REPORT DOCUMENTATION PAGE

Form Approved OMB NO. 0704-0188

1. REPORT DATE (DD-MM-YYYY)	2. REPORT TYPE	3. DATES COVERED (From - To)
15-12-2014	Ph.D. Dissertation	-

4. TITLE AND SUBTITLE
High power UV source development and its applications

5a. CONTRACT NUMBER
W911NF-11-1-0297

5b. GRANT NUMBER

5c. PROGRAM ELEMENT NUMBER
611103

6. AUTHORS
Xiaohen Xu

5d. PROJECT NUMBER

5e. TASK NUMBER

5f. WORK UNIT NUMBER

7. PERFORMING ORGANIZATION NAMES AND ADDRESSES
University of Central Florida
12201 Research Parkway, Suite 501
Orlando, FL 32826 -3246

8. PERFORMING ORGANIZATION REPORT NUMBER

9. SPONSORING/MONITORING AGENCY NAME(S) AND ADDRESS (ES)
U.S. Army Research Office
P.O. Box 12211
Research Triangle Park, NC 27709-2211

10. SPONSOR/MONITOR'S ACRONYM(S)
ARO

11. SPONSOR/MONITOR'S REPORT NUMBER(S)
59727-PH-MUR.83

12. DISTRIBUTION AVAILIBILITY STATEMENT
Approved for public release; distribution is unlimited.

13. SUPPLEMENTARY NOTES
The views, opinions and/or findings contained in this report are those of the author(s) and should not contrued as an official Department of the Army position, policy or decision, unless so designated by other documentation.

14. ABSTRACT
Dating back to the famous “kite” experiment by Benjamin Franklin, human beings (led by a number of daredevils) have been fascinated by the prospect of interrogating, triggering and even harvesting lightning. Advances in high-power laser technology have provided scientists a new tool: when powerful enough, a laser beam can ionize atmosphere, create a plasma channel and propagate as a non-diffracting light bullet called filaments”, which could promote and guide lightning discharge. An ultraviolet (UV) laser would provide unique advantages due to a low

15. SUBJECT TERMS
High Power UV

16. SECURITY CLASSIFICATION OF:			17. LIMITATION OF ABSTRACT	15. NUMBER OF PAGES	19a. NAME OF RESPONSIBLE PERSON
a. REPORT	b. ABSTRACT	c. THIS PAGE			Martin Richardson
UU	UU	UU	UU		19b. TELEPHONE NUMBER 407-823-6819

Report Title

High power UV source development and its applications

ABSTRACT

Dating back to the famous “kite” experiment by Benjamin Franklin, human beings (led by a number of daredevils) have been fascinated by the prospect of interrogating, triggering and even harvesting lightning. Advances in high-power laser technology have provided scientists a new tool: when powerful enough, a laser beam can ionize atmosphere, create a plasma channel and propagate as a non-diffracting light bullet called filaments”, which could promote and guide lightning discharge. An ultraviolet (UV) laser would provide unique advantages due to a low threshold of filament formation. However, a major bottleneck in conducting these experiments is the lack of a powerful yet stable laser source in the UV spectral range. Here, we describe the design and implementation of a high power UV source suitable for laser filamentation studies in air. The system is capable of producing 200 ps, ├ 0.3 J pulses at 266 nm. This corresponds to a peak power of 1 GW, which is well above the critical power required for filament generation. The system includes four critical components: Nd:YAG oscillator, 6-stage amplifier chain, pulse compressor and frequency conversion unit. We optimize each component for maximum energy throughput with an emphasis on stability and reproducibility. At each stage, the optical output is characterized experimentally and compared to theoretical modeling of the corresponding physical processes. A number of technical innovations have emerged during the construction of the system. First, we invented a novel feedback-based cavity stabilization scheme for singlemode operation of the Nd:YAG oscillator. Our scheme eliminated mode beating in ├ 100% of the output pulses over a time scale of hours under noisy environments. Second, we developed a systematic optimization approach for high-energy pulse compression using stimulated Brillouin scattering. Our method achieved temporal compression close to the theoretical limit with unparalleled pulse-to-pulse reproducibility and elucidated the role of a number of overlooked parameters in the literature. Third, we laid down a set of design rules to avoid optical damage as a result of back re ection in a multi-stage amplifier chain. We illustrate the application of the system with preliminary UV filamentation and laser-induced discharge studies. Future directions are discussed.

High power UV source development and its applications

by

Xiaozhen Xu

B.S., Shanghai Jiaotong University 2004
M.S., Optical Science and Engineering, University of New Mexico, 2008

THESIS

Submitted in Partial Fulfillment of the
Requirements for the Degree of

Doctor of Optical Science and Engineering

The University of New Mexico

Albuquerque, New Mexico

February, 2014

High power UV source development and its applications

by

Xiaozhen Xu

B.S., Shanghai Jiaotong University 2004
M.S., Optical Science and Engineering, University of New Mexico, 2008

PhD., Optical Science and Engineering, University of New Mexico, 2014

Abstract

Dating back to the famous "kite" experiment by Benjamin Franklin, human beings (led by a number of daredevils) have been fascinated by the prospect of interrogating, triggering and even harvesting lightning. Advances in high-power laser technology have provided scientists a new tool: when powerful enough, a laser beam can ionize atmosphere, create a plasma channel and propagate as a non-diffracting light bullet called "filaments", which could promote and guide lightning discharge. An ultraviolet (UV) laser would provide unique advantages due to a low threshold of filament formation. However, a major bottleneck in conducting these experiments is the lack of a powerful yet stable laser source in the UV spectral range.

Here, we describe the design and implementation of a high power UV source suitable for laser filamentation studies in air. The system is capable of producing < 300 ps, $\sim 0.3J$ pulses at 266 nm. This corresponds to a peak power of ~ 1 GW,

which is well above the critical power required for filament generation. The system includes four critical components: Nd:YAG oscillator, 6-stage amplifier chain, pulse compressor and frequency conversion unit. We optimize each component for maximum energy throughput with an emphasis on stability and reproducibility. At each stage, the optical output is characterized experimentally and compared to theoretical modeling of the corresponding physical processes.

A number of technical innovations have emerged during the construction of the system. First, we invented a novel feedback-based cavity stabilization scheme for single-mode operation of the Nd:YAG oscillator. Our scheme eliminated mode beating in $\sim$100% of the output pulses over a time scale of hours under noisy environments. Second, we developed a systematic optimization approach for high-energy pulse compression using stimulated Brillouin scattering. Our method achieved temporal compression close to the theoretical limit with unparalleled pulse-to-pulse reproducibility and elucidated the role of a number of overlooked parameters in the literature. Third, we laid down a set of design rules to avoid optical damage as a result of back reflection in a multi-stage amplifier chain.

We illustrate the application of the system with preliminary UV filamentation and laser-induced discharge studies. Future directions are discussed.

Contents

Chapter 1

Introduction

For ages, the perception of lightning has been associated with awe and fear by the human race. In ancient Chinese culture, lightning is produced by the "God of Thunder", a fearsome man-bird hybrid with blue face and sharp claws, to punish evil crimes, secret guilt and polluted spirits. Even to this day, when scientists are capable of manipulating individual atoms and molecules [1] and sending folks on the moon, we still do not understand every detail about lightning. Part of the reason lies in the fact that we have to wait (or by pure serendipity [2]) for lightning to spontaneously take place. This makes ground observation difficult. For example, even in Florida, the lightning capital of United States, discharge happens only about 40 times per kilometer squared per year. Moreover, only 25% of those lightning events are cloud-to-ground, the rest are cloud-to-cloud and intra-cloud.

Naturally, we ask the question, can mankind any kind of control over lightning? For example, instead of passively waiting for it to happen, can we "trigger" the discharge? This has been the central theme of human investigation, from Benjamin Franklin's famous "kite" experiment [3], to protective lightning rod and recent "lightning-harvesting" rockets.

The invention of lasers provided scientists a brand new way to study and interact with lightning. This leverages on the fact that high-power lasers are capable of ionizing the basic constituent molecules (O_2, N_2) of the atmosphere, creating plasma channels that act as "wave-guides" of lightning. In fact, at the early stages of laser development, high power CO_2 and Nd:YAG lasers were already used to induce breakdown in gases (see ref [4] and the references within). Because typical ionization energy of most gases range from 10eV to 20eV, multi-photon ionization processes are required, which calls for lasers with enormous peak intensities. As an example, in order to ionize O_2, which has an ionization energy of 12 eV [5], an intensity of $\sim 10^{13}$ (W/cm^2) at 800 nm (1.5 eV) is required to produce a reasonable ionization rate of 10^6 s^{-1} via an eight-photon process.

One additional requirement to make "laser-guided" lightning feasible is the generation of laser "filaments" in the atmosphere. These are "non-diffracting" beams that maintain highly localized electromagnetic energy over long propagation distances ($\sim$km). When a high intensity laser propagates in a transparent medium such as glass or air, the intensity-dependent refractive index of the medium creates a "Kerr lens" which tends to focus the beam. On the other hand, when the beam is focused, it creates ionized plasma in the medium which then defocuses the beam. Balancing of the two effects leads to a "filament" beam that maintains its width over distances much longer than the Rayleigh range. The physics of laser filamentation has been extensively studied [6] during the past 20 years and fascinating new application has emerged along with theoretical development. Braun et al. [7] were the first to experimentally observe filamentation in air. Zhao [8] demonstrated triggering and guiding electrical discharge using fs UV pulses and Tzortzakis [9] showed laser guided discharge by fs infrared pulses. One notable example is the teramobile project [10]. The "teramobile" is a femtosecond system suitable for field measurements. It is capable of delivering 70 fs, 350 mJ pulses (peak power $\sim$ 5 TW) at 800 nm. Filaments can be formed in the atmosphere at predetermined distances. The team has used the system

to investigate constituents of the atmosphere using the white-light continuum from such a powerful source [11], trigger water condensation [12] and recently, observe correlated lightning [13].

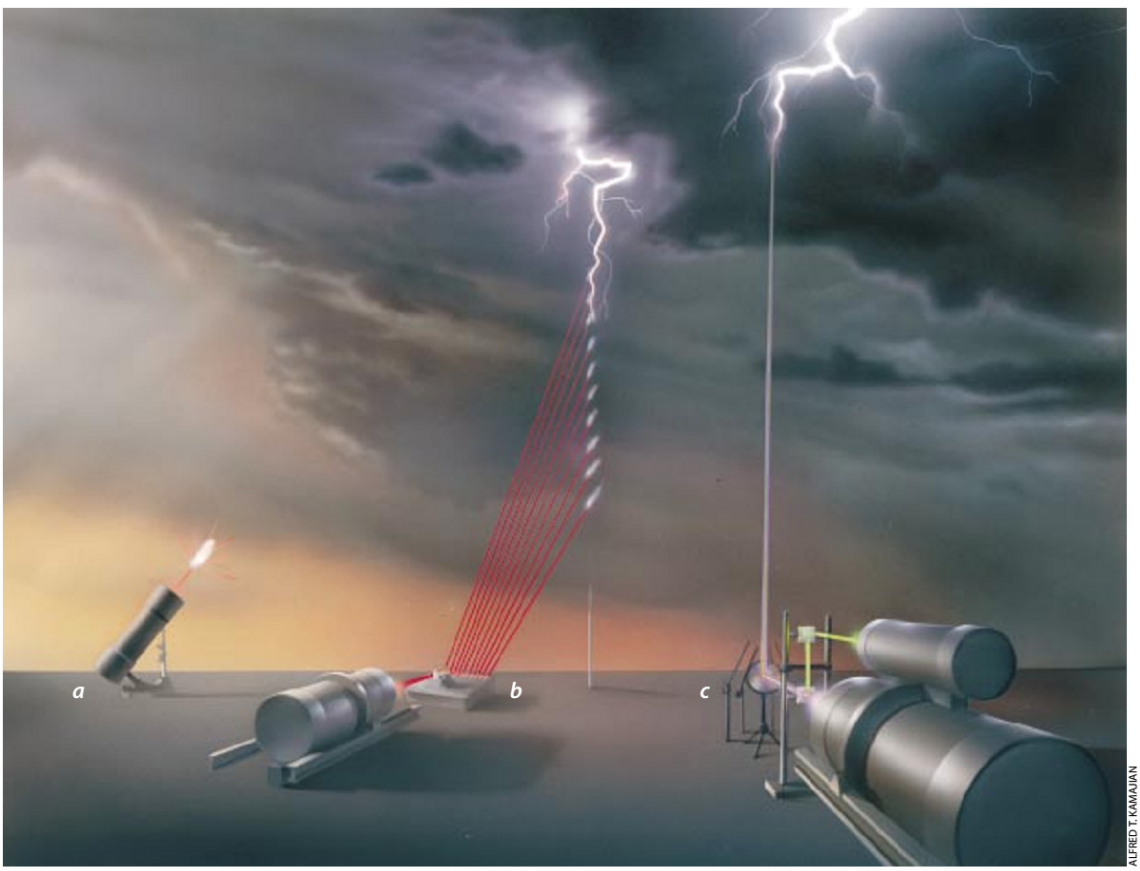

Figure 1.1: Artist's conception of laser induced lightning experiments From Diels et al.

1.1 Motivation for high-power UV lasers

Most experiments were conducted in the NIR at 800 nm, utilizing the matured technology of Ti:Sapph systems. It has been realized early that UV light should provide many advantages for laser-guided lightning. For example, with 266 nm pulses, the

ionization of O_2 is reduced to a 3rd order process. The Diels research group pioneered the use of UV filaments to create laser guided plasma channels. Zhao [8] was the first to investigate mechanism of UV laser induced discharge in gases. Rambo [14] studied extensively induced discharge by UV femtosecond pulses at 248 nm and proposed heating up the plasma by a second laser via inverse bremsstrahlung process. Schwartz [15] worked out an analytical solution to describe UV filament generation and propagation in air. Chalus [16] conducted pilot experiments to generate UV filaments in air using sub-nanosecond pulses. However, detailed research on filaments characterization and application were thwarted by the lack of reproducibility and frequent optical damage resulting from the high peak power. The current thesis thus describes a revamped design of the UV source for filamentation and laser-induced lightning studies. We focus on the design, implementation and characterization of a stable laser system which successfully generates < 300 ps UV pulses with $\sim$gigawatt of peak-power.

1.2 Existing strategies to generate sub-ns UV pulses

Before a detailed description of the entire system, it is helpful to put our work into context and provide some motivation. Here we briefly review the existing technologies for generating high-power UV pulses.

1.2.1 Excimer lasers

Excimer lasers uniquely produce coherent light emission in the ultraviolet region. Its gain medium is a gas mixture, generally containing a noble gas (e.g. Xe, Ar) and a halogen (e.g. Cl_2, F_2). It is pumped by a powerful electron beam (e-), which

generates dimeric (excimer) species between the noble gas and the halogen (e.g. ArF). The excimer complexes, however, is only metastable and quickly dissociate (∼ns) to yield a spontaneous or stimulated UV photon.

Perhaps the best known example of the excimer laser is its use in LASIK operations. In this scenario a 193 nm laser of 1mJ and ∼10ns pulse duration is used to ablate a thin layer (∼10um) of the cornea stroma for restoration of corrected vision. Other important application of the excimer lasers is in deep UV lithography. Technological development in this area is actively being pursued by companies such as Cymer Inc to keep up with Moores law.

Can excimer lasers be used to generate filament in the UV? Not quite, at least for commercial products. For example, the high-power line from Coherent (VYPER) lases at 308 nm with 2 J per pulse and pulse width about ∼29 ns. This corresponds to a peak power of 0.07 GW, about 10 times lower than the required power of ∼0.65 GW [17] for stable filament generation. Excimer lasers also suffer from the disadvantage of limited operation lifetime.

1.2.2 Free electron lasers

The free electron laser has emerged as a versatile source capable of producing coherent radiation from x-ray to terahertz [18]. It works by wiggling relativistic electrons and harvesting their radiation. It is an attractive source for otherwise hard-to-find wavelengths, such as x-ray and extreme UV (from 10 nm to 100nm). However, it requires dedicated large facilities for operation and currently are limited to ∼100 MW of peak power.

1.2.3 Harmonic generation

The most straightforward approach is to start with an oscillator in the visible or near infrared and use nonlinear frequency conversion to reach the UV spectral region. In early experiment, Zhao [8] generated femtosecond, 200 uJ, 248 nm pulse using the third-harmonic from a Ti:Sapph oscillator at 744 nm.

Perhaps the most spectacular UV source of this kind is the laser system designed and constructed at the National Ignition Facility (NIF). There, a total of 1.8 MJ, 351 nm light with 5 ns pulse duration, combined from 192 independent beam lines, were delivered to ignite fusion, producing a peak power of $\sim$500 TW. The final output wavelength (351 nm) is produced by second harmonic generation (SHG) followed by sum frequency generation of the fundamental 1053 nm light.

The harmonic generation approach offers a number of advantages. First, high power Ti:Sapph systems and Nd:YAG, Nd: glass lasers are readily available, offering an excellent fundamental source for harmonic generation. Second, pulse shaping techniques that rely on light-matter interactions are much easier to implement at visible or NIR wavelengths than at the ultra violet due to their small linear and multi-photon absorption. Third, high quality UV optics are expensive and difficult to manufacture. Thus, producing the UV pulse at the last harmonic generation stage seems most effective and economic. The laser system described in this thesis follows the harmonic generation approach.

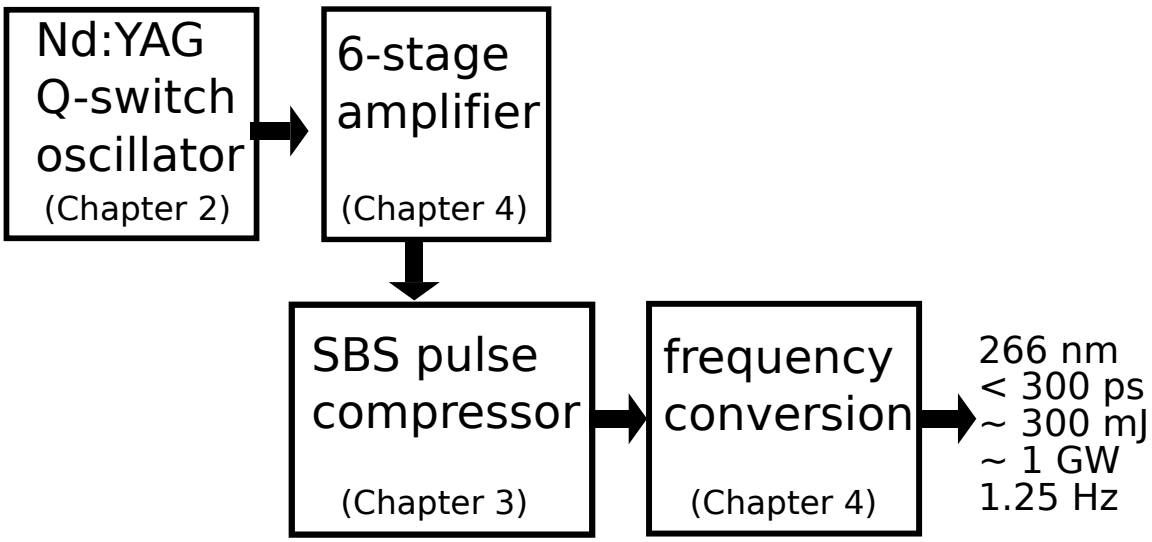

Figure 1.2: Laser system schematic

1.3 System layout based on Q-switched Nd:YAG system

Our laser system is consisted of the following components (Fig. 1.2). The first is an injection-seeded, Q-switched Nd:YAG oscillator producing pulses of 8 ns at its FWHM and 120 J/pulse. Unique to our system is a novel feed-back stabilization scheme developed to produce pulses with a clean single mode at every laser shot. The details of the oscillator design will be described in Chapter 2. The 1064 nm light coming out of the oscillator then goes through a six-stage Nd:YAG amplifier system, which boost the energy at 1064 nm by a factor of 45 to 5.4 joule per pulse. The amplifier design and characterization will be summarized in Chapter 4. After the amplifier, we further increase the peak power of the output by pulse compression. Our pulse compressor, discussed in depth in Chapter 3, is based on the well-established principle of stimulated Brillouin scattering but extensively optimized in energy throughput for our applications. Finally, light is frequency converted to the

4th harmonic at 266 nm. We discuss design considerations in Chapter 4. Finally, we show some preliminary UV filament and induced discharge studies using our laser system and point to future directions in Chapter 5.

Chapter 2

Single mode operation of an injection seeded Q-switched Nd:YAG laser

2.1 Introduction

Single mode high power pulse lasers have many applications in spectroscopy and nonlinear optics, such as high energy pulse compression by stimulated Brillouin scattering. For the latter, a smooth temporal profile with no spikes, typical of single mode operation, is required. There are generally two ways to obtain single mode operation in high energy Q-switched lasers. One is to introduce mode selecting elements (e.g. etalons) inside the cavity to add extra loss for undesired modes. Meanwhile, the Q-switch build-up time is increased (pre-lase or pre-pulse) to ensure large enough passages through the mode selecting elements for good mode discrimination before the Q-switch opens [19, 20, 21]. Injection seeding is another popular method [22, 23]. By injecting an external field to enhance mode discrimination during the pulse build-up,

no intra-cavity mode selecting element is needed. With a narrow-linewidth injected field that is close to the center of the gain curve, the cavity mode that coincides with the injected frequency builds up faster because of its higher initial condition (starting from the injected signal instead of fluorescence noise), and because of the vectorial field addition at each round-trip at an early stage of the build-up. This seeded mode then reaches the saturation level of the gain before other modes, and depletes the population inversion, leading to single mode operation. In this chapter, we use the injection seeding method.

Since the first demonstration of injection seeded Q-switched Nd:YAG lasers [23], several cavity stabilization schemes [24, 25, 26, 27] have been deviced to match the cavity mode to the injected mode for long term single mode operation. The build-up-time minimization method [24] measures the build-up time of the laser output and *predicts* a cavity length adjustment for the next output. Because it relies on previous laser shots to correct the laser resonator, it becomes inaccurate at low rep-rate and high gain where shot-to-shot variation of the cavity length becomes critical. The "Ramp-hold-fire" method [25], although immune to noisy environment, needs high injected power ($\sim$500mW) to detect an error signal over a large fluorescence background. Moreover, the tens of μs time jitter inherent in this method makes it unsuitable for operation requiring external synchronization. In section 2.4 we describe and demonstrate a robust stabilization scheme suited for low repetition rate operation in a noisy environment, requiring only mW injected power. The time jitter is less than 2 ns. Additional advantages are that the control system is simple and easy to implement, requiring only a photo detector, a data acquisition card and a computer with LabVIEW program. Similar real-time feedback control system has been successfully demonstrated for mode-locking optimization [28]. Before that, in section 2.2 we characterize the cavity length changes due to heating from the flashlamp pumping at different repetition rate. A custom-built cavity stabilization scheme based on minimizing the Q-switch pulse build-up-time is also demonstrated

in section 2.3.

In spite of variations in different injection schemes and cavity stabilization methods, it is generally acknowledged that slowing down the Q-switch speed is necessary to achieve clean single mode pulses [25, 29, 26]. However, the mechanism had, up to now, not been elucidated. In section 2.5 we demonstrate the dependence of seeding performance on the opening speed of the Q-switch and present a quantitative model for its explanation. The simulation fits the experiments well and also predicts the mode selectivity for a broad range of parameters: finite Q-switch opening time, injected power (from several mW to hundreds of mW), and gain.

2.2 Cavity length breathing by heating from flashlamp pumping

The Nd:YAG crystal is pumped by flashlamps filled with a mixture of krypton (90%) and xenon (10%) at 1200 torr. Both the Nd:YAG rod and flashlamp are cooled by circulating water. The flashlamp emits a broad spectrum ranging from 200 nm to 1100 nm, while the Nd:YAG absorbs from around 500 nm to 900 nm. The effective absorption for lasing at 1064 nm is centered at 808 nm. As a result, the majority of absorption from the flashlamp emission is transferred into heat. Heating changes the refractive index of the Nd:YAG crystal and is the dominant contribution to the effective cavity length fluctuation. Non uniform heating causes in addition thermal birefringence.

2.2.1 Analysis method

To tailor an effective cavity length stabilization method to our application (high energy flashlamp pumping at low repetition rate), we analyze the transient cavity response to an applied elongation. This is done by monitoring the transient transmitted power of the injected CW seed laser through the cavity, without opening the Q-switch, i.e. without laser action. We first measure the cavity transmission in

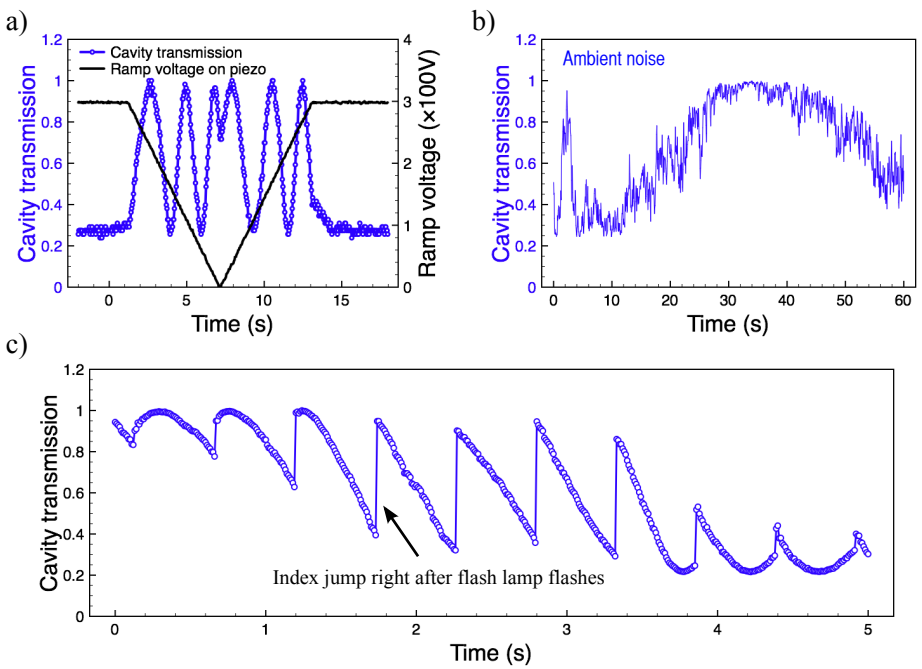

Figure 2.1: a) Cavity transmission response to cavity length changes. The cavity length is scanned by adding ramp voltage on the piezo element attached on the cavity end mirror; b) Monitoring the cold cavity length fluctuation from ambient noise; c) Cavity length variation under flashlamp pumping. There is a rapid change of cavity transmission right after each flashlamp shot, indicating a rapid change of cavity length. It then relaxes slowly until the next shot.

response to cavity length changes, as shown in Figure 2.1 (a). The cavity length is scanned by adding ramp voltages on the piezo element attached to the cavity end mirror. Variation of the transmission from minimum to maximum corresponds to

a cavity length change by $\lambda/4$. Figure 2.1 (b) shows the cavity length drift under ambient noise. In figure 2.1 (c), the cavity length undergoes a jump right after the flashlamp flashes, indicating a rapid index changes of the rod from heat. After the flashlamp pulse (last for 210 μs), the cavity length relaxes gradually until the next flashlamp pulse. However, the cavity length does not usually relaxes to the same value as the previous shot due to the inefficient and inaccurate water cooling. As shown in figure 2.1 (c), the cavity length drifts by $\lambda/4$ after 7-8 shots.

2.2.2 Cavity length breathing at different pumping and repetition rates

With the method we describe in section 2.2.1, we can analyze this cavity length "breathing" motion in different experimental conditions. Figure 2.2(a) shows the transient cavity length at different pumping power. The higher the pump power, the higher the rod temperature after the flashlamp pulse, thus the more dramatic the cavity length variation. Figure 2.2(b) shows the transient cavity length at different repetition rates. The shot-to-shot variation is calculated for three different repetition rates, in which 100% variation corresponds to the cavity transmission changes from minimum to maximum. The shot-to-shot variation is as high as 10% at low repetition rate, making it difficult for any shot-to-shot based cavity length stabilization method to work, such as the build-up-time minimization method. In section 2.3, we demonstrate the build-up-time minimization method. The repetition rate of the laser is increased from 2 Hz to 7 Hz, which is a compromise between moderate shot to shot variation and thermal lensing effect. In section 2.4, we demonstrate a new method, the real-time resonance tracking method, with which the Q-switched cavity outputs single longitudinal mode pulse in every shot.

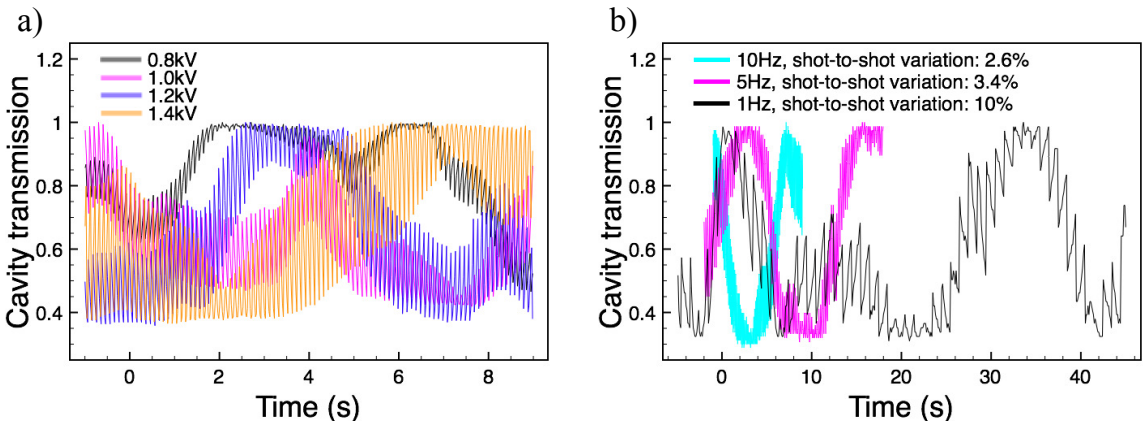

Figure 2.2: a) Cavity length breathing motion at 10 Hz with different pump power; b) Cavity lenght breathing motion at different repetition rates. 100% of variation corresponds to cavity transmission changes from its minimum to maximum, i.e. cavity length changes by $\lambda/4$.

2.3 Cavity length stabilization by build-up-time minimization method

2.3.1 Basic principle

The build-up time of a Q-switched pulse, time interval between the Q-switch opens and the emission of a giant pulse, is reduced when the cavity is injection seeded with a seeder whose frequency coincides with the peak of the gain curve. The build-up time is further reduced as the cavity (resonator) is tuned from being off resonance to at resonance with the injected frequency, because the vectorial electric field addition becomes most efficient when the cavity mode and the injected frequency are the same. Figure 2.3 demonstrates this effect. The black curve is the measured high voltage switching applied to the Pockels cell. There are two groups of Q-switched pulses. The red arrow points to the group representing single mode pulses when the cavity is at resonance with the injected frequency, which is smooth and has little

modulation in time. The green arrow points to the group representing multi-mode pulses when the cavity is off resonance with the injected frequency, where strong temporal modulation caused by mode beating is shown. These two groups of pulses are measured in time relative to the same Q-switch trigger. A clear time of arrival difference of about 7 ns can be seen between these two groups.

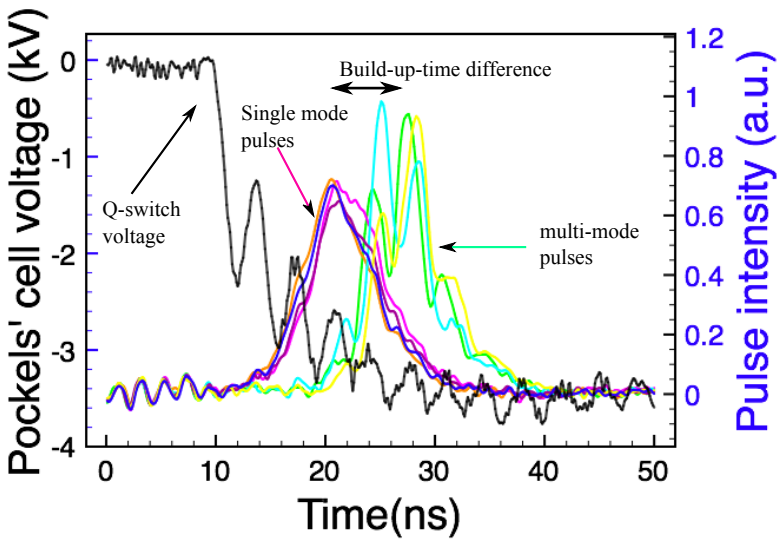

Figure 2.3: Build-up-time difference between single and multi-mode, when the cavity mode is either at- or off- resonance with the injected frequency. Black curve: high voltage applied to the Pockels cell. Single mode pulses and multi-mode pulses are measured at the same time. The arriving time difference between them represents the build-up-time difference.

The idea of the build-up-time minimization method is based on the fact that the build-up-time (BUT) reaches its minimum when the cavity is fine tuned to be at resonance with the injected frequency [24]. For a high gain Q-switched cavity, it takes only a couple of round-trips to build-up a giant pulse, with pulse width of 6 to 10 ns. In this case, the build-up-time difference between resonance and off resonance case is only 1-2 round-trips, which is 3.5 to 7 ns for a cavity of 50 cm long.

2.3.2 Experimental method and results

To measure such a small time difference with sub-ns accuracy and use it as the error signal to feed-back control the cavity length, we custom-built a time-to-voltage conversion circuit, which converts the time interval between a start pulse and a stop pulse into voltage. The circuit first converts the time interval into the width of a square pulse. The start pulse comes from the Q-switch trigger; a TTL signal generated by a function generator. The stop pulse comes directly from a fast optical detector which detects the Q-switched pulse. The square pulse, of which the width corresponds to the build-up time, then triggers the start and stop charging of a capacitor. The final voltage across the capacitor is proportional to the build-up time. The circuit measures a time delay as short as 7 ns, with resolution of 500 ps, and the scalable capacitor allows measurement of different ranges of time delay.

Figure 2.4(a) shows the measured build-up time voltage in response to the cavity length changes. The cavity length is scanned by adding ramp voltage on the piezo electric element attached on the cavity end mirror. Periodic oscillation of BUT voltage can be seen, indicating the BUT is oscillating as the cavity mode is scanned across the injected frequency. A data acquisition card controlled by LabVIEW is externally triggered to read the BUT voltage when it is ready, and send it to LabVIEW as an error signal for feedback control calculation. We tried different algorithm and the following one works the best. As it is shown in figure 2.4(b), the periodic oscillation of BUT voltage in response to ramp voltage can be modeled as a sinusoidal function plus a noise dependent phase: $BUT = A\sin(\frac{V}{V_0}2\pi + \phi) + B$. A, B and V_0 is predetermined by scanning the BUT for 100 oscillation. ϕ is a noise dependent phase. Figure 2.4(c) shows the drifting of phase during 180 s of scanning time. For each measured BUT and the piezo voltage of the previous pulse, BUT_1 and V_1, the algorithm estimates a phase according to the model and then applies a new feedback voltage that corresponds to the minimum of the sinusoidal function:

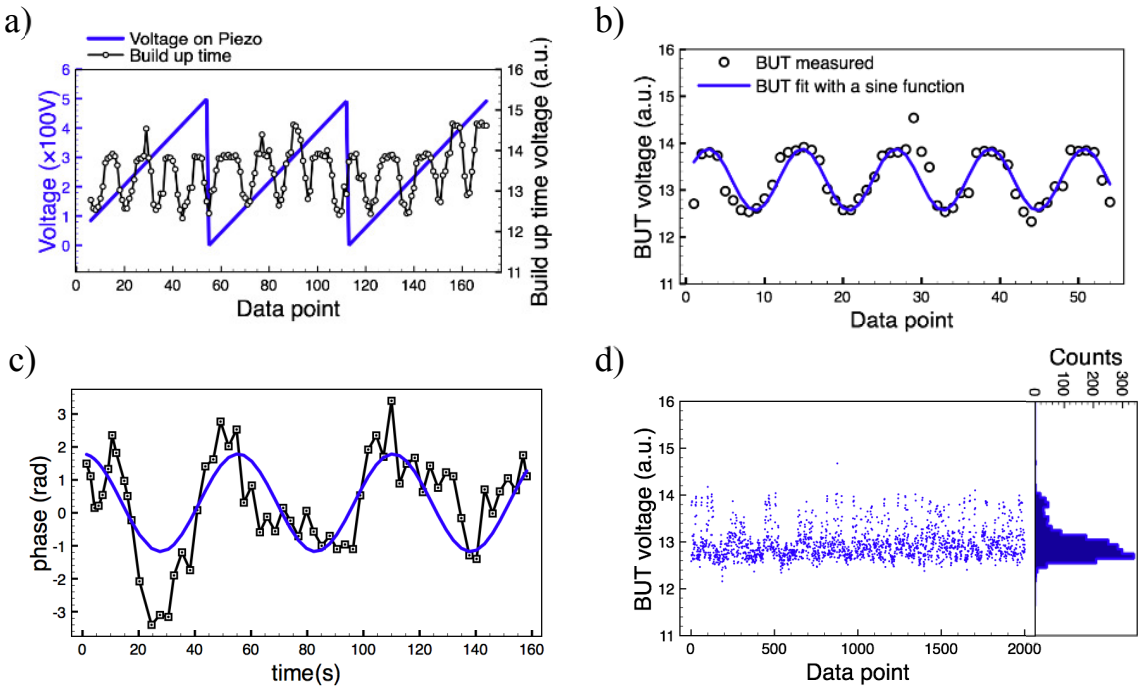

Figure 2.4: (a) Build-up time (BUT) changes in response to cavity length changes. Black: build-up time voltage that is proportional to the build-up time. Blue: ramp voltage applied to the piezo attached to the cavity end mirror. (b) Model the BUT response to ramp voltage on piezo as a sinusoidal response plus a noise dependent phase. (c) Monitor the phase variation versus time. Scanning ramp voltage on the piezo for 180s. Each phase (black square) is extracted from a sinusoidal fit of 10 successive shots. Blue: a sinusoidal fit to the phase variation. (d) Single mode performance when the feedback is turned on. 2000 shots are sampled and about 85% of them are considered single mode (BUT voltage below 13.2). On the right of the data, a histogram quantifies the spread of data.

$V_{new} = V_1 - \arcsin(\frac{BUT_1 - B}{A})/2\pi$. Figure 2.4(d) shows the performance of this algorithm. 2000 shots are sampled and about 85% of them considered single mode, of which the build-up time voltage is below 13.2.

As a comparison, we simulate the performance of the new algorithm and the conventional gradient descent algorithm (to find the minimum). BUT is generated using the above model. Under the same noise level, figure 2.5 shows that our new algorithm has better result in controlling the BUT to its minimum. However, because

of the high noise level of the system (from shot to shot variation), and low contrast of the error signal (only 9%), the BUT is not 100% locked to minimum and the output pulses are not 100% single mode.

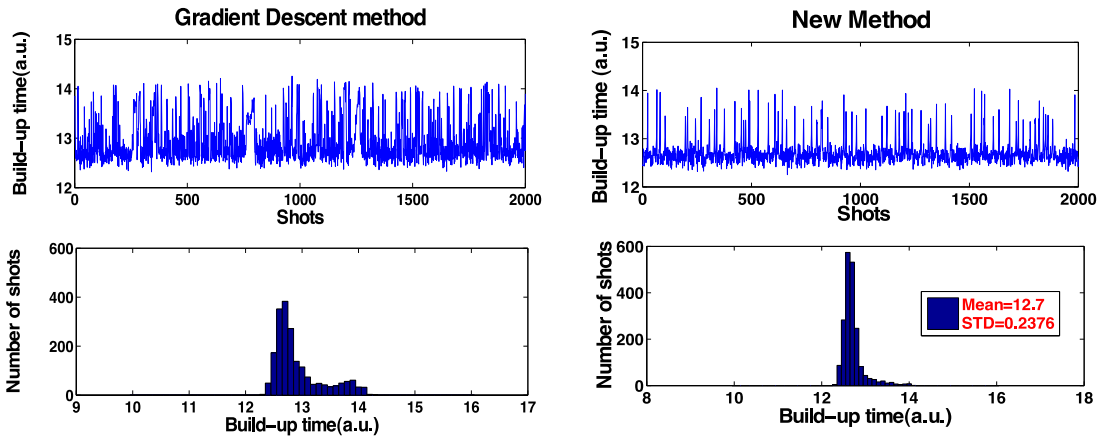

Figure 2.5: Simulation of the performance of two different feedback algorithms. Left: The gradient descent Method for looking for minimum. Feedback voltage is proportional to the negative slope. Right: New method based on the sinusoidal modeling of BUT v.s. Voltage. Update the phase for each BUT measurement and feed back a voltage that corresponds to the minimum of the sine function. Under the same noise level, the new feedback method controls the average BUT 2% lower and the standard deviation of BUT is only 55% of the gradient descent method.

2.4 Cavity length stabilization by real-time resonance tracking method

2.4.1 Real-time resonance tracking method

High energy flashlamp pumping results in a significant change in the temperature distribution in the laser rod after the Q-switched pulse. Therefore, the higher the

pumping energy and the longer the time interval between pulses, the less reliable the information on optical length of the cavity derived from prior pulses in the build-up-time minimization method [24]. We choose instead, via realtime feedback control, to have the cavity mode continuously track the seed wavelength in the time interval *between* pulses, as it is explained in figure 2.6.

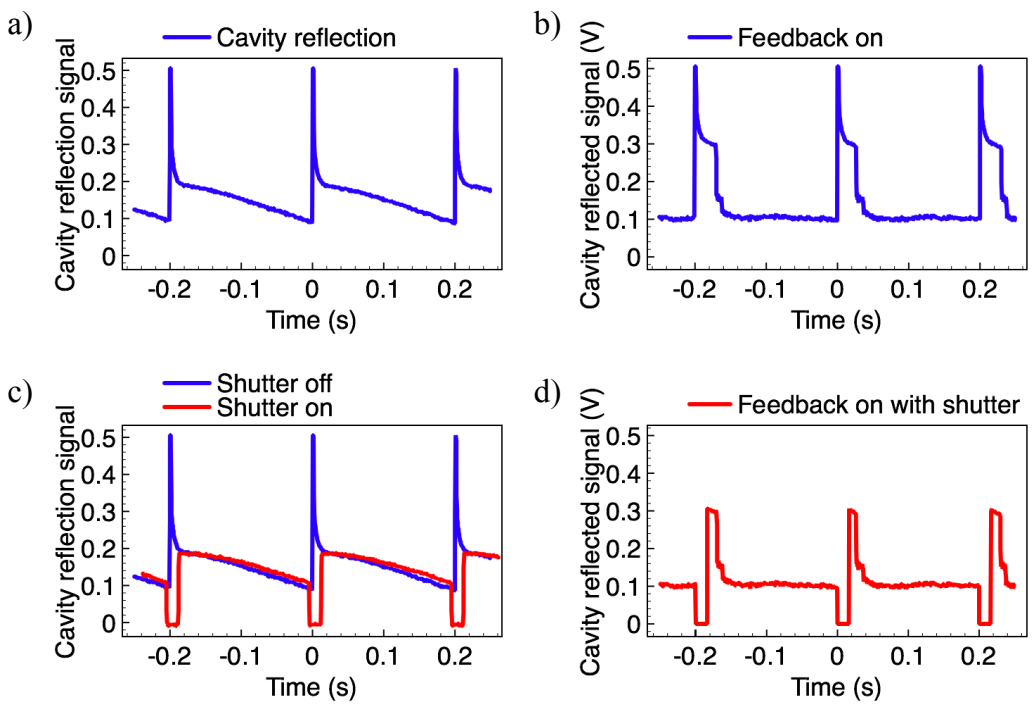

Figure 2.6: Idea of the real time resonance tracking method. Vertical axis are seed intensity reflected from the Q-switched cavity. (a) Cavity reflection signal. The spikes are fluorescence from the gain medium when the flashlamp flashes. After the fluorescence pulse, the cavity reflection varies in between pulses as the cavity length "breathes". (b) The real-time resonance tracking method tracks the cavity reflection signal and adjust the cavity length to lock the reflection to its minimum, i.e. lock the cavity to be at resonance with the injected frequency. (c) Since the fluorescence spike provides no information about the cavity resonance in this method, it is blocked by a synchronized shutter. (d) The cavity reflection with shutter and real-time feedback control. That reflection is locked to a minimum value in the time interval between pulses, while the shutter is open.

The idea of this method is, instead of letting the cavity length relax to some

random value after the flashlamp pulse, to continuously track the cavity resonance and lock it to be resonant with the injected seed frequency. As shown in figure 2.6(c), the fluorescence pulse is actually noise on the error signal for this slow resonance detection. A synchronized shutter that closes for a short period of time can be used to block the fluorescence pulse. While the shutter is open, the signal is used as the error signal for feedback control.

This method is effective, because the Q-switched pulse builds up and leaves the cavity (within 200μs) before the heat shock from the flashlamp pumping takes notable effect on the cavity length.

2.4.2 Experimental setup

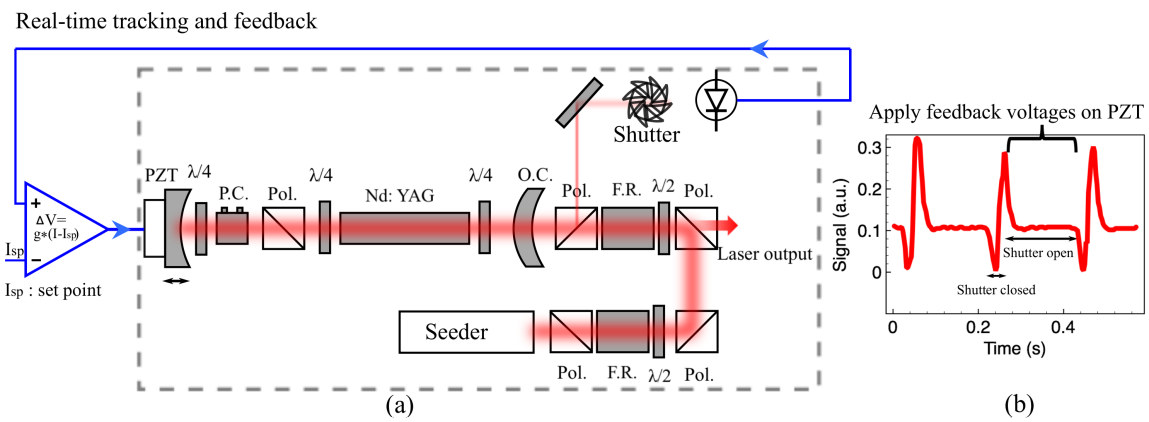

Figure 2.7: (a) Experimental setup. Pol: polarizer; PZT: piezo; P.C. : Pockels cell; $\lambda/4$: quarter wave-plate; $\lambda/2$: half wave-plate; O.C.: output coupler; F.R.: Faraday rotator. (b) Real-time cavity reflected signal measured from leakage of a polarizer, after a synchronized shutter and with feedback on.

Figure 2.7 (a) shows the injection and detection setup for realtime resonance tracking method. An unstable resonator configuration is used, with a R_0 =12% reflectivity Gaussian output coupler [30] providing an output with single spatial mode. With a flashlamp pump energy of 40 J at 5 Hz, Q-switched pulses of 120

mJ, 9.5 ns FWHM are generated. A 60 mW CW seed beam (linewidth <10MHz) is injected into the Q-switched laser cavity through two isolators and the Gaussian output coupler. The purpose of the isolators is (i) to inject the seed laser via the output coupler, and (ii) to decouple the seed cavity from the high power Q-switched cavity. Two cross-axis quarter-wave plates are placed on both sides of the Nd:YAG medium to create a "twisted mode" inside the gain medium for spatial-hole-burning elimination [31]. The switching time of the cavity (controlled by switching the high voltage applied on the Pockels cell) is slowed down to 24.6 ns.

For real-time resonance tracking, we monitor the reflection of the injected signal off the Q-switched cavity via the leakage from a polarizer. The reflection reaches a minimum when the cavity is resonant at the injected optical frequency. As the cavity is tuned across the resonance, we measured 63% fringe visibility, 6 times higher than using the build-up-time method or "Ramp-hold-fire" method. To prevent "blinding" the detector with the strong fluorescence generated from population inversion and the Q-switched pulse, a synchronized shutter closes for about 20 ms when the flashlamps are activated. At any other time the shutter is open, a data acquisition card samples the signal from the photo detector at 1 kHz and sends it as input to the feedback loop realized in LabVIEW. The input value is then compared to a minimum set point and the difference serves as an error signal. Different control algorithms can be implemented in the feedback loop to suit different systems. For our system, a simple proportional control method works best and is very robust. The change of output voltage on the piezo element attached on the cavity end mirror can be expressed as $\Delta V = g \times (I - I_{sp})$, in which g is the gain, I is the input signal, I_{sp} is the set point. The loop time is about 7 ms, including 5 ms for the piezo element to settle down in its new position. During a pulse period of 200 ms, this algorithm can provide 20 feedback corrections to the cavity, more than enough (3 to 4 corrections are enough) to adjust the cavity to the resonant condition before the next Q-switched cycle begins, as shown in Figure 2.7(b).

2.4.3 Experimental results

To evaluate the performance of our method, we sample 104 shots of the laser for half an hour with a fast Si avalanche photodiode (Hamamatsu S2831) and oscilloscope (Tektronix TDS620B). We record the normalized Fourier amplitudes of the temporal pulse shapes at 285 MHz (the longitudinal mode spacing of the cavity), as a measure of the temporal modulation depth.

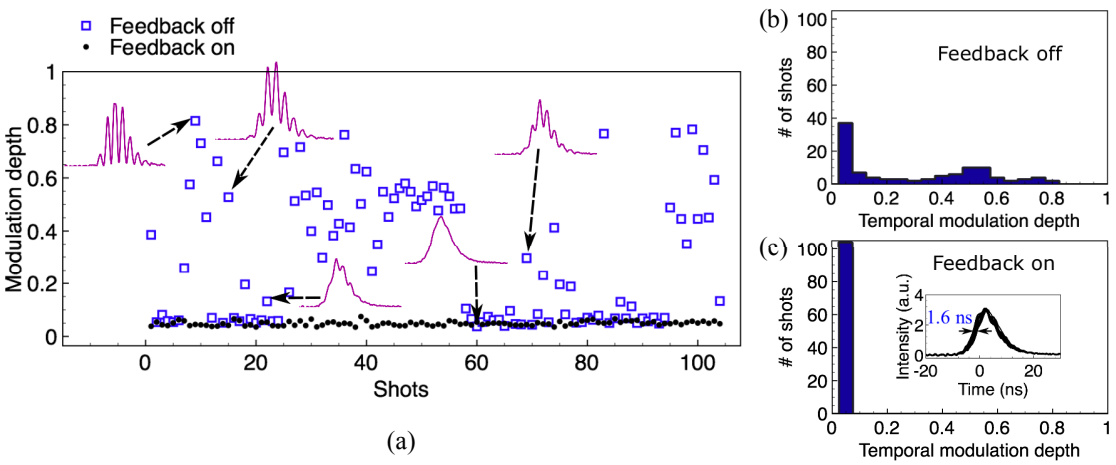

Figure 2.8: (a) Pulse temporal-modulation-depth analysis for 104 shots with feedback off and on. Purple: sample of temporal pulse shapes with different modulation depth. (b) Histogram of intensity modulation depth with feedback off and (c) with feedback on, insert: overlapping of 20 pulses shows a time jittering of 1.6 ns.

The modulation depth of the Q-switched pulses is plotted as a function of the pulse index (from 1 to 104), with the feedback turned off (squares) or on (dots). With the feedback off, the cavity-length drift from shot to shot results in a scattered distribution of modulation depth. This shot to shot variation comes from the thermal effect from high energy flashlamp pumping, inefficient water cooling and ambient thermal fluctuation at the low repetition rate. As the feedback is turned on, the laser outputs a smooth pulse in almost every shot (>95% of the pulses have a modulation depth $\leq$ 6.3%, or an intensity contrast >1000, all of the pulses show an intensity

contrast >500, as indicated in Figure. 2.8(c)). Within the half an hour of sampling time, a maximum time jitter of 1.6 ns (see Figure 2.8 (c) insert) is measured, 1000 times smaller than that of the "Ramp-hold-fire" method. Cavity length fluctuation away from resonant conditions are responsible for the jitter in the arrival time of the Q-switch pulse. Knowing that the pulse build-up time difference between the on- and off-resonance condition is about 7 ns, a 1.6 ns time jitter indicates a cavity length control (at the time of the Pockels cell opening) to be within 11.4% of a wavelength.

As the cavity is detuned from resonance, the range over which the intensity contrast is >500, or the mode selection range, is measured to be 53 MHz, 18.6% of the cavity free spectral range. This measurement is comparable to that reported elsewhere [32] and to the frequency bandwidth of a 9.5 ns Fourier-transform-limited pulse (46 MHz).

Within at least 8 hours of daily usage of the Q-switched laser, single mode operation is maintained without a need for adjustment once a suitable set point is chosen.

2.5 Mode purity dependence on Q-switch speed

The results in section 2.3 and 2.4 are achieved with a cavity Q-switch opening time of 24.6 ns. We've noticed that a clean single mode can be achieved only when the Q-switch speed is slowed down to a certain value. In order to study the underlying mechanism and to optimize the Q-switch speed, we investigated the relationship between switching speed and the resulting single mode quality by both experiments and theoretical modeling.

2.5.1 Q-switch speed modification and measurement

The switching speed is modified by adding different resistors in series with an electrode of the Pockels' cell. It is characterized by a time constant τ_Q, the cavity Q switching time, in which the cavity Q is switched to 1/e of its maximum value. It is measured by detecting the 60 mW seed laser after double passage through the quarter-wave-plate and the Pockels cell, and an analyzing polarizer. We focus the beam on a Si detector DET-210 from Thorlab, which has a rise time of 1 ns, active area of 0.8 mm^2, responsivity of about 0.02A/W at 1064nm. With a 50 Ω termination, we are able to measure a signal of about 30 mV while there is no voltage applied on the Pockels' cell. When the 4 KV high voltage on the Pockels' cell is switching, the detector, however, picks up electronic noise from the Pockels' cell driver. We measure this background noise by blocking the seeder and subtract it from each measurement for 5 different switching time settings. 10 measurements are made for each switching time settings and the averaged and normalized results are shown in figure 2.9 with blue dots. The red lines are fitted exponential curves.

2.5.2 Mode purity measurement at different switching speed

Slow Q switch brings loss to cavity and leads to low energy output. However, in the injection seeded Q-switched cavity with not very high injected power (e.g. with a CW seeder), the switch needs to be slowed down to get a clean temporal pulse shape. With the original Pockels' driver from Coherent, we measure the Q-switching time to be 2.6 ns, as shown in figure 2.9. In this setting and with our 60 mW seeder, the cavity always outputs a pulse with spiky temporal profile, even though the cavity is tuned to be on resonance with the injected frequency. This indicates that there are more than one longitudinal frequency that are lasing simultaneously. To quantify the mode purity, we use the same method as in section 2.4.3. From the modulation

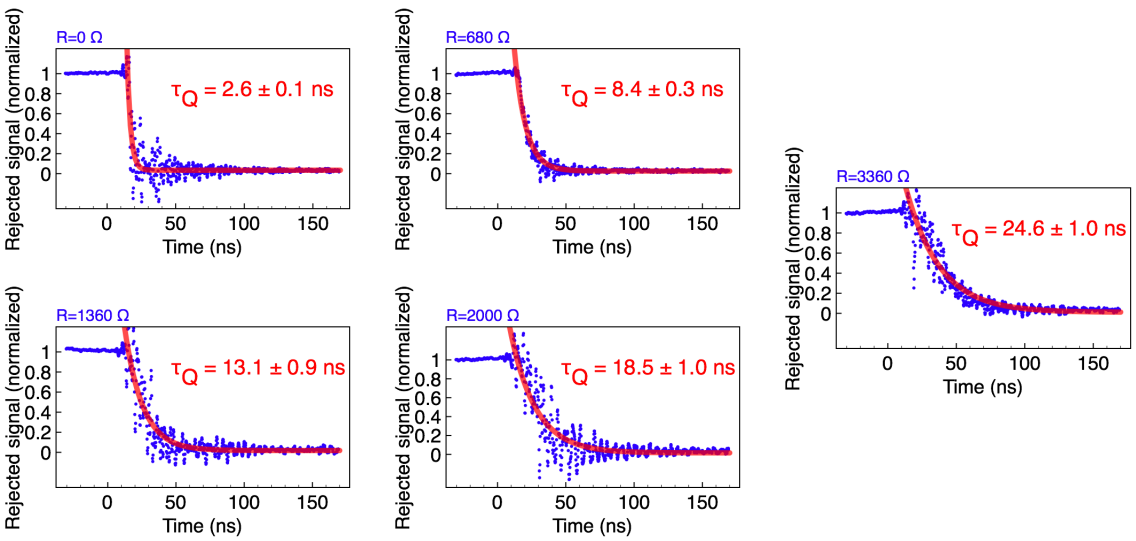

Figure 2.9: Q-switching speed measurements. Different resistors are wired in series with the high voltage electrode of the Pockels' cell in order to modify the the high voltage switching speed. Blue dots: experimental data; Red line: exponential fit to extract the switching time τ_Q

depth of the temporal pulse shapes, assuming the resonant seeded mode and its adjacent mode are lasing simultaneously, we calculate the intensity contrast of these two frequency components.

The blue curves in Figure 2.10(b) on the left are measured temporal profiles at different Q-switching speed when the cavity is locked on resonance with the injected frequency. The blue dots in Figure 2.10(a) are the corresponding intensity contrast of the resonant seeded mode over its adjacent mode. With 60 mW of injected power, even though with zero detuning, the single mode quality is still poor at very fast Q-switch opening (2.6 ns switching time). As the Q-switch opening becomes slower, the pulse shows less temporal spikes and becomes smoother. The intensity contrast increases almost by two orders of magnitude as the switching time is slowed down from 2.6 ns to 24.6 ns. The red curves are from simulation using the model described in the next sub-section.

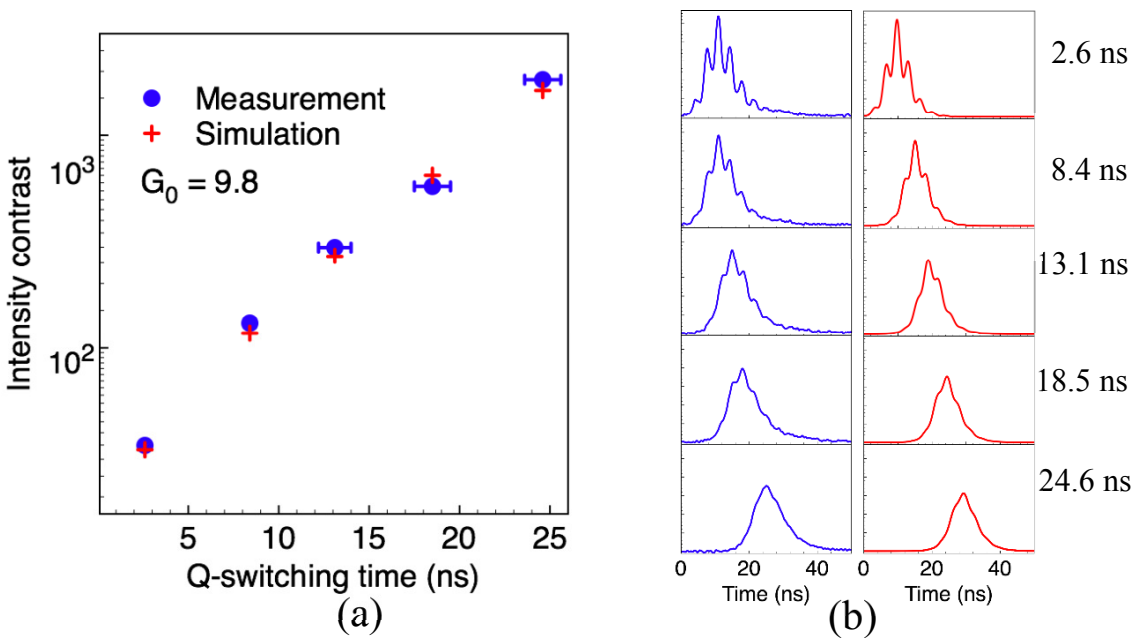

Figure 2.10: (a) Intensity contrast of the resonant seeded mode over its adjacent mode at different Q-switch opening times. (b) Temporal pulse shapes at different Q-switch opening time. The temporal positions of theses pulses show their relative arriving time. Blue on the left: experimental measurement with zero detuning; Red on the right: simulation.

2.5.3 Theoretical model

In presence of a externally injected field $\mathcal{E}_{in}(t)\exp[i(\omega_0 t - kz)]$, we describe the intracavity field by a plane wave $\mathcal{E}_s(t)\exp[i(\omega t - kz)]$(seeded mode), with a time dependent envelope $\mathcal{E}_s(t)$ and a time dependent frequency of which the initial value equals the injected frequency: $\omega(0) = \omega_0$, rattling back and forth in a cavity with mirror reflectivity R_1 and R_2 for the end mirror and the output coupler, respectively, and a gain $\alpha = \sigma\Delta N(t)\ell$. The gain medium is characterized by a gain cross section σ, a time dependent inversion $\Delta N(t)$, and has a length of ℓ. Assuming a constant injected field amplitude $\mathcal{E}_{in}$ (value inside the resonator), the evolution of the seeded mode

then is given by [33, 22]:

$$\mathcal{E}_s(t+\tau_{RT}) = \mathcal{E}_s(t)\sqrt{R_1R_2}T_Q(t)e^{\sigma\Delta N(t)\ell}e^{-i\Delta\omega\tau_{RT}} + \mathcal{E}_{in}. \tag{2.1}$$

$T_Q(t)$ is the internal transmittance which includes the time dependent losses introduced by the Pockels cell and polarizer. The Q-switch transition is modeled as having an exponential time dependence with a characteristic time constant τ_Q:

$$T_Q(t) = T_{Qf} - (T_{Qf} - T_{Qi})e^{-\frac{t}{\tau_Q}}. \tag{2.2}$$

T_{Qi} and T_{Qf} are the initial and final internal transmittance. $\Delta\omega = \omega_0 - \omega_c$ is the detuning of the injected frequency ω_0 from the nearest cavity mode ω_c. Since we are only interested in the resonant case, we choose a zero detuning frequency. As shown in reference [22], Eq. (2.1) is equivalent to the differential equation:

$$\frac{d\mathcal{E}_s}{dt} = m(t)\mathcal{E}_s + \frac{m(t)}{e^{m\tau_{RT}} - 1}\mathcal{E}_{in}, \tag{2.3}$$

where $m(t)$ is the net gain per round-trip:

$$m(t) = \frac{1}{\tau_{RT}}[\ln\sqrt{R_1R_2}T_Q(t) + \sigma\Delta N(t)\ell] \tag{2.4}$$

The injected field affects the field evolution in two ways. The first one is to offer a higher initial condition for the seeded mode as compared to the mode that evolved from spontaneous emission. The second one is the in phase addition of the seed field at each round trip, as described by the second term of the right hand side of Eqs. (2.1) and (2.3). The latter effect manifests itself as a regenerative amplification of the injected field before the cavity reaches its threshold, which is critical for mode selection, as will be detailed below.

Since there is no coherent external field at any other frequency, the evolution of non-seeded modes that build up from spontaneous emission can be described by Eq. (2.3) but without the second term.

$$\frac{d\mathcal{E}(t)}{dt} = m(t)\mathcal{E}(t) \tag{2.5}$$

As the gain depletion occurs in tens of ns, we consider only the stimulated emission and ignore the spontaneous decay, which has a life time of 230 μs:

$$\frac{d\Delta N(t)}{dt} = -2\sigma c\Phi(t)\Delta N(t) \tag{2.6}$$

where $\Phi(t)$ is the photon flux. Both the seeded mode and un-seeded mode fields contribute equally to the photon flux $\Phi(t)$ for stimulated emission in the Nd:YAG medium, in which homogenous broadening is the dominant broadening mechanism.

$$\Phi(t) = \frac{\epsilon}{2h\nu}(|\mathcal{E}_s|^2 + |\mathcal{E}(t)|^2) \tag{2.7}$$

Table 1 is a summary of the parameters that we use in the simulation, matching closely our experimental condition. The injection intensity is calculated from the 60

Table 2.1: Parameters used in simulations

mirror reflectivity: R_1, R_2	0.99, 0.12
internal transmittance at low Q: T_{Qi}	0.06
internal transmittance at high Q: T_{Qf}	0.86
round-trip time: τ_{RT}	3.5137 ns
gain medium length: l	0.115 m
gain cross-section: σ	5×10^{-23}m^2
initial gain above threshold: r	2
CW injection intensity	1300 W/m^2
peak fluorescence intensity per mode	300 W/m^2

mW seed laser, being expanded to 5 mm FWHM, and passing through the output coupler with 12% reflectivity. The intensity of the fluorescence at the non-seeded mode is estimated from measurements. We measure the ratio of the peak fluorescence to the reflection of injected CW seed from the cavity, after passing through a bandpass filter for 1 μm. The intensity ratio is 129 in resonant condition. From the cavity mirror reflectivity and internal loss information we know that the peak fluorescence intensity is 18 times that of the injected intensity. Consider the bandwidth of each cavity mode to be 50 MHz and the fluorescence bandwidth at 1 μm to be 20 GHz, we estimate the peak fluorescence intensity per mode to be 4.5% of the injected

intensity, which is about 60 W/cm^2. The fluorescence intensity per mode that we use in our simulation is instead 300 W/cm^2. We believe this is reasonable because the mode just next to the seeded mode is always preferred to other modes since it is closer to the seed frequency. We don't have a model to describe this preference so we justify it by increasing the initial intensity of that nearest mode by factor of 5, which matches our experimental observation.

2.5.4 Numerical results

Using the parameters in Table 1, we numerically solve Eq. (2.3), (2.5) and (2.6) with different characteristic Q-switch opening time τ_Q that we measure. The mode contrasts obtained from simulation are shown in Figure. 2.10 (a) with red crosses. The possible temporal pulse shapes are shown in Figure. 2.10 (b) on the right in red. The trend of increasing Q-switching opening time leading to increasing mode selectivity on the seeded mode matches well with experimental data.

To better illustrate the effect of Q-switch opening time on mode selectivity, the net round-trip gain and the corresponding Q-switched pulse are plotted at two switching times, shown in Figure. 2.11 (a). The blue solid line is the fast switching case and the black dashed line is the slow switching case. The red dotted line indicate the cavity threshold condition, i.e. net round-trip gain=0. The rising edge of the net gain indicates the Q-switching process and the fall edge indicates the gain depletion. Before the cavity reaches its threshold, the seeded mode is regeneratively amplified because of the cumulative seed field addition at each round trip (second term of Eq. (2.3)). The non-seeded mode, however, experiences loss until the cavity reaches its threshold. As the Q-switch opening time is slowed down, the time of threshold gets delayed and so does the build-up of the non-seeded mode. The seeded mode, because of the regenerative amplification before threshold, suffers less delay in its

build-up. This leads to an overall increase of build-up time difference between the seeded mode and non-seeded mode. When the build-up time difference is longer than one temporal pulse width, the seeded mode depletes the population inversion before the non-seeded mode builds up to a comparable level, resulting in a high contrast single mode output.

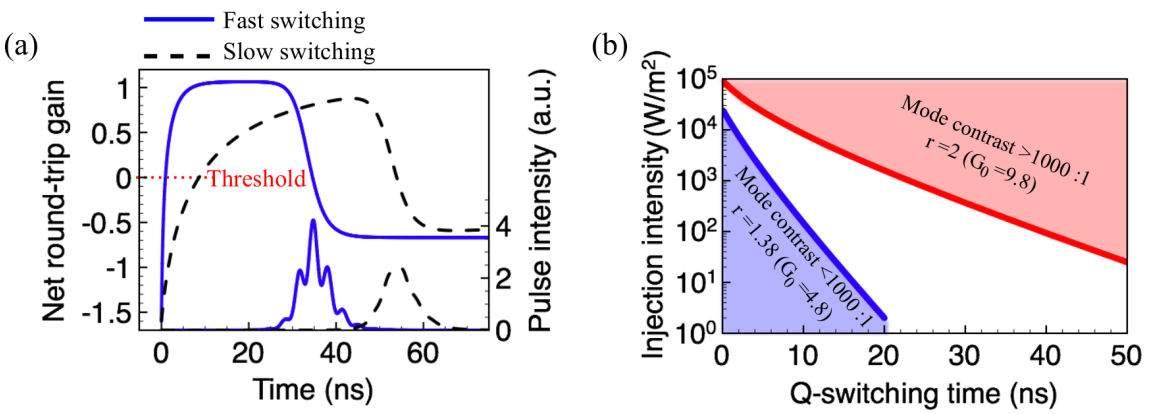

Figure 2.11: (a) Net round-trip gain evolution and Q-switched pulse with different switching time. The red dotted line indicates the cavity is at threshold, i.e. net round-trip gain =0. (b) Phase diagram for high contrast single mode operation. When the laser is pumped at twice above threshold (single pass small signal gain =9.8), the red area shows where the mode contrast >1000:1 can be achieved. At lower gain, this area becomes bigger and the blue area shows where the mode contrast is less than 1000:1.

Figure. 2.11 (b) shows the phase diagram for high contrast single mode operation under different pumping conditions, injection intensities and Q-switch opening time. For pumping twice above threshold, which is typical for high energy flashlamp pumped Q-switched Nd:YAG laser, with a CW seeder with power of a couple mW to a couple tens of mW corresponding to intensity of 10^2 to 10^3W/m^2, the Q-switching opening time should be slowed down to 20 to 40 ns in order to achieve mode contrast of 1000:1. Lowering the gain makes the single mode window much wider, as shown in the blue curve.

2.5.5 Energy reduction problem

We observe an energy reduction of about 10% when the laser is injection seeded and working in single mode. Similar phenomena was also mentioned in literature [32]. The reason is, instead of owing to the in-homogeneously broadening of two transitions

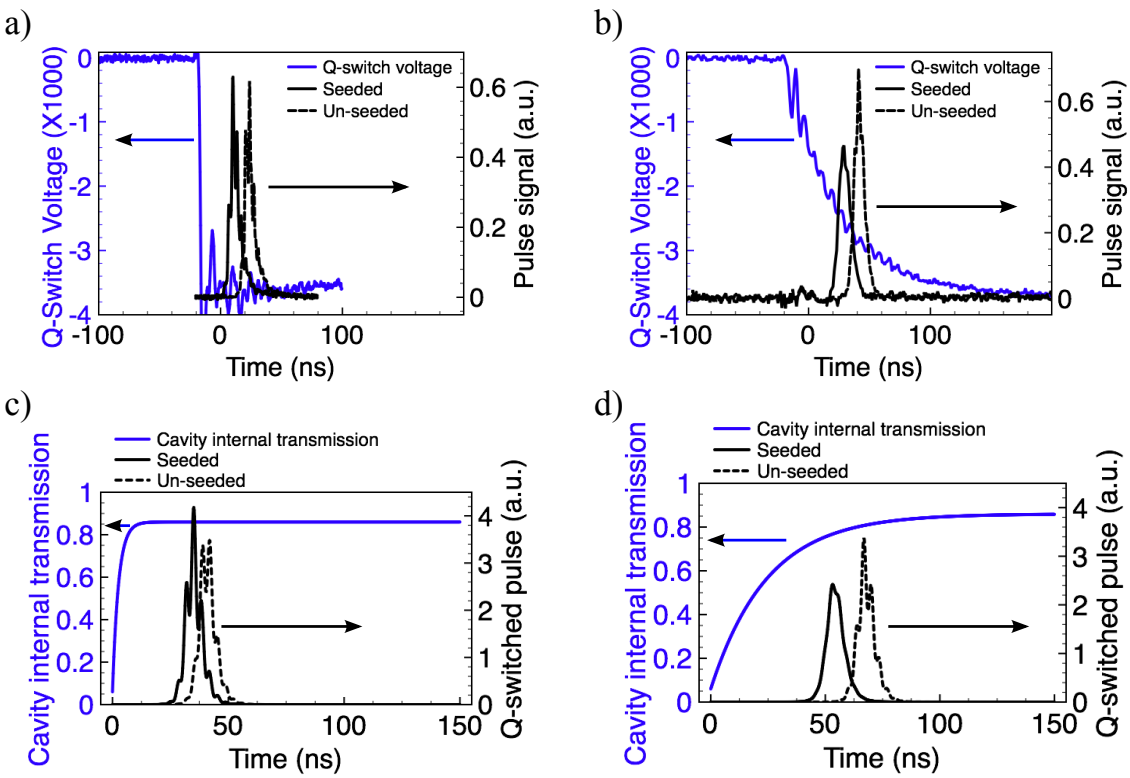

Figure 2.12: (a) Measured Q-switch voltage and pulse in fast switching case. (b) Measured Q-switch voltage and pulse in slow switching case. (c) Simulated cavity internal transmission and Q-switched pulse in fast switching case. (d) Simulated cavity internal transmission and Q-switched pulse in slow switching case.

of 1.064 and 1.0645 μm in Nd:YAG [32], due to the slow Q-switch that is necessary for good single performance. We measure the seeded and un-seeded Q-switched pulse in both fast and slow switching case, as shown in figure 2.12 (a) and (b). Only in the slow switching case we observe energy reduction, while the cavity is operated in

seeded mode. The high DC voltage applied on the Pockels cell is also measured at the same time, using a high voltage probe with 2 ns response time, and plotted in figure 2.12 (a) and (b). As measured in figure 2.12 (a), the pulse leaves the cavity after the loss is switched to its minimum in both seeded and un-seeded modes. All the population inversion is dumped in both cases and the pulse energies are the same. In figure 2.12(b), however, as the voltage is switched on slowly, the pulse leaves the cavity before the loss is switched to its minimum. The pulse builds up faster and leaves the cavity earlier in injection seeded mode , thus "see" more cavity loss than the pulse in un-seeded mode and has less energy. The energy reduction problem due to slow Q-switch can also be explained in the model we describe in section 2.5.3, as shown in figure 2.12(c) and (d).

The reduction of output energy, is the compromise of high gain, high single mode purity and low injection power. We can keep the same pulse energy and good single mode quality with high injection power and fast Q-switch, as we analyzed in section 2.5.3. However, when the relatively low power, CW single mode seeder is more convenient and accessible, 10% energy reduction is okay for good single mode Q-switched laser.

Chapter 3

Pulse compression by Stimulated Brillouin Scattering

3.1 Introduction

The efficiency of many nonlinear light-matter interaction processes critically depends on the peak power of the laser pulse. This is particularly true in the cases of higher-order processes such as multi-photon ionization of gaseous nitrogen and filamentation in air, where the required peak power exceeds gigawatt. Pulse compression is a family of techniques commonly used to increase the peak power of laser pulses. In the ultra-short (<ps) regime, method such as chirp compensation compresses an optical pulse to the Fourier-transform-limited duration. These methods are however generally not feasible for ns pulses.

Pulse compression from ns to the sub-ns regime is commonly achieved by utilizing nonlinear light-matter interactions. Stimulated Brillouin scattering (SBS) is a classic example of this type of technique. In its simplest realization, a high-energy laser pulse is focused into a SBS active medium. At the focus the field is strong enough to

initiate a backward scattered "Stokes" field which interferes with the remaining of the incoming field and produces a standing wave. Due to electrostriction, through which the material tends to concentrate where the light field is stronger, the standing wave generates a density grating (i.e. phonon field). Meanwhile, the expanding phonon field, acting like a "moving" mirror, back scatters more energy from the incident field into the Stokes field, leading to depletion of the incident pulse and a compressed Stokes pulse with a sharp rising edge. The result is an optical pulse with most of the initial energy but with much reduced temporal width.

Pulse compression by SBS was first demonstrated by Hon [34]. Kmetik [35] showed stable SBS compression in liquid fluorocarbon FC-75 at 1064 nm. The liquid fluorocarbon family has remained the medium of choice in subsequent studies [36, 37, 17, 38, 39] for its short phonon lifetime, high SBS gain and low absorption in a broad spectral range from the visible to near infrared. Schiemann *et al* [40, 41, 42, 43] showed that water can also be used as a SBS medium at 532 nm. However, their study was limited to low energy and therefore low peak power amplification. Dane [44] pioneered a parallel two-cell configuration for SBS pulse compression which increased the energy capacity of the method to more than 1 J and achieved a peak power of 1 GW in 1 ns pulses.

The SBS pulse compressor is a critical component in our UV source. A huge amount of effort has been spent on designing and optimizing its performance for UV filamentation experiments and the results are summarized here. This chapter is organized as follows. We first describe the theory behind SBS pulse compression and numerical methods to simulate the process. We then focus on experimental realization using liquid fluorocarbon (FC72) as the SBS active medium. Two geometries, the single-cell and the generator-amplifier configuration, were extensively studied, optimized and compared. It was then realized that the unfavorable thermo-optic property of FC72 ultimately limits the energy capacity of the setup. To address this,

we switched to water as the SBS gain medium and discuss the tradeoffs. Ultimately, we achieved output pulses of $\sim$ 500ps, 1 J at 1064 nm (using FC72) and $\sim$ 300 ps, 1.2 J at 532 nm (using water) which, after converting to 266 nm, meet the theoretical requirements for filamentation in air.

3.2 Theoretical modeling

3.2.1 Principle of SBS pulse compression

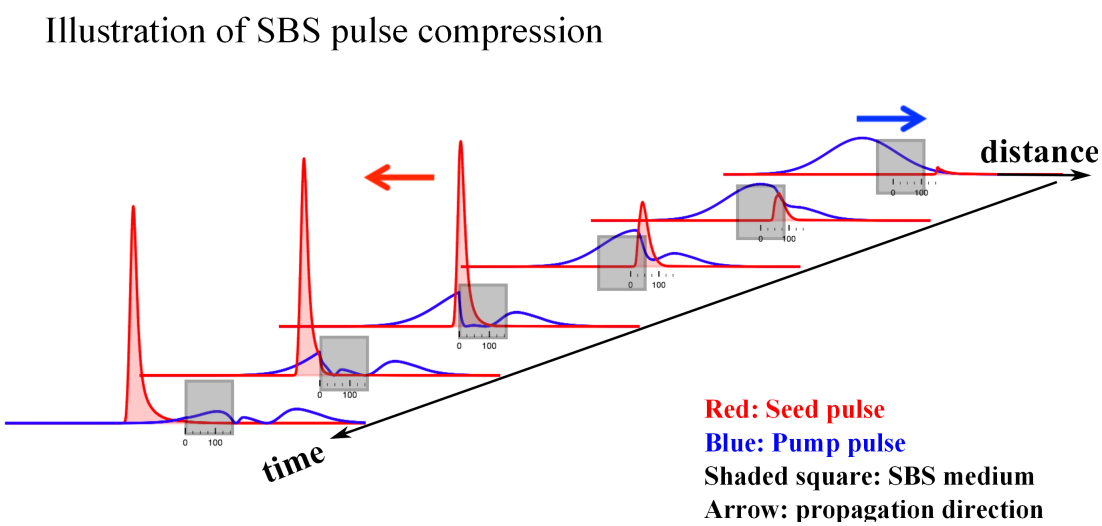

Figure 3.1: Illustration of pulse compression process by Stimulated Brillioun Scattering (SBS), see text for details

Since its first demonstration in 1980 [34], SBS pulse compression has evolved from the tapered waveguide geometry [45, 46], the single long focusing setup [45] to the cascaded-two-cell arrangement [47] and eventually the parallel-two-cell configuration [44]. The principle of SBS pulse compression is based on the strong interaction between the pump and the Stokes and depletion of the pump. The Stokes pulse

is either generated from the pump pulse's leading edge via SBS (i.e. the tapered wave-guide, single focusing and cascaded-two-cell setup), or pre-generated using a separated pump pulse (i.e. the parallel-two-cell setup). As illustrated in Fig. 3.7(a), the pump pulse (blue, from left to right) and the Stokes pulse (red, from right to left) are counter-propagating inside the SBS medium (shaded area). The interference between them creates a growing density grating that scatters the energy from the pump into the leading edge of the Stokes, which, with sufficient interaction length, leads to a compressed, amplified Stokes pulse with a sharp leading edge.

Here, we layout a comprehensive theoretical treatment of the SBS generation which is the foundation for numerical simulations. Our treatment is based on the pioneering work of Veltchev [48] with modifications. The following derivation is in SI unit.

3.2.2 Optical and density waves coupled equations

The spatial evolution of the optical fields is described by the following wave equation [49],

$$\frac{\partial^2 \tilde{E}_i}{\partial z^2} - \frac{1}{(c/n)^2}\frac{\partial^2 \tilde{E}_i}{\partial t^2} = \frac{1}{\epsilon_0 c^2}\frac{\partial^2 \tilde{P}_i}{\partial t^2}, \qquad i = 1, 2 \tag{3.1}$$

where $\tilde{E_1}$ is the incoming(pump) wave and $\tilde{E_2}$ is the reflecting(stokes) wave. The two fields are counter-propagating according to

$$\tilde{E}_1(t, z) = \frac{1}{2}\mathcal{E}_1(t, z)e^{i(\omega_1 t - k_1 z)} + c.c. \tag{3.2a}$$

$$\tilde{E}_2(t, z) = \frac{1}{2}\mathcal{E}_2(t, z)e^{i(\omega_2 t + k_2 z)} + c.c. \tag{3.2b}$$

For Brillouin scattering induced by electrostriction, the nonlinear polarization which gives rise to the source terms for the pump and stokes fields comes from the change of

dielectric constant by electrostriction (i.e. change of dielectric constant from change of material density). Thus the total nonlinear polarization on the right hand side of Eq. 3.1 is [49]

$$\tilde{P} = \epsilon_0 \Delta\chi \tilde{E} = \epsilon_0 \Delta\epsilon \tilde{E} = \epsilon_0 \gamma_e \frac{\tilde{\rho}}{\rho_0} \tilde{E} \tag{3.3}$$

where $\gamma_e = \rho_0(\partial\epsilon/\partial\rho)$ is the electostrictive constant of the material. The density wave $\tilde{\rho}$, which describes the spatio-temporal material density distribution, can be written as

$$\tilde{\rho}(t,z) = \rho_0 + [\frac{1}{2}\rho(t,z)e^{i(\Omega t - qz)} + c.c.] \tag{3.4}$$

where ρ_0 represents the mean density of the medium. For Stimulated Brillouin scattering, the density wave is induced by the interference between the pump and Stokes field. $\rho(t,z)$ is the induced density fluctuation distribution. From the conservation of momentum and energy, the k vector and frequency of the density wave satisfy

$$\mathbf{q} = \mathbf{q_B} = \mathbf{k_1} - \mathbf{k_2} \approx 2\mathbf{k_1} \tag{3.5}$$

$$\Omega = \Omega_B = \omega_1 - \omega_2 \tag{3.6}$$

Consequently, we have

$$\tilde{\rho}(t,z) = \rho_0 + [\frac{1}{2}\rho(t,z)e^{i(\Omega_B t - q_B z)} + c.c.] \tag{3.7}$$

The material density obeys the acoustic wave equation

$$\frac{\partial^2\tilde{\rho}}{\partial t^2} - \Gamma'\nabla^2\frac{\partial\tilde{\rho}}{\partial t} - v^2\nabla^2\tilde{\rho} = \nabla\cdot\mathbf{f} \tag{3.8}$$

where b is the sound velocity in the material, Γ' is the damping parameter and $\mathbf{f}$ is the electrostrictive force per unit volume given by

$$\mathbf{f} = \nabla p_{st}, \qquad p_{st} = -\frac{1}{2}\epsilon_0\gamma_e < \tilde{E}^2 > \tag{3.9}$$

and p_{st} is the electrostrictive pressure. $\tilde{E}$ is the total electric field. The time average should be understood as averaging over many optical cycles since the material density can only respond to low frequency components of the field (GHz).
The total electric field is the sum of the pump and Stokes fields and we have

$$\begin{aligned}\tilde{E}^2 &= (\tilde{E_1} + \tilde{E_2})^2 \\ &= \tilde{E_1}^2 + \tilde{E_2}^2 + 2\tilde{E_1}\tilde{E_2}\end{aligned}$$

$$\begin{aligned}\tilde{E_1}^2 &= (\frac{1}{2}\mathcal{E}_1(t,z)e^{i(\omega_1 t - k_1 z)} + c.c.)^2 \\ &= \frac{1}{4}\mathcal{E}_1^2 e^{2i(\omega_1 t - k_1 z)} + \frac{1}{4}\mathcal{E}_1^{*2} e^{-2i(\omega_1 t - k_1 z)} + \frac{1}{2}\mathcal{E}_1^2\end{aligned}$$

$$\begin{aligned}\tilde{E_2}^2 &= (\frac{1}{2}\mathcal{E}e^{i(\omega_2 t + k_2 z)} + c.c.)^2 \\ &= \frac{1}{4}\mathcal{E}_2^2 e^{2i(\omega_2 t + k_2 z)} + \frac{1}{4}\mathcal{E}_2^{*2} e^{-2i(\omega_2 t + k_2 z)} + \frac{1}{2}\mathcal{E}_2^2\end{aligned}$$

$$\tilde{E_1}\tilde{E_2} = \frac{1}{4}\mathcal{E}_1\mathcal{E}_2 e^{i(\omega_1+\omega_2)t}e^{i(k_2-k_1)z} + \frac{1}{4}\mathcal{E}_1\mathcal{E}_2^* e^{i(\omega_1-\omega_2)t}e^{-i(k_1+k_2)z} + c.c.$$

and their time averages are

$$\begin{aligned}< \tilde{E_1^2} > &= \frac{1}{2}|\mathcal{E}_1|^2 \\ < \tilde{E_2^2} > &= \frac{1}{2}|\mathcal{E}_2|^2 \\ 2 < \tilde{E_1^2}\tilde{E_2^2} > &= \frac{1}{2}\mathcal{E}_1\mathcal{E}_2^* e^{i(\omega_1-\omega_2)t}e^{-i(k_1+k_2)z} + c.c. \\ &= \frac{1}{2}\mathcal{E}_1\mathcal{E}_2^* e^{i(\Omega_B t - q_B z)} + c.c.\end{aligned}$$

As a result, the right-hand-side of Eqaution 3.8 is

$$\begin{aligned}\nabla \cdot \mathbf{f} = \nabla^2 p_{st} &= -\frac{1}{2}\epsilon_0\gamma_e\nabla^2 < \tilde{E}^2 > \\ &= -\frac{1}{2}\epsilon_0\gamma_e\nabla^2[\frac{1}{2}\mathcal{E}_1\mathcal{E}_2^* e^{i(\Omega_B t - q_B z)} + c.c.] \\ &= \frac{1}{4}\epsilon_0\gamma_e q_B^2[\mathcal{E}_1\mathcal{E}_2^* e^{i(\Omega_B t - q_B z)} + c.c.]\end{aligned}$$

$$\nabla \cdot \mathbf{f} = \frac{1}{4}\epsilon_0 \gamma_e q_B^2 [\mathcal{E}_1 \mathcal{E}_2^* e^{i(\Omega_B t - q_B z)} + c.c.] \tag{3.10}$$

The treatment of density wave (Eq. 3.8) is similar to Refs. [43, 48]. First, we note that the density wave is considered as a ultra short pulse because the Brillouin bandwidth is comparable to the Brillouin frequency, the slowly-varying-envelope approximation does not applied here. Plug Eq. 3.7 into 3.8, we get

$$\begin{aligned}
\frac{\partial \tilde{\rho}}{\partial t} &= \frac{1}{2}[\frac{\partial \rho(t,z)}{\partial t} + i\Omega_B \rho(t,z)]e^{i(\Omega_B t - q_B z)} + c.c. \\
\frac{\partial^2 \tilde{\rho}}{\partial t^2} &= \frac{1}{2}[\frac{\partial^2 \rho(t,z)}{\partial t^2} + 2i\Omega_B \frac{\partial \rho(t,z)}{\partial t} - \Omega_B^2 \rho(t,z)]e^{i(\Omega_B t - q_B z)} + c.c.
\end{aligned}$$

Assume that the phonon wave doesn't move along z within the timescale we consider, we make the approximation that

$$\begin{aligned}
\nabla^2 \frac{\partial \tilde{\rho}}{\partial t} &\approx -\frac{1}{2} q_B^2 [\frac{\partial \rho(t,z)}{\partial t} + i\Omega_B \rho(t,z)]e^{i(\Omega_B t - q_B z)} + c.c. \\
\nabla^2 \tilde{\rho} &\approx -\frac{1}{2} q_B^2 \rho(t,z) e^{i(\Omega_B t - q_B z)} + c.c.
\end{aligned}$$

and Eq. 3.8 becomes

$$\begin{aligned}
\frac{1}{2}\frac{\partial^2 \rho(t,z)}{\partial t^2} + (\frac{1}{2}\Gamma' q_B^2 + i\Omega_B)\frac{\partial \rho(t,z)}{\partial t} + (v^2 q_B^2 - i\Omega_B \Gamma' q_B^2 - \Omega_B^2)\rho(t,z) + c.c. \\
&= \nabla \cdot \mathbf{f} \\
&= \frac{1}{4}\epsilon_0 \gamma_e q_B^2 (\mathcal{E}_1 \mathcal{E}_2^* + c.c.)
\end{aligned} \tag{3.11}$$

The wave number, frequency and velocity of the density wave are related by

$$q_B = \frac{\Omega_B}{v} \tag{3.12}$$

so Eq. 3.11 becomes

$$\frac{\partial^2 \rho(t,z)}{\partial t^2} + (\Gamma_B + 2i\Omega_B)\frac{\partial \rho(t,z)}{\partial t} + i\Omega_B \Gamma_B \rho(t,z) = \frac{1}{2}\epsilon_0 \gamma_e q_B^2 \mathcal{E}_1 \mathcal{E}_2^* \tag{3.13}$$

where we have defined

$$\Gamma_B = \Gamma' q_B^2 \tag{3.14}$$

as the Brillouin line-width of the material.

We solve Eq. 3.13 in the Fourier domain. First, utilizing that $\frac{\partial}{\partial t} = i\Omega$ and $\frac{\partial^2}{\partial t^2} = -\Omega^2$, we have, in the frequency domain

$$-\Omega^2\widetilde{\rho}(z,\Omega) + i\Omega(\Gamma_B + 2i\Omega_B)\widetilde{\rho}(z,\Omega) + i\Omega_B\Gamma_B\widetilde{\rho}(z,\Omega) = \frac{1}{2}\epsilon_0\gamma_e q_B^2\widetilde{\mathcal{E}_1\mathcal{E}_2^*} \tag{3.15}$$

so

$$\begin{aligned}\widetilde{\rho}(z,\Omega) &= \frac{-\epsilon_0\gamma_e q_B^2\widetilde{\mathcal{E}_1\mathcal{E}_2^*}/2}{\Omega^2 + 2\Omega_B\Omega - i\Gamma_B(\Omega+\Omega_B)} \\ &= \frac{-\epsilon_0\gamma_e q_B^2\widetilde{\mathcal{E}_1\mathcal{E}_2^*}/2}{(\Omega+\Omega_B)^2 - \Omega_B^2 - i\Gamma_B(\Omega+\Omega_B)}\end{aligned} \tag{3.16}$$

We subsequently define

$$\widetilde{g}(\Omega) = \frac{\Omega_B}{(\Omega+\Omega_B)^2 - \Omega_B^2 - i\Gamma_B(\Omega+\Omega_B)} \tag{3.17}$$

as the gain profile of the SBS process, which has resonances at $\Omega + \Omega_B = \pm\Omega_B$. The two resonances correspond to the Stokes and anti-Stokes of the Brillouin scattering process. The density wave in the Fourier domain is

$$\widetilde{\rho}(\Omega,z) = -\frac{\epsilon_0\gamma_e q_B^2}{\Omega_B}\widetilde{g}(\Omega)\widetilde{\mathcal{E}_1\mathcal{E}_2^*}/2 \tag{3.18}$$

Correspondingly, in the time domain,

$$\rho(t,z) = -\frac{\epsilon_0\gamma_e q_B^2}{\Omega_B}g(t) * \mathcal{E}_1\mathcal{E}_2^*/2 \tag{3.19}$$

in which $*$ is the convolution. The gain profile in the time domain is

$$g(t) = \frac{1}{\sqrt{2\pi}}\int_{-\infty}^{\infty}\frac{\Omega_B}{(\Omega+\Omega_B)^2 - \Omega_B^2 - i\Gamma_B(\Omega+\Omega_B)}e^{-i\Omega t}d\Omega \tag{3.20}$$

To evaluate Eq.3.20, we examine the integrand

$$\begin{aligned}f(\Omega) &= \frac{\Omega_B e^{-i\Omega t}}{(\Omega+\Omega_B)^2 - \Omega_B^2 - i\Gamma_B(\Omega+\Omega_B)} \\ &= \frac{\Omega_B e^{-i\Omega t}}{[\Omega - (-\Omega_B + \frac{i\Gamma_B}{2} + \sqrt{\Omega_B^2 - \frac{\Gamma_B^2}{4}})]\cdot[\Omega - (-\Omega_B + \frac{i\Gamma_B}{2} - \sqrt{\Omega_B^2 - \frac{\Gamma_B^2}{4}})]}\end{aligned}$$

$f(\Omega)$ has two poles Ω_1 and Ω_2 in the upper half:

$$\Omega_1 = -\Omega_B + \frac{i\Gamma_B}{2} + \sqrt{\Omega_B^2 - \frac{\Gamma_B^2}{4}}$$
$$\Omega_2 = -\Omega_B + \frac{i\Gamma_B}{2} - \sqrt{\Omega_B^2 - \frac{\Gamma_B^2}{4}}$$

The integral of Eq. 3.20 equals to the contour integral:

$$g(t) = \frac{1}{\sqrt{2\pi}} \oint_C f(\Omega) d\Omega \tag{3.21}$$

When $t \geq 0$, the complete contour runs from $-\infty$ to $+\infty$ of the $Re(\Omega)$ axis and a semi-circle in the upper half of the complex plane. The integral in Eq. 3.20 can be evaluated using the Residue theorem,

$$\begin{aligned}
g(t) &= \frac{1}{\sqrt{2\pi}} 2\pi i (\mathrm{Res}(f(\Omega))|_{\Omega_1} + \mathrm{Res}(f(\Omega))|_{\Omega_2}) \\
&= \frac{1}{\sqrt{2\pi}} 2\pi i \left(\frac{\Omega_B e^{i\Omega_1 t}}{\Omega_1 - \Omega_2} + \frac{\Omega_B e^{i\Omega_2 t}}{\Omega_2 - \Omega_1}\right) \\
&= \frac{\sqrt{2\pi} i \Omega_B}{\Omega_1 - \Omega_2} (e^{i\Omega_1 t} - e^{i\Omega_2 t}) \\
&= \frac{\sqrt{2\pi} i \Omega_B}{2\sqrt{\Omega_B^2 - \frac{\Gamma_B^2}{4}}} e^{i(-\Omega_B + i\frac{\Gamma_B}{2})t} (e^{i\sqrt{\Omega_B^2 - \frac{\Gamma_B^2}{4}}t} - e^{-i\sqrt{\Omega_B^2 - \frac{\Gamma_B^2}{4}}t}) \\
&= \frac{-\sqrt{2\pi}\Omega_B}{\sqrt{\Omega_B^2 - \frac{\Gamma_B^2}{4}}} e^{-i\Omega_B t} e^{-\frac{\Gamma_B}{2}t} \sin\left(\sqrt{\Omega_B^2 - \frac{\Gamma_B^2}{4}}t\right)
\end{aligned}$$

When $t < 0$, the complete contour runs from $-\infty$ to $+\infty$ of the $Re(\Omega)$ axis and a semi-circle in the lower half. Since $f(\Omega)$ has no pole in the lower half, the Integral 3.21 equals zero. So the transient gain $g(t)$ has an exact solution,

$$g(t) = \begin{cases} \frac{-\sqrt{2\pi}\Omega_B}{\sqrt{\Omega_B^2 - \frac{\Gamma_B^2}{4}}} e^{-i\Omega_B t} e^{-\frac{\Gamma_B}{2}t} \sin\left(\sqrt{\Omega_B^2 - \frac{\Gamma_B^2}{4}}t\right) & \text{if } x \geq 0 \\ 0 & \text{if } x < 0 \end{cases} \tag{3.22}$$

and it decays with a characteristic time $\tau_p = 1/\Gamma_B$, which is the phonon lifetime. The phonon wave is coupled with the optical waves via Eq. 3.19 and 3.22.

For the optical waves, the slowly-varying-envelope approximation (S.V.E.A.) applies since the pulse width of interest is hundreds of pico-seconds. With the S.V.E.A, the optical wave (Eq. 3.1) can be rewritten as

$$ik_1(\frac{\partial \mathcal{E}_1}{\partial z} + \frac{1}{c/n}\frac{\partial \mathcal{E}_1}{\partial t})e^{i(\omega_1 t - k_1 z)} + c.c. = \frac{1}{\epsilon_0 c^2}\frac{\partial^2 \tilde{P}_1}{\partial t^2} \tag{3.23a}$$

$$ik_2(-\frac{\partial \mathcal{E}_2}{\partial z} + \frac{1}{c/n}\frac{\partial \mathcal{E}_2}{\partial t})e^{i(\omega_2 t + k_2 z)} + c.c. = \frac{1}{\epsilon_0 c^2}\frac{\partial^2 \tilde{P}_2}{\partial t^2} \tag{3.23b}$$

Now choose only the phase-matched source terms on the right-hand-side of Eqs. 3.23, meaning:

$$\tilde{P}_1 = \frac{1}{2}P_1 e^{i(\omega_1 t - k_1 z)} + c.c.$$
$$\tilde{P}_2 = \frac{1}{2}P_2 e^{i(\omega_2 t + k_2 z)} + c.c.$$

and continue on the nonlinear polarization source term in Eq. 3.3,

$$\begin{aligned}\tilde{P} &= \epsilon_0 \gamma_e \frac{\tilde{\rho}}{\rho_0}\tilde{E} \\ &= \frac{\epsilon_0 \gamma_e}{\rho_0}[\frac{1}{2}\rho e^{-i(k_1+k_2)z}e^{i(\omega_1-\omega_2)t} + c.c.] \cdot [\frac{1}{2}\mathcal{E}_1 e^{i(\omega_1 t - k_1 z)} + \frac{1}{2}\mathcal{E}_2 e^{i(\omega_2 t + k_2 z)} + c.c.] \\ &= \frac{\epsilon_0 \gamma_e}{\rho_0}[\underbrace{\frac{1}{4}\rho \mathcal{E}_2 e^{i(\omega_1 t - k_1 z)} + c.c.}_{\tilde{P}_1} + \underbrace{\frac{1}{4}\rho^* \mathcal{E}_1 e^{i(\omega_2 t + k_2 z)} + c.c.}_{\tilde{P}_2} + ...]\end{aligned} \tag{3.24}$$

We introduce Eq. 3.24 into the optical wave equations 3.23, and apply the S.V.E.A,

$$\frac{\partial \mathcal{E}_1}{\partial z} + \frac{1}{c/n}\frac{\partial \mathcal{E}_1}{\partial t} = \frac{i\gamma_e \omega_1}{4nc\rho_0}\rho \mathcal{E}_2 \tag{3.25a}$$

$$-\frac{\partial \mathcal{E}_2}{\partial z} + \frac{1}{c/n}\frac{\partial \mathcal{E}_2}{\partial t} = \frac{i\gamma_e \omega_2}{4nc\rho_0}\rho^* \mathcal{E}_1 \tag{3.25b}$$

The coupled optical wave equations 3.25 and density wave equations 3.19, 3.22 are to be solved numerically. The pump and Stokes frequency are very close since the Brillouin shift is only sub GHz to GHz. So we can make the assumption $\omega_1 \approx \omega_2 = \omega$.

The steady state Brillouin gain g_B is a material property, the derivation of which can be found in [49].

$$g_B = \frac{\gamma_e^2 \omega^2}{n c^3 v \rho_0 \Gamma_B} \tag{3.26}$$

With Eq. 3.26, the optical waves as well as the density wave equations can be rewritten in the following forms

$$\begin{cases} \frac{\partial \mathcal{E}_1}{\partial t} + c/n \frac{\partial \mathcal{E}_1}{\partial z} = -i\epsilon_0 c^2 g_B \Gamma_B \rho' \mathcal{E}_2 \\ \frac{\partial \mathcal{E}_2}{\partial t} - c/n \frac{\partial \mathcal{E}_2}{\partial z} = -i\epsilon_0 c^2 g_B \Gamma_B \rho'^* \mathcal{E}_1 \\ \rho'(t) = \frac{1}{8} g(t) * \mathcal{E}_1 \mathcal{E}_2^* = \frac{1}{8\sqrt{2\pi}} \int_0^t g(t-\tau) \mathcal{E}_1(\tau) \mathcal{E}_2^*(\tau) d\tau \end{cases} \tag{3.27}$$

Equations 3.27 are used to simulate the dynamics of the SBS process.

3.2.3 Numerical implementation

To solve Eqs. 3.27 numerically we use the split-step method (reference). By introducing a propagation operator $\hat{P} = c/n \frac{\partial}{\partial z}$ and a nonlinearity operator $\hat{N} = -i\epsilon_0 c^2 g_B \Gamma_B \rho'$, the optical wave equations in Eqs. 3.27 can be rewritten in a matrix form as

$$\frac{\partial}{\partial t} \begin{pmatrix} \mathcal{E}_1 \\ \mathcal{E}_2 \end{pmatrix} = \left(\begin{bmatrix} 0 & \hat{N} \\ -\hat{N}^* & 0 \end{bmatrix} + \begin{bmatrix} -\hat{P} & 0 \\ 0 & \hat{P}^* \end{bmatrix} \right) \begin{pmatrix} \mathcal{E}_1 \\ \mathcal{E}_2 \end{pmatrix} \tag{3.28}$$

For a small time step Δt, the propagation and nonlinearity operator can be treated as acting independently on the field,

$$\begin{pmatrix} \mathcal{E}_1(t+\Delta t, z) \\ \mathcal{E}_2(t+\Delta t, z) \end{pmatrix} = \exp\left(\begin{bmatrix} 0 & \hat{N} \\ -\hat{N}^* & 0 \end{bmatrix} \Delta t \right) \cdot \exp\left(\begin{bmatrix} -\hat{P} & 0 \\ 0 & \hat{P}^* \end{bmatrix} \Delta t \right) \cdot \begin{pmatrix} \mathcal{E}_1(t, z) \\ \mathcal{E}_2(t, z) \end{pmatrix} \tag{3.29}$$

Firstly we look at what the propagation operator does on the field. The propagation operator in Fourier domain is $\widetilde{\hat{P}} = ic/nk_z$ so

$$\begin{aligned}\exp\left(\begin{bmatrix}-\hat{P} & 0\\ 0 & \hat{P}^*\end{bmatrix}\Delta t\right)\cdot\begin{pmatrix}\mathcal{E}_1(t,z)\\ \mathcal{E}_2(t,z)\end{pmatrix} &= \mathcal{F}^{-1}\begin{pmatrix}e^{ic/nk_z\Delta t}\widetilde{\mathcal{E}}_1(t,k_z)\\ e^{-ic/nk_z\Delta t}\widetilde{\mathcal{E}}_2(t,k_z)\end{pmatrix}\\ &= \begin{pmatrix}\int_{-\infty}^{\infty}e^{ic/nk_z\Delta t}e^{-ik_z z}\widetilde{\mathcal{E}}_1(t,k_z)dk_z\\ \int_{-\infty}^{\infty}e^{-ic/nk_z\Delta t}e^{-ik_z z}\widetilde{\mathcal{E}}_2(t,k_z)dk_z\end{pmatrix}\\ &= \begin{pmatrix}\mathcal{E}_1(t,z-c/n\Delta t)\\ \mathcal{E}_2(t,z+c/n\Delta t)\end{pmatrix}\end{aligned} \tag{3.30}$$

After a time step Δt, the propagation operator shifts the field by $\pm c/n\Delta t$ in space. We then look at the nonlinearity operator $\hat{N}$.

$$\begin{bmatrix}0 & \hat{N}\\ -\hat{N}^* & 0\end{bmatrix}^2 = \begin{bmatrix}-\hat{N}\hat{N}^* & 0\\ 0 & -\hat{N}\hat{N}^*\end{bmatrix} = -|\hat{N}|\hat{\mathbb{1}}$$

$$\exp\left(\begin{bmatrix}0 & \hat{N}\\ -\hat{N}^* & 0\end{bmatrix}\Delta t\right) = \exp\left(i|\hat{N}|\begin{bmatrix}0 & \frac{-i\hat{N}}{|\hat{N}|}\\ \frac{-i\hat{N}^*}{|\hat{N}|} & 0\end{bmatrix}\Delta t\right) = e^{i|\hat{N}|\hat{\sigma}_n\Delta t} \tag{3.31}$$

in which

$$\hat{\sigma}_n = \begin{bmatrix}0 & \frac{-i\hat{N}}{|\hat{N}|}\\ \frac{-i\hat{N}^*}{|\hat{N}|} & 0\end{bmatrix}, \hat{\sigma}_n^2 = \hat{\mathbb{1}} \tag{3.32}$$

We can make use of the mathematical properties of matrix $\hat{\sigma}_n$ and rewrite Eq. 3.31 as the following simplified form

$$\begin{aligned}e^{i|\hat{N}|\hat{\sigma}_n\Delta t} &= e^{i\theta\hat{\sigma}_n}\\ &= \cos(\theta)\hat{\mathbb{1}} + i\sin(\theta)\hat{\sigma}_n\end{aligned} \tag{3.33}$$

By introducing a dimensionless $\theta = |\hat{N}|\Delta t$, and with $\frac{\hat{N}}{|\hat{N}|} = -i\frac{\rho'}{|\rho'|}$, $\frac{\hat{N}^*}{|\hat{N}|} = i\frac{\rho'^*}{|\rho'|}$:

$$e^{i|\hat{N}|\hat{\sigma}_n\Delta t} = \begin{bmatrix}\cos(\theta) & -i\sin(\theta)\frac{\rho'}{|\rho'|}\\ -i\sin(\theta)\frac{\rho'^*}{|\rho'|} & \cos(\theta)\end{bmatrix} \tag{3.34}$$

Plugging the simplified form of the propagation operator, Eq. 3.30, and the nonlinearity operator, Eq. 3.34 into Eq. 3.29, we arrive at a simple equation to propagate electric field amplitude after a small time step Δt,

$$\begin{pmatrix} \mathcal{E}_1(t+\Delta t, z) \\ \mathcal{E}_2(t+\Delta t, z) \end{pmatrix} = \begin{bmatrix} \cos(\theta) & -i\sin(\theta)\frac{\rho'}{|\rho'|} \\ -i\sin(\theta)\frac{\rho'^*}{|\rho'|} & \cos(\theta) \end{bmatrix} \cdot \begin{pmatrix} \mathcal{E}_1(t, z-c/n\Delta t) \\ \mathcal{E}_2(t, z+c/n\Delta t) \end{pmatrix} \quad (3.35)$$

3.2.4 Simulation in Matlab

The simulation of SBS compression is realized in the Matlab environment. As described in Eqn. 3.35, the simulation is to calculate the fields evolution in whole space at every small time intervals Δt. The Matlab code consists of one main .m file and 5 function .m files (REFERENCE APPENDIX).

The "SBSmain.m" is the main .m file for simulating conventional single-cell SBS compression. It defines all the physical constants, the initial conditions (pulse width, pulse energy, beam size, focal length of the lens, etc.), the time step, the temporal space, spatial space, index and gain space(i.e. define the SBS gain medium dimension), and call the other 5 functions to complete the simulation.

The "gfunc.m" is a function .m file which calculates the transient gain describe in Eq. 3.22.

The "MakePhonon.m" is a function .m file that calculates the phonon wave (density wave) in Eq. 3.19. The convolution is done by calculating the following sum

$$\rho'(t,z) = \sum_{\tau=t}^{t-N\Delta t} \frac{1}{8\sqrt{2\pi}} g(t-\tau)\mathcal{E}_1(\tau)\mathcal{E}_2^*(\tau)\Delta t \quad (3.36)$$

starting from the current time $\tau = t$ back to some past time $\tau = t - N\Delta t$. The physical meaning of the convolution is that the memory of the system affects the present value of the phonon wave. As shown in Eq. 3.22, the transient gain still exists after the optical filed leaves and decays with a characteristic time $2/\Gamma_B$. So

as long as the integer N is chosen such that $N\Delta t > 2/\Gamma_B$, i.e., the history of the system being considered is longer than the memory of it, the sum in Eq. 3.36 is a good approximation of the convolution (Eq. 3.19).

The "Propagate.m" function calculates the effect of the propagation operator on the pump and Stokes field amplitude after time Δt. As shown in Eq. 3.30, the field shifts by $c/n\Delta t$ in space after time Δt. The space step is chosen as $\Delta z = c/n\Delta t$ so that the filed in space shifts by one step after Δt:

$$\mathcal{E}_{1\text{shift}}[2:\text{end}]] = \mathcal{E}_1[1:\text{end-1}]$$
$$\mathcal{E}_{1\text{shift}}[1] = \text{complex}(0,0)$$

For propagating the Stokes filed $\mathcal{E}_2$, the procedure is similar but with an opposite direction.

The "Nonlinearity.m" function calculates the nonlinearity operator matrix of Eq. 3.34.

The "genCorrection.m" function corrects the field after the propagator "shift" in space by considering the geometric effect. It is necessary because the beam size at different locations in space is different when a lens is used to focus the beam in the SBS medium. The correction factor is only z dependent as long as the beam size and focusing condition is known.

For our generator-amplifier setup, the "SBS2PulseInteraction.m" is used as the main .m file and a function "seedGeneration.m" is called to generate a seed pulse as the initial Stokes pulse (instead of using random noise with normal distribution).

3.3 SBS Pulse compression with a single-cell and cascaded two-cell setup

3.3.1 Experimental setups

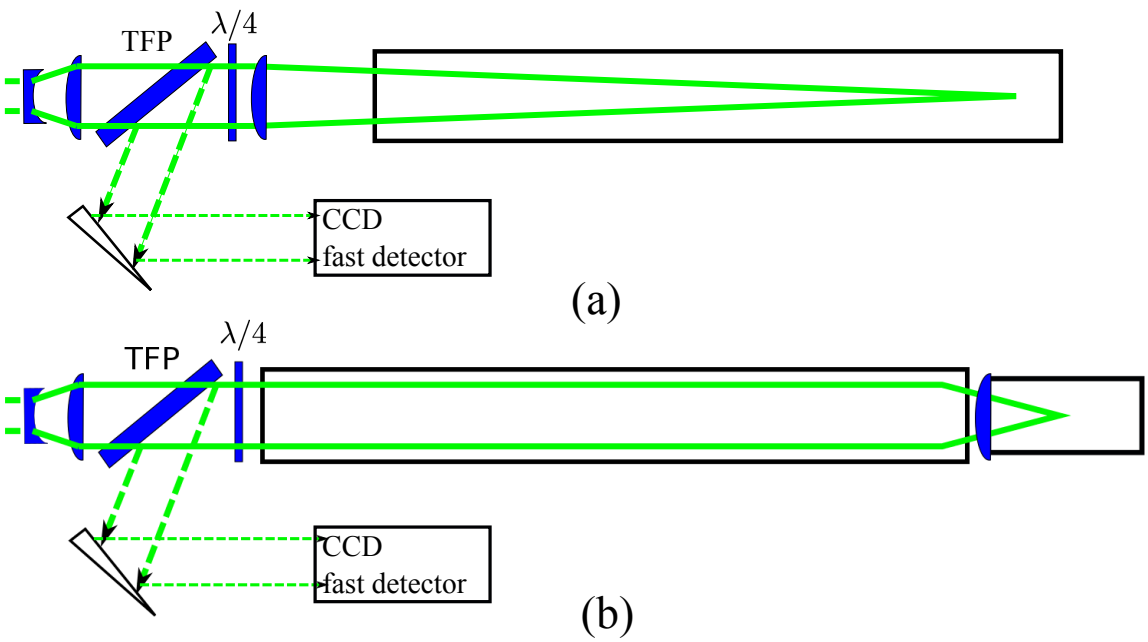

Figure 3.2: SBS compression setup: (a) Single cell setup; (b) Cascaded two-cell setup. TFP: thin film polarizing beam splitter. $\lambda/4$: quarter-wave plate.

The single-cell and cascade two-cell setups are commonly used optical configurations when working with SBS compression and SBS phase conjugation, because they are simple to implement and very effective. The initial design of the SBS compressor for this project was a single-cell setup with liquid FC-72 as the SBS medium, as sketched in Fig. 3.2(a). The focusing distance inside the SBS cell is designed to match half of the spatial pulse length at its half maximum for effective compression. The combination of a polarizer and a quarter-wave plate separates the pump and the Stokes beams.

The cascade two-cell setup, sketched in Fig. 3.2(b), consists of one generator cell and one amplifier cell. The beam is collimated inside the amplifier cell to allow more energy in the medium without triggering other nonlinear effect such as stimulated Raman scattering. The beam is then focused into the generator cell with a short focusing lens, in order to initial the SBS reflection in the very leading edge of the pump pulse, without triggering optical breakdown around the focus. An attenuator can be inserted in between the two cells to further limit the pump energy entering the generator cell to avoid optical break down.

3.3.2 Experimental results with single cell setup

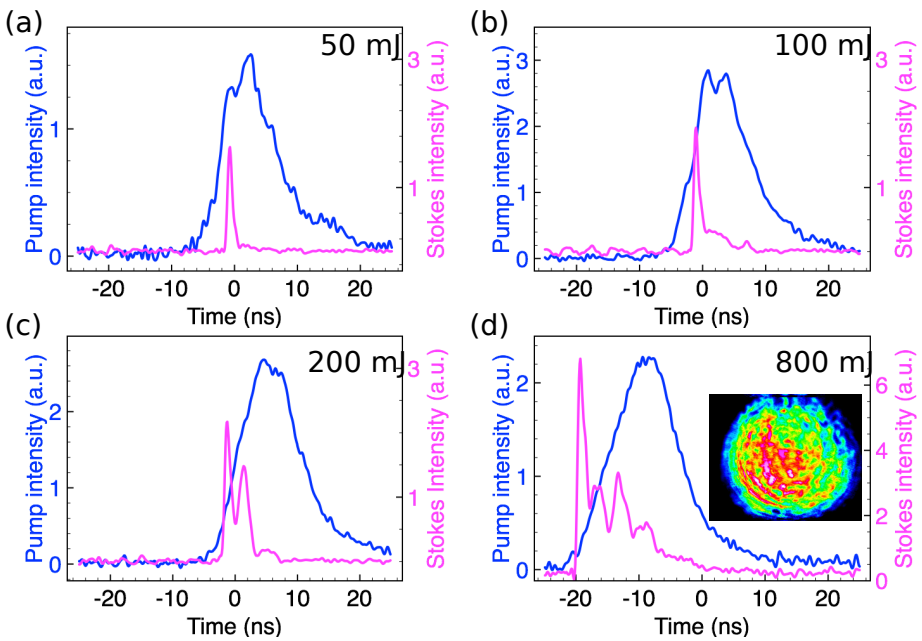

Figure 3.3: Compression results with a single cell setup at 532 nm using FC-72 as the SBS medium. Blue: pump pulse shape; red: Stokes pulse shape.

Fig. 3.3 summaries the compression results with a single cell setup at 532 nm using liquid FC-72 as the SBS medium. Here, the cell length is L = 130 cm and the focal length inside the liquid is 120 cm, matching half of the spatial pulse length:

$c\tau_p/n \times \frac{1}{2} \approx 140$ cm (pulse width τ_p=12 ns and index of refraction of the liquid is n = 1.25). The Stokes pulse was compressed down to $\sim$ 1 ns with a pump pulse of 50 mJ. As we increased the pump pulse energy (from panel a to d), the Stokes featured a short leading pulse with multiple subsequent pulses. In the end, the peak power amplification was limited because at higher pulse energies, an increasing portion of the pulse energy was distributed in the secondary structures, instead of being confined to a single peak.

We think this is due to the relatively short interaction length ($\sim$ focal distance inside the SBS medium) compared to the actual interacting pulse length. As the pump energy increases, the SBS initiates earlier into the leading edge of the pump pulse, also shown in the relative timing the Stokes pulses in Fig. 3.3, making the actual interacting pulse longer than its FWHM. As the leading edge of the Stokes exits the cell, there is still a significant portion of the pump that continues entering the cell, reaching the focal area and generating a second Stokes pulse.

On the other hand, as we increased the pump energy, we observed more distortion and modulation on the spatial intensity profile of the Stokes beam, shown in inset of Fig. 3.3(d). This might be due to the on-set of other nonlinear effects such as stimulated Raman scattering.

We then increased the cell length to 250 cm and the focal length to 230 cm ($\sim$FWHM of the spatial pulse length) inside the liquid. Fig. 3.4 shows the results of using a 250 cm long cell and input pulse at 1064 nm. With an input pulse of 12 ns, 330 mJ, the Stokes pule was successfully compressed to a single pulse of 404 ps with 79% conversion efficiency, as shown in Fig. 3.4(a). The compression ratio is about 30X and the Stokes pulse width is below the phonon lifetime ($\sim$1 ns [36]) of FC-72. However, as we sent more energy into the SBS cell, the Stokes pulse shape became fluctuating, shown in Fig. 3.4(b), and the beam profile became distorted as well. We think this was the result of the on set of competing nonlinear effects due

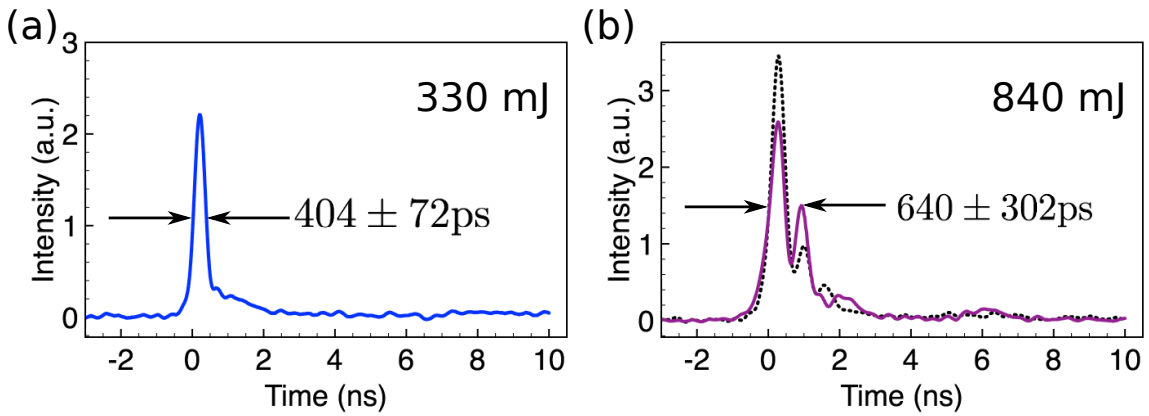

Figure 3.4: Compression results with a single cell setup at 1064 nm using FC-72 as the SBS medium. Cell length: L=250 cm; focal length: f=230 cm; input beam diameter ϕ=20mm.

to high intensity in the focusing geometry.

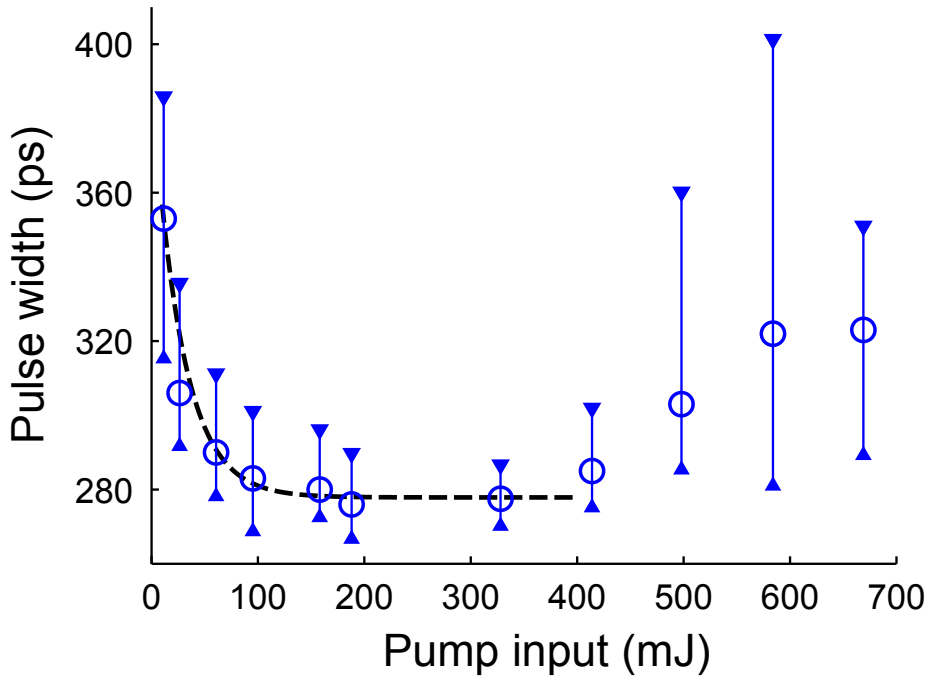

Figure 3.5: Compression results with a single cell setup at 532 nm using water as the SBS medium.Cell length: L=250 cm; focal length: f=230 cm; input beam diameter ϕ=30mm.

The same experimental configuration was applied to 532 nm pulses using water

as the SBS medium and similar energy limitation was observed. In Fig. 3.5, we plot the Stokes pulse width versus the input pump energies. The error bars represent the maximum and minimum pulse width that we observed over 80 shots. The compression was very stable at input energies between 150 mJ and 350 mJ and the compressed pulse width saturated to the phonon lifetime of water ($\approx$ 300 ps [50]). However, as the pump energy increased further (e.g. $>$ 400 mJ), the compression became unstable. At input energy of 498 mJ, noticeable stimulated Raman signal of water at 649.5 nm was observed. Strong stimulated Raman was observed in every shot when the input energy increased to 680 mJ.

3.3.3 Experimental results with cascaded two-cell setup

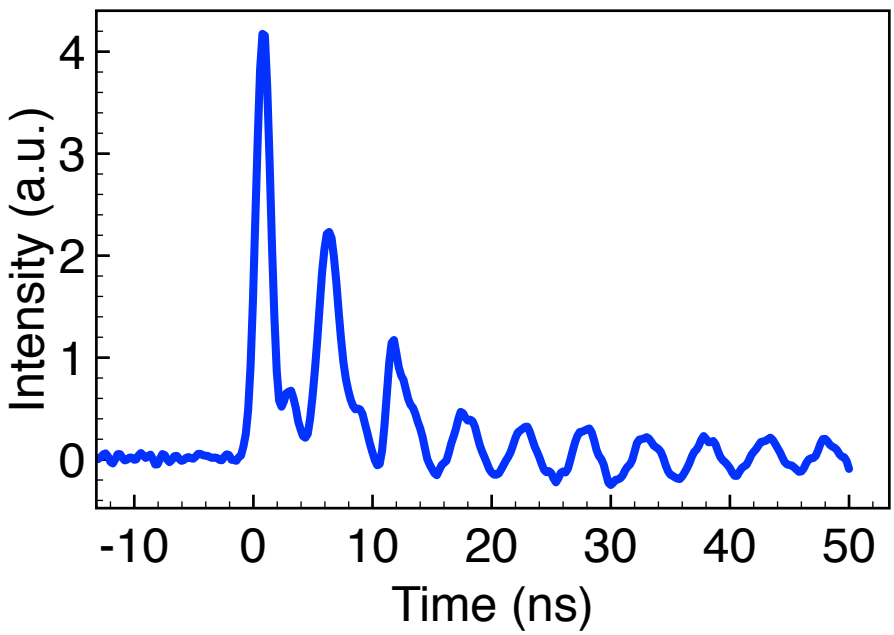

Figure 3.6: Compression results with a cascaded two-cell setup at 1064 nm using FC-72 as the SBS medium. Amplifier cell length: L=250 cm; focal length in generator cell: f=18.8 cm; input beam diameter ϕ=20mm.

The cascaded two-cell arrangement was also tried with 1064 nm pulses and liquid

FC-72 as the SBS medium. With an input energy of 660 mJ, we observed stable reflectivity of 83% and no beam distortion. However, instead of a single compressed pulse, the reflected Stokes featured a multiple-pulse train with decaying amplitude, shown in Fig. 3.6. Consequently, similar to the single-cell configuration, the maximum peak power in the Stokes pulse was severely compromised.

3.3.4 Conclusion

We demonstrated SBS pulse compression at 1064 nm and 532 nm with liquid FC-72 and water as the SBS medium in two different configurations. We found that both the single-cell and cascaded two-cell setup allow effective pulse compression for energies up to several hundreds of mJ. In our hands, the interaction length needs to be at least the FWHM of the spatial pulse length of the pump, instead of half the FWHM as commonly used in the literature, for a complete compression at high energy input. In this way, the Stokes pulse can be compressed to close to the phonon lifetime limit of the SBS medium with $\sim 80\%$ conversion efficiency.

However, we found that the energy capacity of both setups is limited to only several hundreds of mJ due to competing nonlinear effects as well as the presence of multiple pulses in the Stokes's temporal profile. These severe limitations make both configurations unsuitable for our high energy (> 1J) application.

3.4 Optimizing SBS Pulse compression with a generator-amplifier setup

In this section, we show results of SBS compression using a different optical configuration: the generator-amplifier setup (or the parallel two-cell setup). We explore

the limit of SBS pulse compression in liquid for high energy applications using this configuration. Towards this end, we use a combination of theoretical modeling, computer simulation and experiments to elucidate the critical parameters in the SBS generation process and show how optimizing these parameters leads to ∼40X pulse compression down to ∼300 ps with >1 J of energy after compression and a shot-to-shot variation of the pulse width of ∼2%. To our knowledge, this represents the highest peak power at 532 nm obtained using SBS technique with unprecedented shot-to-shot reproducibility.

3.4.1 Motivation and basic principles of the generator-amplifier setup

Although simple in implementation, for stable high energy application, the SBS pulse compression by singe cell or cascaded two cell is strongly limited for stable high energy application by its low energy capacity and instability due to thermal disturbance [35] (see Section 3.3.2 and 3.3.3). Of all the SBS compression geometries, the parallel two cell setup [44] has demonstrated the largest energy capacity. The idea of this setup is to first generate a Stokes seed pulse with small energy in a single long focusing configuration, then amplify the Stokes seed pulse in a amplifier cell where the beams are collimated. The energy in the focusing generator cell can be controlled to the minimum value needed for efficient energy extraction of the pump, without exceeding the energy limit and with no further attenuation. The energy in the amplifier cell can be scaled up by increasing the beam size while keeping the intensity under the SBS threshold (empirically, the intensity-gain-length parameter should be $IgL < 30$). In this way, the energy capacity can be greatly increased, limited only by the size of the optics and the homogeneity of the SBS medium. Moreover, the energy density can be even higher by choosing a SBS medium with smaller gain.

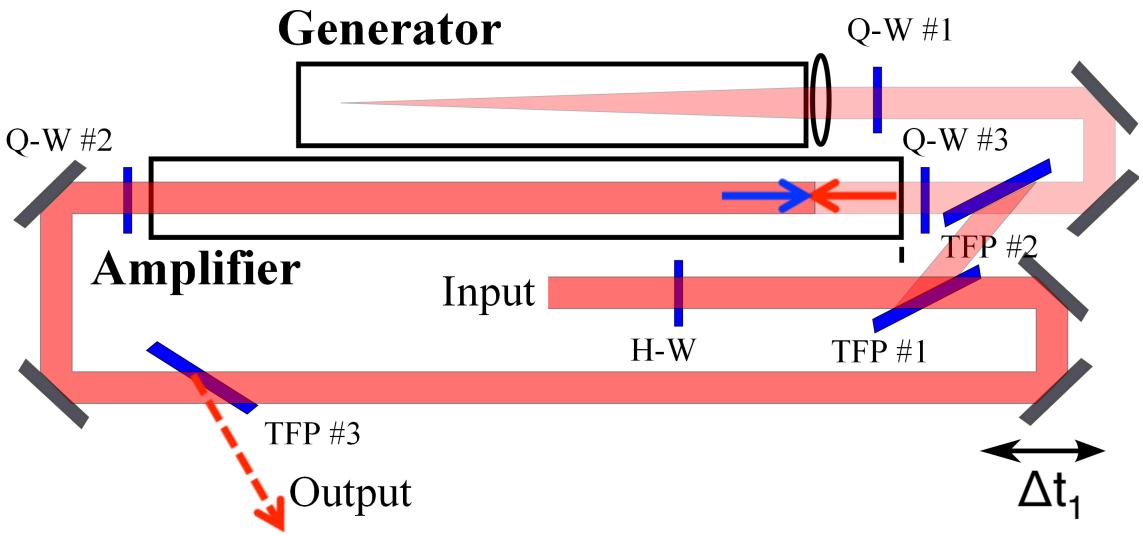

Figure 3.7: Layout of the amplifier-generator SBS setup. Q-W: quarter waveplate, TFP: thin film polarizer, H-W: half waveplate, Δt_1: optical path length delay. Dark red: pump beam, light red: seed beam. Arrows: propagation directions.

The experimental arrangement used is sketched in Fig. 3.7. The input is from a custom-built single mode Q-switched Nd:YAG oscillator and 6-stage single-pass amplifiers system operating at 1.25 Hz. A novel real-time resonance tracking method [51] is implemented to ensure that every single shot from the injection seeded Q-switched oscillator is single mode with a smooth temporal profile. The system output pulses of 12 ns at FWHM, 5 J at 1064 nm and 3.5 J at 532 nm (doubling with a LBO SHG crystal). A small portion of the laser is extracted by the combination of a half-wave plate and a thin film plate polarizing beam splitter (TFP #1). The split output is directed into a generator cell by TFP #2 and two directing mirrors. The largest fraction of the source is sent into the Brillouin amplifier cell entering from the left side in Fig. 3.7 and interacts with the Stokes seed pulse entering from the opposite side. The quarter-wave plate Q-W #1 is used to ensure that the Stokes seed pulse is reflected from the generator with its polarization angle rotated by 90^o and transmitted through TFP #2 into the amplifier. Two quarter-wave plates Q-W #2 and

Q-W #3 are oriented with their fast axis aligned such that the depleted pump can be reflected by TFP #2 without entering the generator and the amplified Stokes can be extracted by TFP #3. The energy scaling is realized by a beam-size controlling telescope before the half-wave plate. As will be detailed in the following discussion, the meeting point of the pump and Stokes seed pulse, indicated by the solid blue and red arrows, the intensity of pump and seed pulse, the interaction length inside the amplifier and finally the thermal stability can be optimized to achieve efficient and stable pulse compression. We measured the 1064 nm pulse by a 12.5 GHz GaAs biased photodetector from Newport and the 532 nm pulse by a Hamamatsu R1328U-52 biplanar phototube (rise time: 60 ps; spectral response: 185-650 nm; detection area: 10 mm diameter) combined with an Agilent DSO90254A digital oscilloscope (Bandwidth: 2.5 GHz; Sampling rate: 20 Gsa/s). As it was reported the compressed pulse width is intensity dependent across the beam area [41], only center regions of the beam sampled are shown below.

3.4.2 Experimental parameters optimization

Optimizing the relative delay between pump and seed pulse

Since the pump and Stokes seed pulse are counter-propagating, overlapping of them in time is critical for efficient energy exchange. The amplifier cell needs to be positioned correctly with respect to the crossing point between pump and seed. Fig. 3.8 illustrates three simulated situations in which the leading edge of the pump and Stokes seed meet at different locations relative to the SBS cell. In all three panels, the vertical axis on the right (blue) represents the pump intensity, the vertical axis on the left (red) represents the Stokes intensity, both in arbitrary unit. The horizontal axis represents the spatial dimension. The SBS medium is 2.5 m long and is located in space from 0 to 2.5 m. The solid red pulses are the amplified Stokes while the

dotted blue pulses are the input pump and the solid blue with shaded area are the depleted pump. The arrows point to the propagation directions. The rectangle with a blue and red arrow pointing at opposite directions in the inset indicate the SBS medium relative to the meeting point of the pump and Stokes seed. When the two

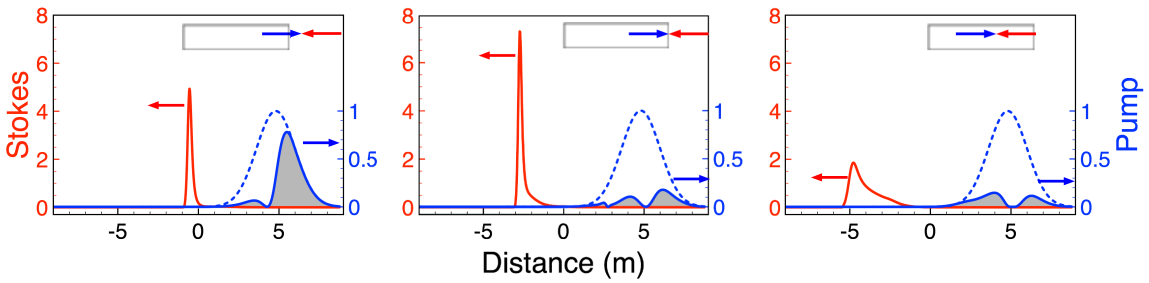

Figure 3.8: Optimizing the delay between the pump and seed pulse is critical for optimal SBS compression. Simulated compression result as the pump and seed pulse meeting location (top right schematic) is varied with respect to the SBS medium. Solid red: amplified Stokes; dashed blue: input pump;solid blue with shaded area: depleted pump.

pulses meet outside the right entrance of the SBS amplifier cell, as shown in the left panel of Fig. 3.8, the Stokes pulse interact with only a portion of the pump pulse, leaving a large amount of energy un-depleted (shaded area). The overall result is a low pump energy extraction efficiency and therefore a small peak power amplification. As shown in Fig. 3.8 middle panel, meeting at the right entrance of the cell ensures persistent interaction with the SBS medium throughout the spatial-temporal overlap of the pump and Stokes pulses, leading to an efficient energy exchange and high peak power amplification. If they meet inside the cell as indicated in the right panel, although the Stokes still extracts most of the energy from the pump, the energy goes to its trailing edge instead of its leading edge as the leading edge exit the cell. This leads to a low peak power amplification and compression ratio due to the short interaction length. In conclusion, there is an optimal delay Δt between the pump and the Stokes pulse for best compression performance.

Other than the optical path length difference Δt_1 shown in the setup Fig. 3.7(b),

we found that the extra delay during the Stokes seed generation process Δt_2 should also be taken into account:

$$\Delta t = \Delta t_1 + \Delta t_2 \tag{3.37}$$

To visualize the effect of Δt_2 which is coupled into the seed energy, we use an input pulse of 16 ns and a fixed optical path length delay. We measured the amplified Stokes(red)and the depleted pump(blue with shade area) as shown in Fig. 3.9. As the seed energy increases, the energy transfer between the pump and Stokes starts earlier. However, the peak power of the Stokes increases and then decrease, with more energy distributing in its "tail". This counter-intuitive result was also shown in the result of reference [44] but with no explicit explanation.

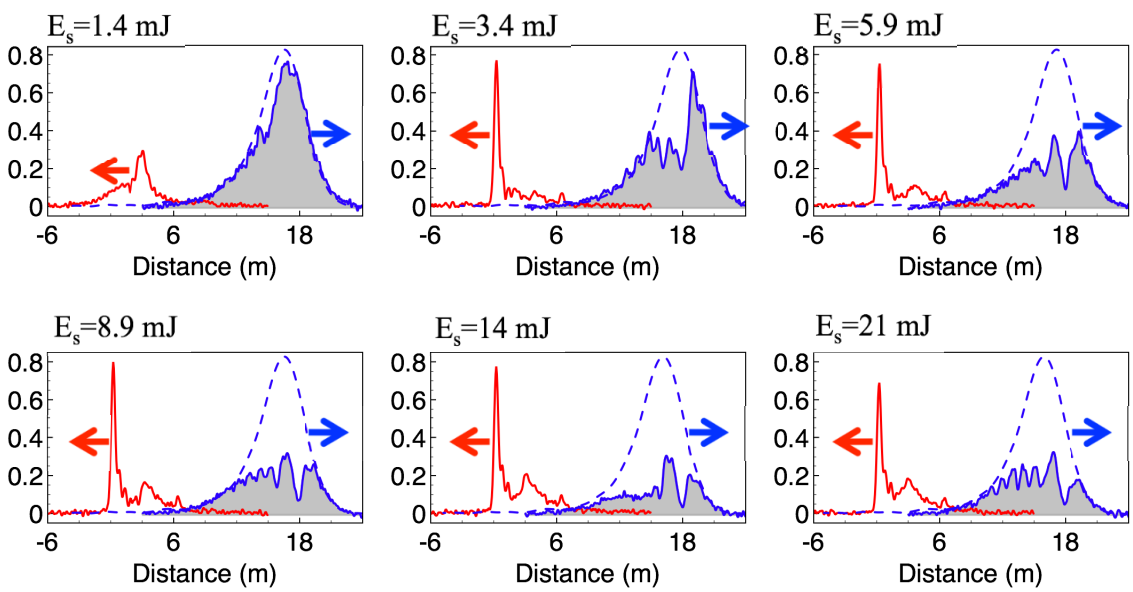

Figure 3.9: Solid red: amplified Stokes; dashed blue: input pump;solid blue with shaded area: depleted pump

The energy dependent Δt_2 is due to the threshold property of stimulated Brillouin scattering: the stimulated process initiates only when the intensity at the focus

reaches its threshold. Therefore, the SBS starts at the peak of the pulse at low input energy and advances to the leading edge as the input energy increases. Fig. 3.10(a) is

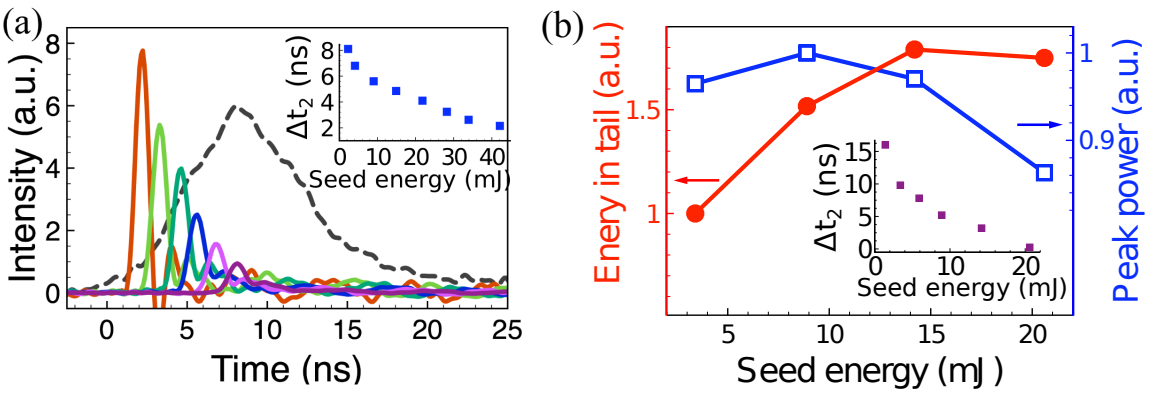

Figure 3.10: (a) Direct experimental measurement of the extra delay (Δt_2) during seed pulse generation at different seed energies. Colored curves: seed pulse shapes with energy from 3.4 mJ to 45 mJ. Inset: quantified Δt_2 versus seed energy. (b) Peak power (blue axis) and "tail" energy (red axis) of the amplified Stokes pulse as a function of seed pulse energy. Inset: Δt_2 as a function of seed energy, a 16 ns seed was used in this experiment.

a direct experimental measurement of Δt_2. The black dashed line is the input pulse shape and the colored solid lines are reflected Stokes pulses with different input energies. The arrival time difference of the Stokes with different energy is as long as the FWHM of the input pulse,which is several nano seconds, as plotted in the inset of Fig. 3.10(a). Fig. 3.10(b) shows the quantified results in Fig. 3.9: the peak power of the amplified Stokes and the energy in its "tail" as function of the Stokes seed energy. The mapping of seed energy to Δt_2 is plotted in the inset. As the seed energy increases, the peak power of the amplified Stokes increases and then decreases with more energy distributed in the trailing edge.

With both Δt_1 and Δt_2 taken into account, an optimal delay can be found by using a fixed Stokes seed energy and adjust Δt_1 to make sure the pump and Stokes seed meet at the right side of the cell's entrance for maximum power amplification.

Optimizing pulse intensity for best energy extraction

As a $\chi^{(3)}$ nonlinear process [49], the higher the intensity, the more efficient the SBS interaction inside the amplifier. However, the intensity of the pump should not be too high to initiate SBS back reflection by the pump itself.

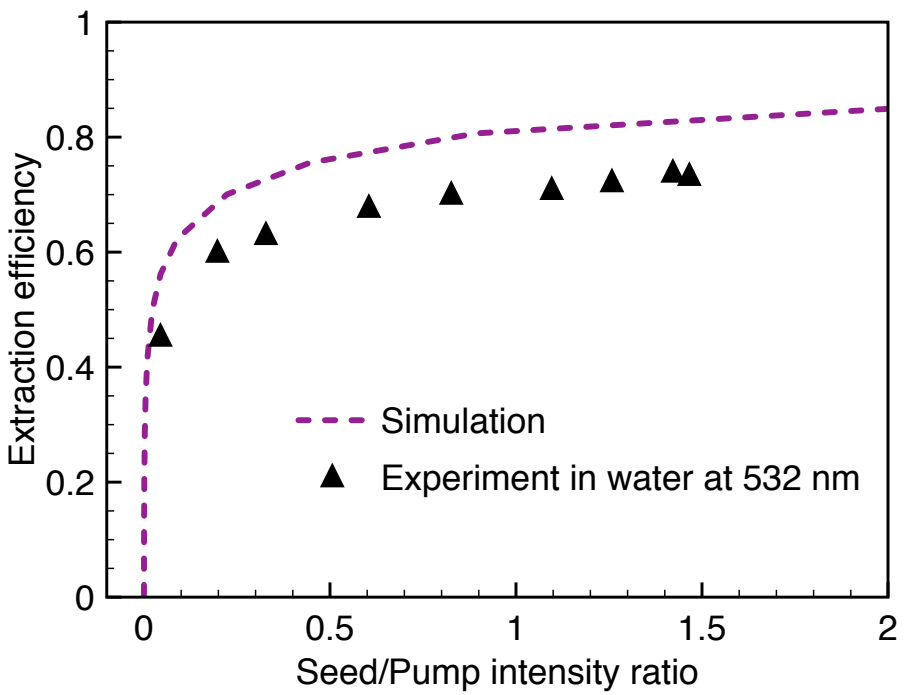

Figure 3.11: Optimizing seed intensity for best pump energy extraction. Magenta: simulated relation between extraction efficiency versus seed/pump intensity ratio; solid black triangles: experiment in water at 532 nm.

The empirical intensity-gain-length parameter for the SBS threshold is $IgL = 30$. In the experiment, this empirical number is very well matched by simply adjusting the beam size until the reflected signal is just about to grow exponentially.

In order to search for an optimum Stokes seed intensity to achieve efficient energy extraction from the pump, we carried out both simulation and experiment in water at 532 nm. In both ways the pump intensity is at threshold intensity for SBS in

the amplifier cell. In the experiment, to avoid time-energy coupling as discussed in section 3.4.2, we send a fixed input energy of 120 mJ into the SBS generator (220 cm focusing distance into water used here as SBS medium), creating a compressed Stokes seed of 87 mJ and 325 ps at its FWHM. The actual Stokes seed energy that enters the amplifier cell is adjusted by an extra half-wave plate and a thin film polarizing beam splitter in between Q-W #3 and TFP #2. The results are plotted in Fig. 3.11. The extraction efficiency increases quickly as the seed intensity increases and saturates to a maximum value when the seed intensity is comparable to the pump. Our measurement in water shows the similar trend (full triangle in Fig. 3.11). The smaller measured SBS extraction efficiency (as compared to the simulation) is due to the smaller intensity at the beam edge. In simulation a ideal flat top beam is used.

In summary a Stokes seed with the same peak power as the pump is desired to effectively extract energy from the pump. The energy of the seed needed is relatively small if a long focusing generator is used to get a highly compressed seed pulse. In our experiment in water, with a compression ratio of 37 in the generator, a seed with less than 3% of the pump energy is enough for optimum energy extraction.

Optimizing the interaction length

The interaction length is the length of the amplifier cell, provided the delay between pump and Stokes has been optimized. As it is shown in Fig. 3.8, a short interaction length gives rise to incomplete compression with a long tail in the Stokes pulse. However, long interaction length brings in loss due to absorption and makes the system inefficient as well as bulky. Our goal is to find an amplifier cell length that is at the saturation point for power amplification,which represent the optimum combination of compression ratio and efficiency. In Fig. 3.12, the power amplification is plotted as a function of relative delay, Δt between pump and Stokes at different amplifier

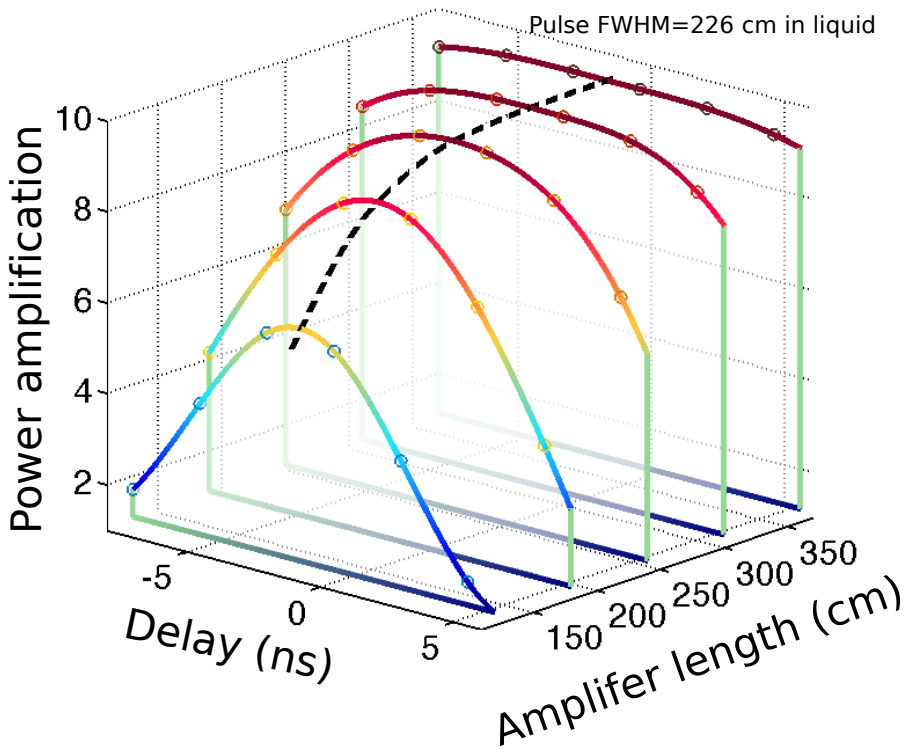

Figure 3.12: Searching for optimum amplifier length for best power amplification. Color lines: simulated power amplification ratio versus delay (Δt) at amplifier lengths of, from front to back: 120 cm, 180 cm, 240 cm, 300 cm and 360 cm. Black dashed line: power amplification ratio at optimum delay as a function of amplifier length. The zero delay refers to the peak of the Gaussian pump reaching the left entrance window when the seed enters the cell from the right.

lengths. The black dashed line tracks the peaks of power amplification curves. The colored curves are a quantitative representation of the effect of delay, which were shown in Fig. 3.8. As the amplifier length increases, the output peak power becomes less sensitive to the delay and the peak of it also saturates to a maximum value. One can imagine that, for an infinitely long cell, the pump and Stokes can always overlap in the medium and the delay is negligible. The peak power amplification reaches a saturation point when the amplifier length is more than 250 cm ($\approx$ FWHM of the spatial pulse length). This is the length we used in our experiments.

Minimizing thermal disturbance

Thermally induced motion in the SBS medium strongly limits the stability of the compressed Stokes seed pulse generation. The same limitation applies for the long focusing single cell setup and the cascade two cell setup [35, 38]. As for the amplifier cell in the parallel two-cell setup, thermal fluctuation induces inhomogeneity of the medium due to thermal-optical effect, which introduces aberrations to the Stokes wavefront. This effect is extremely significant in the FC-72 liquid, the temperature dependent refractive index of which is six times higher than water (-4.7$\times 10^{-4}$/K compared to -0.8$\times 10^{-4}$/K). After propagating through the 2.5 m long liquid cell with no thermal control, a round beam becomes elliptical with its major axis parallel to the optical table and also deflects downwards in the vertical direction. The thermal effect can be modeled by ABCD propagation of Gaussian beam in lens-like medium[52]. As the temperature of the environment around the cylindrical cell increases, an positive index gradient from the center to the side of the cylinder develops because of the negative dn/dt, making the liquid cell act like a positive lens. At the presence of gravity, "hot" medium rises to the top while "cool" medium stays at the bottom, leading to a vertical index gradient. The overall effect of temperature variation and gravity gives rise to an asymmetric lens with shorter focal length in the vertical direction, which makes a round beam elliptical and bending downward.

To quantify the thermal effect and evaluate thermal isolation performance, we sent a beam of 2.5 mm in diameter through the 2.5 m long liquid cell and measured the beam deflection angle. We compared the results on cells filled with liquid FC-72 and water with different thermal isolation methods in laboratory with active temperature controlled to within 2^{o}C.

The result plotted with solid triangle in Fig. 3.13 shows the performance of a FC-72 cell with one-layered styrofoam housing (made of 1" thick styrofoam with windows

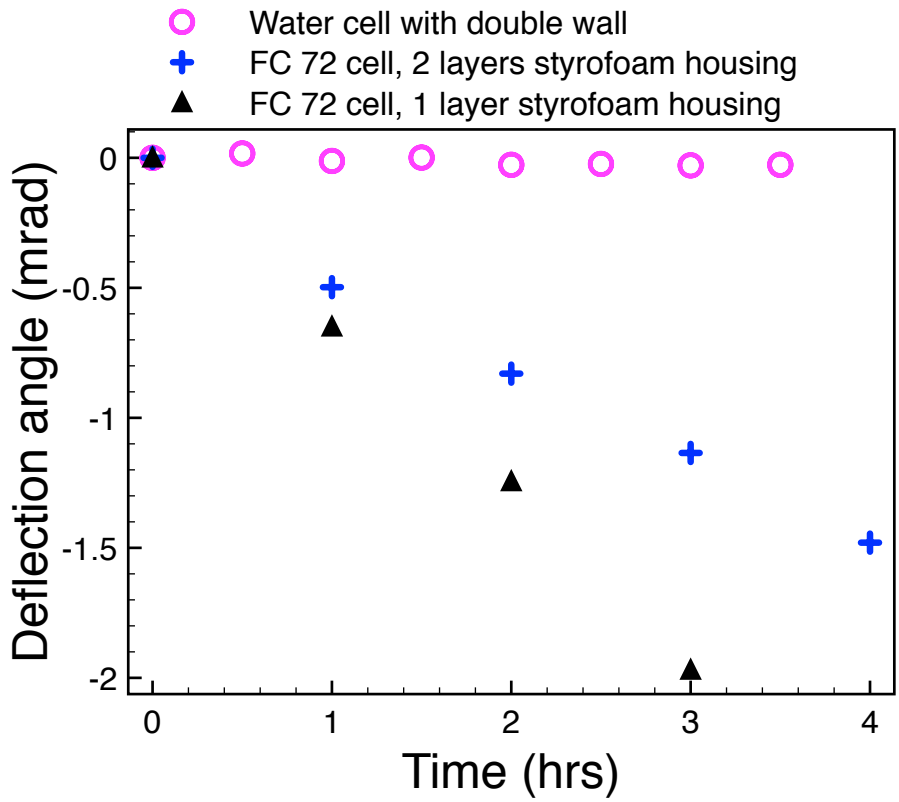

Figure 3.13: Minimizing thermal disturbance for long-term stability. Beam deflection angle versus experimental time in hours under different test conditions.

at the entrance and exit. 1" air gap in between the styrofoam and the glass cell is designed to have air as extra layer of thermal insulation but with a minimum of air convection.) The deflection angle changes by 2 mrad after three hours, corresponding to an index difference of 5.3×10^{-4} between the center of the 48 mm diameter cell to the bottom of it. This is good enough for stable compression within 3 hours. An extra layer of styrofoam housing slows down the thermal effect on the FC-72 cell, shown in blue cross in Fig. 3.13. Without any thermal control, the beam deflects quickly by 2 mrad within half an hour in the lab (data not shown), and the SBS compression is very unstable even at low input energy of several tens of mJ.

A significant improvement was achieved when water was filled in a special design

double-walled glass cell, shown in empty circles in Fig. 3.13. The inner tube of the double-walled glass cell is filled with pure water as the SBS medium. The space in-between two walls is filled with circulating water allowing active temperature stabilization. The combination of water and the double-walled cell successfully controls the beam deflection angle to be below 30 μrad for hours. This is almost two orders of magnitude smaller than the result in a FC-72 cell. We also expanded the beam to 32 mm and monitored the far field pattern of it after propagation through the water cell. No significant aberration was observed on the beam wave front.

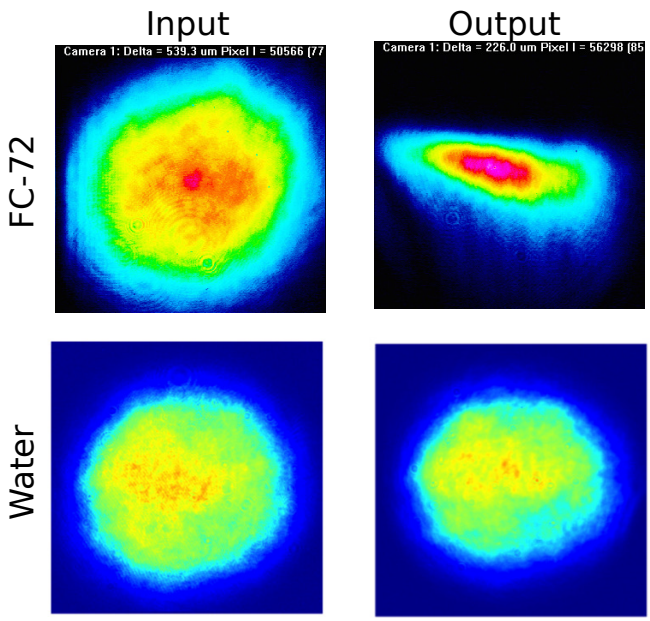

Figure 3.14: Beam distortion measurement with liquid FC-72 and water. Left panels: input beam profiles; Right panels: output profiles after propagating through the 2.5 m long liquid cell and about 7 m of air. Upper panels: measurements with liquid FC-72; Lower panels: measurements with water. Both at room temperature.

The enclosed styrofoam housing with windows and air gap provides good thermal isolation for the FC-72 liquid cell and ensures stable pulse compression. However, we still noticed distortion on the Stokes beam caused by the amplifier cell from ambient temperature fluctuations, see Fig. 3.14. Beam distortion measurements were taken

with both liquid FC-72 and water. The left panels are the initial beam profiles and the right panels are the beam profile after propagating through the 2.5 m long liquid cell and 7 m of air. The upper panels shows the results of liquid FC-72 and the lower panels shows the results of water. Both measurements were taken at room temperature. Asymmetric focusing effect from the FC-72 cell is clearly seen while water shows no significant distortion on the beam. If a beam with high far field quality is critical, SBS medium with small temperature dependent refractive index such as water is desired. Engineered thermal isolation housing such as the double-walled glass cell also minimizes the thermal disturbance inside the medium and therefore minimizes aberrations on the Stokes beam.

Pulse compression results in FC72

As we optimized the energy scalable two-cell setup discussed in section 3.4.2, stable, efficient high energy SBS compression is achieved. A representative pulse of the amplified Stokes is plotted in Fig. 3.15a. At 1064 nm, the final output is compressed down from a 1J, ∼12 ns pump (inset, blue dotted line) to a FWHM width of ∼580 ps. Note that this value is below the phonon lifetime of FC-72 (∼ 1 ns [36]). The overall energy reflectivity in this case was 73.5%. We have thus achieved a peak power of ∼1 GW which represents a factor of 11 enhancement compared to pre-SBS compression. To quantify the stability of the setup, we measured the shot-to-shot fluctuation in pulse width to be below 2 % and shot-to-shot energy fluctuation to be below 1.3 %

Also clearly visible in the experimental pulse shapes shown in Fig. 3.15a is signal resurgence at ∼ 2 ns. We understand this interesting phenomenon as energy exchange between the pump and Stokes under the condition of transient SBS compression [46]. As the leading edge of the Stokes pulse gets amplified, it depletes the pump quickly (panel a, depleted pump between -5 to 3 ns). The tail of the Stokes

pulse continues to interact with the phonon field and transfer its energy back into a "regenerated" pump, as indicated by the peak near 5 ns in the depleted pump trace (panel a inset). This Stokes-to-pump back transfer sharpens the falling edge of the Stokes pulse, resulting in a highly compressed pulse shape. As the Stokes is compressed down to below the phonon lifetime of the SBS medium and its tail gets depleted, pump-to-Stokes transfer resumed domination, giving rise to a weak secondary pulse in the amplified Stokes after its main peak. This process continues as they propagate across each other, therefore creates a Stokes pulse with modulated tail. In panels (b) of Fig. 3.15, we show the calculated pulse shapes of the amplified Stokes. Our theoretical modeling successfully reproduced the relative pulse width in the two cases as well as the position and relative amplitudes of the secondary pulse when compressing in the FC-72. The second pulse contains $\sim 25\%$ of the pulse energy and presents a limit to the peak power enhancement. It can be avoid by choosing a medium with short phonon lifetime (wavelength dependent) or compressing the Stokes to be above the phonon lifetime.

Pulse compression in water

One drawback of liquid fluorocarbon is its high sensitivity to thermal fluctuations (due to its high temperature dependent refractive index, $\partial n/\partial T \sim -4 * 10^{-4} K^{-1}$ at $25^o C$), which gives rise to unstable compression. Although a better thermal isolation scheme help alleviate the problem (Fig. 3.13), the less favorable thermo-optical property of liquid fluorocarbon ultimately limits its application in high energy SBS compression. Other than liquid fluorocarbon, water has also been explored in SBS applications [40, 41]. Water shares many of the favorable properties of liquid fluorocarbon for SBS pulse compression applications, such as short phonon lifetime, high SBS gain and chemical stability. It is also cheaply and widely available, even at the highest purity. Moreover, water has a much smaller thermal-optical coefficient,

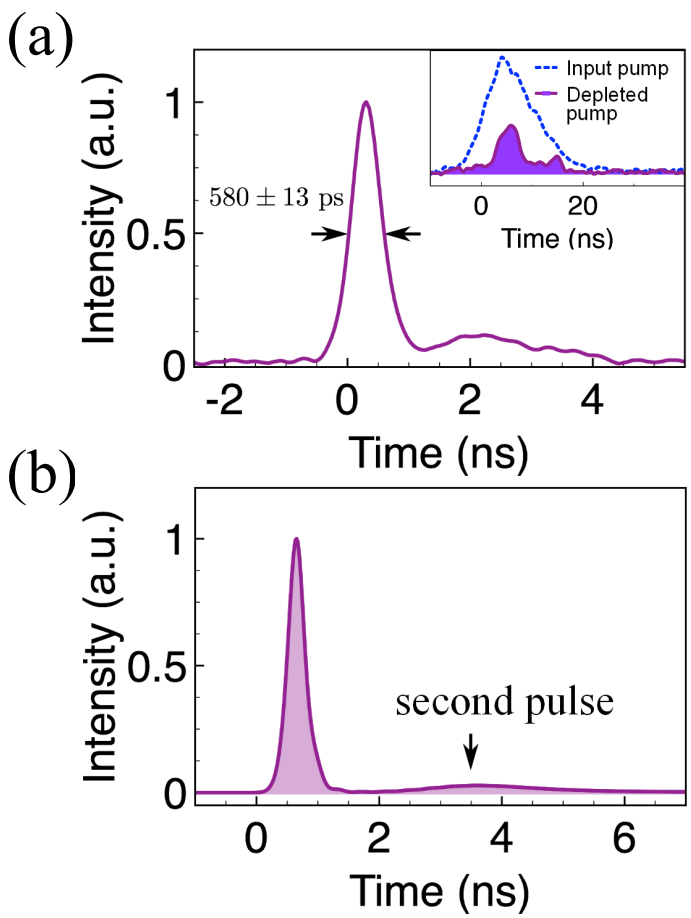

Figure 3.15: (a) Experimental output pulse shapes using FC-72 as the SBS medium at 1064 nm. Inset: pulse shape of the pump before (dotted blue) and after (filled magenta) interaction with the seed. (b) Theoretical output pulse shape of the experimental condition in a.

from ($\partial n/\partial T = -0.8 * 10^{-4} K^{-1}$ at 20°C [53]) down to 0 at 4°C. This low coefficient alleviates the hydrothermal perturbation effect. One drawback of water is its enhanced absorption in the vis-NIR range, as compared to liquid fluorocarbon, so compression has to be carried out with 532 nm pulses. The green beam is expanded to 32 mm diameter in order to keep light intensity just below the SBS threshold in the amplifier. For thermal isolation, we designed a SBS cell with two concentric glass tubes. Water from a temperature stabilized chiller is circulated through the outer

mantel to ensure temperature uniformity and stability in the inner tube. The inner tube is filled with high purity water (OmniSolv, EMD Milipore) as SBS medium. Thermal isolation successfully reduced the pointing fluctuation of the pump beam to be below 40 μrad within 4 hours. This is about 70X better than using FC72 as the SBS medium as shown in Fig. 3.13.

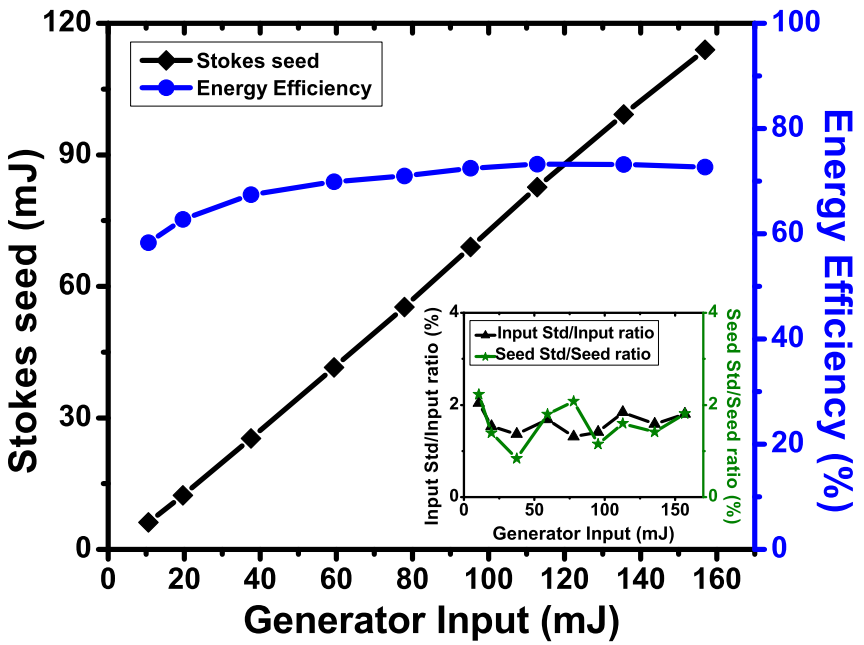

Figure 3.16: Output energy of Stokes seed (solid diamond) and corresponding energy efficiency (solid circle) with different generator input energy; Inset: Ratio between input standard deviation (Std) and input energy (solid triangle); Ratio between seed standard deviation and Stokes seed energy (solid star).

To assess the performance of the setup, we start by characterizing the seed pulse from the generator. As illustrated in Fig. 3.16, the energy reflectivity of the generator saturates at about 73%, for an input energy above 90 mJ. We measure the relative energy fluctuation in the generated seed pulse to be around 2%, which matches the amount of fluctuation in the input beam (Fig. 3.16 inset). This observation implies that the SBS process in the generator is extremely stable. The stability is further

demonstrated by the small fluctuation in pulse width (Fig. 3.17), when the input energy exceeds 90 mJ. The maximum deviation of pulse width, measured for 80 laser shots, is about (±)10 ps. We achieve a minimum compressed pulse width of 309 ps at the highest input energy of 160 mJ. Larger input energy will drive this compressed pulse width even closer to the phonon lifetime limit (295 ps) of water at 532 nm, but the reflected Stokes will also become strong enough to trigger stimulated Raman scattering (SRS), making the SBS unstable. An input energy of 120 mJ, which produces seed pulses with ∼90 mJ and ∼325 ps from the generator, is chosen for subsequent compression experiments.

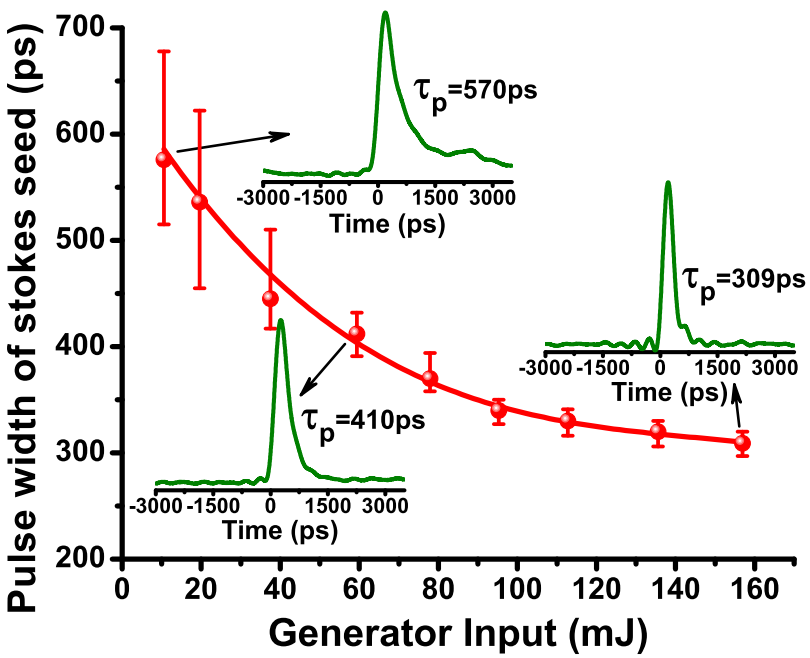

Figure 3.17: Pulse width evolution of Stokes seed with respect to generator input energy. Solid circles denote measurements of seed pulse width and the solid curve is a fit to the measurements; Error bar shows the maximum deviation of pulse width from the mean value; Three insets show typical compressed pulse shapes for corresponding input energy.

The seed pulse enters the amplifier cell and interacts with the pump pulse, during which energy gets transferred from the high energy pump pulse to the low energy

seed pulse through the transient phonon field created in the SBS medium. The seed pulse eventually exits the amplifier cell as a sharpened and amplified pulse with a temporal width close to the phonon lifetime of the SBS medium. To determine the minimum seed energy required to extract a pump energy of ∼2.2 J, we varied the input seed energy (by inserting a half-wave plate and a polarizer in between TP2 and QW2 in Fig. 3.7) and monitored the output (amplified Stokes pulse). As shown in Fig. 3.18, the maximum extracted energy is close to 1.2 J and with a stability of 2% energy fluctuation (not shown in figure). The total losses L (sum of water absorption and loss from optics) of amplification process was measured by subtracting from the total input energies (pump E_p and seed E_s) the sum of the transmitted (depleted) pump E_d and the amplified Stokes pulse E_{AS}. The SBS energy extraction efficiency is then defined as $\eta_{ex}=E_{AS}/(E_p + E_s - L)$ and is also plotted in Fig. 3.18. The maximum of ∼75% extraction efficiency is comparable to the literature [44]. Both extracted energy and extraction efficiency saturated at a seed energy of ∼90 mJ. At this point, the peak intensity of the seed pulse (due to compression in the *generator* cell) matches that of the uncompressed pump pulse, leading to most efficient nonlinear interactions

Finally, a typical temporal trace of the amplified Stokes pulse is shown in Fig. 3.18 (a), together with the initial pulse shape (inset). Fig. 3.18(b) is the calculated pulse shape. We achieved ∼40 fold compression in pulse width (from ∼12 ns to ∼300 ps) and a peak intensity of >3 GW at 532 nm. The maximum compressible energy of the current setup is around 2.4 J, limited by SBS return of the pump beam itself in the amplifier cell and stimulated Raman scattering in the generator cell, both of which can be further improved by switching to larger optics.

In the end, SBS compression in a generator-amplifier setup with water as the nonlinear medium provided the most promising result. The output optical pulse, when further converted to UV (266 nm), is well suited to pump the three-photon ioniza-

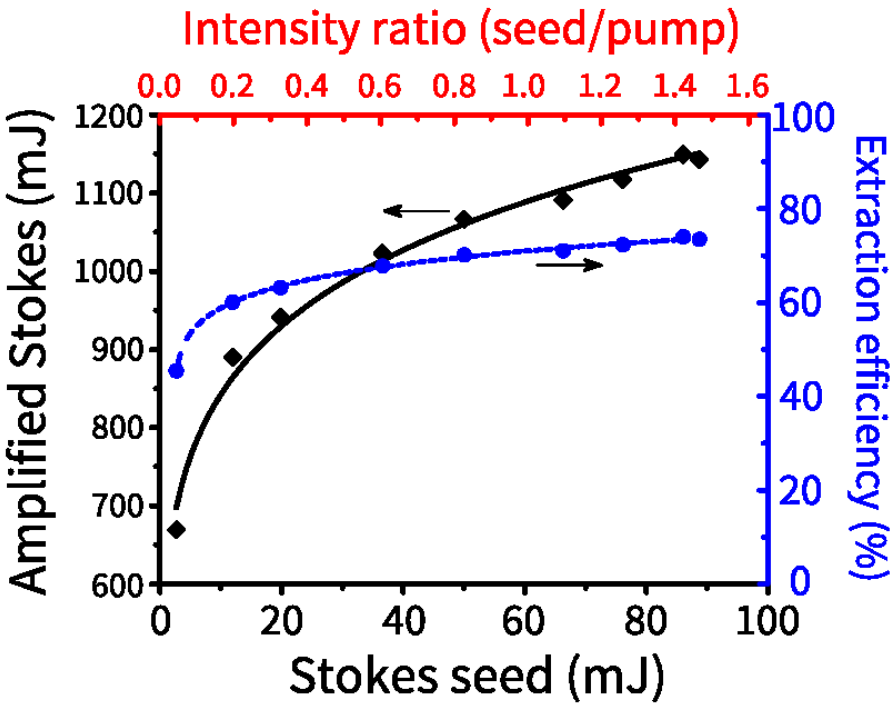

Figure 3.18: (a) Amplified Stokes energy and extraction efficiency for SBS amplification process. Solid diamonds denote measured output energy ; Solid circles denote extraction efficiency. The solid and dashed curves are a fit to the data. The energy of the input pump pulse is fixed at 2.2 J. (b) Amplified output pulse of 300 ps and 1.2 J. The inset shows the input pulse of 12 ns.

tion process of oxygen, the four-photon ionization process of nitrogen and eventually facilitate the creation of ionized plasma channels in air for laser guided discharge. It will also serve as an improved UV/VIS source for laser-induced breakdown studies.

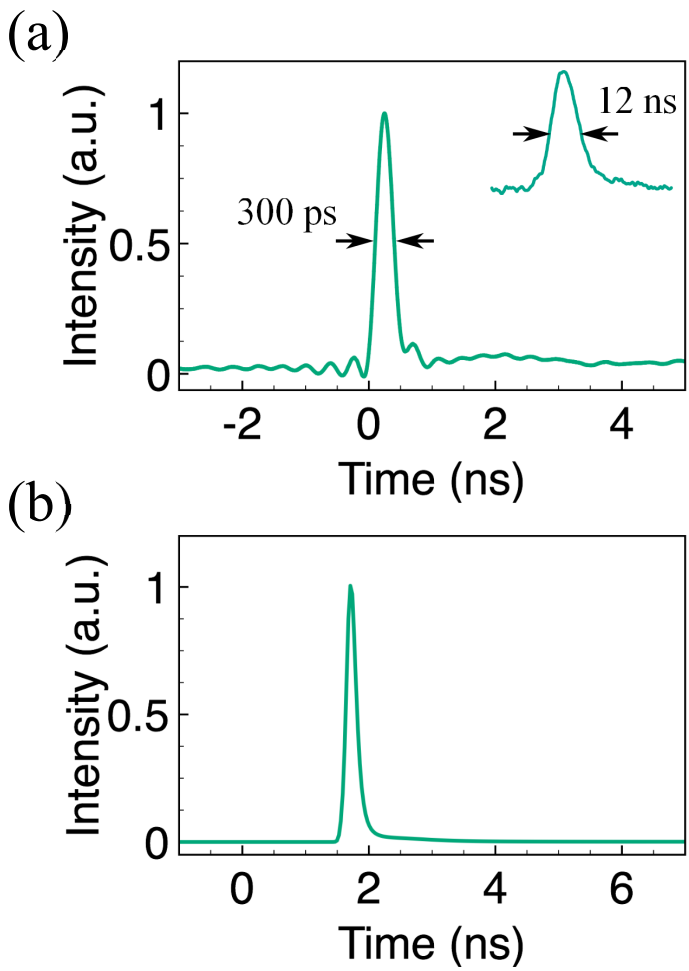

Figure 3.19: (a) Amplified output pulse of 300 ps and 1.2 J. The inset shows the input pulse of 12 ns. (b)Theoretical output pulse shape of the experimental condition in a.

Chapter 4

6-stage single-pass Nd:YAG amplifier and harmonic generations

In this chapter, we describe the amplifier and the harmonic generation units of our laser system. Since the physical principles of these modules are well established, here we focus on practical design considerations and beam characterization. First we describe our engineering efforts to maximize the energy extraction efficiency from the gain medium (i.e. flash-lamp pumped Nd:YAG rods). This includes selecting the optimal spatial mode and beam expansion. We then give a simple design recipe to avoid optical damage from unintentionally focused back reflections. This is followed by engineering considerations in the harmonic generation unit, where we compared the performance of different SHG crystals.

4.1 Super-Gaussian beam generation

In a laser amplifier, energy stored in population inversion needs to be efficiently extracted via stimulated emission. Consequently, for optimal amplification, the population inversion distribution needs to overlap with the optical fields in both space and time. While temporal overlap can be achieved by synchronizing the flash lamp pump to the master oscillator, optimal spatial overlap is less straightforward to accomplish. Ideally one would want a "top-hat" spatial profile that matches perfectly the spatial extent of the YAG rod. However, such a beam produces ringing (e.g. high spatial-frequency modulation) in the far field due to the "knife-edge" diffraction effect. To achieve maximum overlap between the beam and the rod while avoiding intensity ringing, a super-Gaussian spatial mode can be used.

In essence, a super-Gaussian mode is an "apodized" top-hap mode: intensity is flat near the beam center but near the edge, instead of abruptly dropping to zeros as in a "top-hat" beam, a super Gaussian mode smoothly tapers off to zero. Mathematically, it is described as

$$I_i(r) = I_0 \exp(-2(\frac{r}{w})^n) \tag{4.1}$$

where n is the super-Gaussian order. The higher the order, the sharper the near-edge transition is and the more it looks like a "top-hat" beam.

A super-Gaussian beam can be generated by a unstable cavity with a tapered reflectivity mirror such as a mirror with a super-Gaussian reflectivity profile [54] . The reflectivity of a GRM mathematically can be described as:

$$R(r) = R_0 \exp(-2(\frac{r}{w_m})^n) \tag{4.2}$$

where n is the Gaussian order of the reflectivity profile and w_m denotes the $1/e^2$ radius of reflectivity on the GRM. It can be shown that the self-repeating fundamental mode

of the cavity is a super-Gaussian with the same order, i.e.

$$I_i(r) = I_0 \exp(-2(\frac{r}{w_i})^n) \tag{4.3}$$

where w_i is the intra-cavity mode size and can be calculated by

$$w_i = w_m(M^n - 1)^{1/n} \tag{4.4}$$

and M is magnification factor of the cavity.

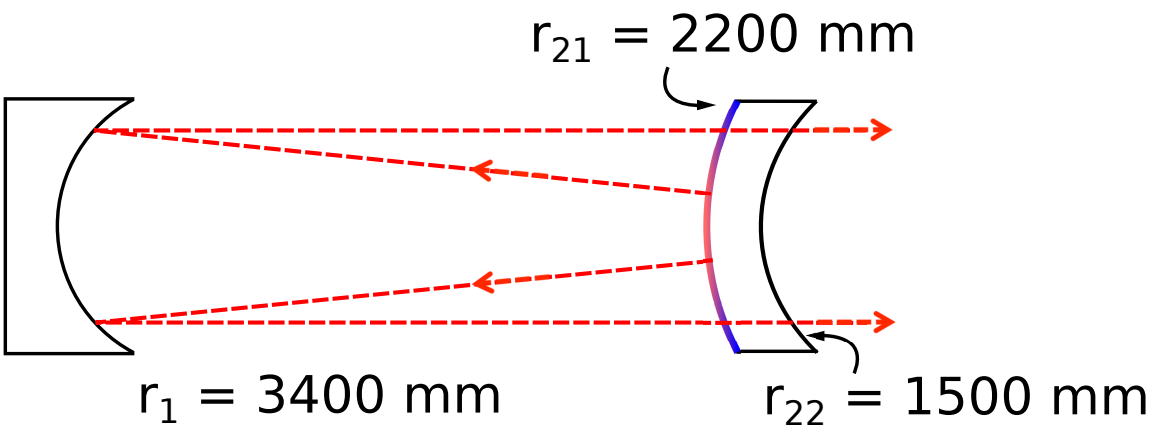

Figure 4.1: Schematic of the oscillator design. The output coupler on the right is a graded reflectivity mirror (GRM).

The output of the cavity can be derived to be

$$I_{\text{out}}(r) = I_0[1 - R_0 \exp(-2(\frac{r}{w_m})^n)] \exp(-2(\frac{r}{w_i})^n) \tag{4.5}$$

Note that once coupled out, the mode is no longer super-Gaussian with the same order and its intensity profile depends on R_0 and M. In other words, super-Gaussian mode is straightforward to generate inside a cavity but difficult to maintain during its propagation through the amplifier chain. Our goal is to keep the intensity as close as an approximated super-Gaussian during beam amplification.

As can be shown by Eq.4.5, when $R_0 > 1/M^n$, an intensity dip appears at beam center. To generate a "flat-top" near the beam center, we need $R_0 = 1/M^n$. This is our design goal of the optimal GRM.

Several additional factors need to be taken into account. For example, in a cavity with saturated gain, the magnification factor is not the same as the geometrical magnification factor but usually bigger. The higher the gain, the bigger the M. The diffraction from the small area of reflective coating also make the effective magnification factor bigger [reference]. These need to be taken into account when designing the GRM.

The cavity design is illustrated in Fig. 4.1. It is a confocal unstable cavity with geometric magnification M = 1.55. The end mirror on the right-hand-size is a GRM. Two different GRMs, whose measured reflectivity profiles are shown in Fig. 4.2, were tested. The one on the left has a higher R_0 and produces an output with a

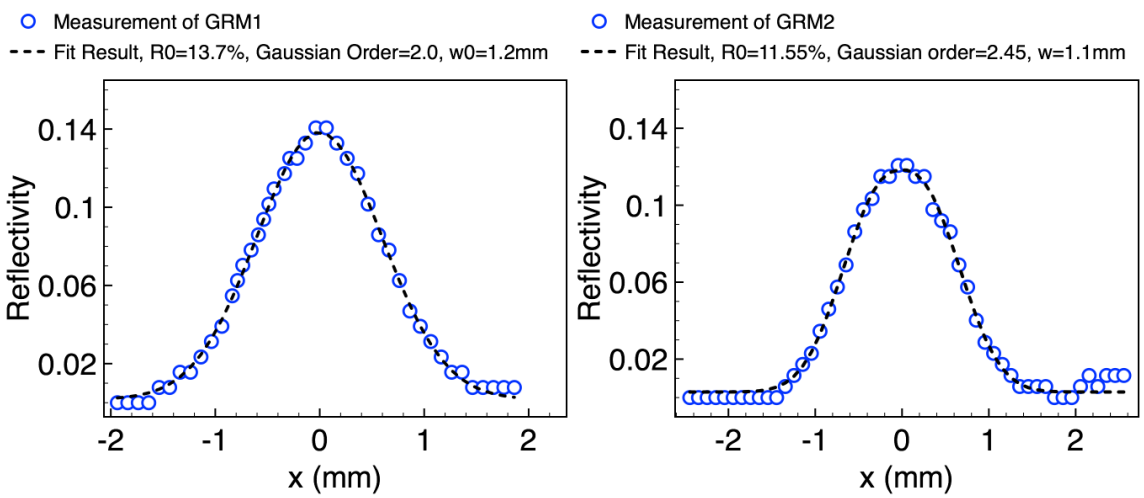

Figure 4.2: Measured reflectivity profile of two different GRMs. Left: a GRM with a super-Gaussian order n = 2.0 and a peak reflectivity of 13.7%. Right: a GRM with a super-Gaussian order n = 2.5 and a peak reflectivity of 11.6%.

bigger dip. The one on the right we can still see a small dip (see Fig. 4.4). As the beam propagates, the beam profile changes and the central dip becomes a peak, as shown by measured profile in Fig. 4.3b. This was mostly due to the fact that the real magnification factor is much bigger than the geometrical magnification factor (measured M = 2.65 compared to 1.55). Such local intensity inhomogeneity in the beam profile is undesirable during the amplification and SHG stages.

Using the measured magnification factor (M = 2.65) we simulate the output from

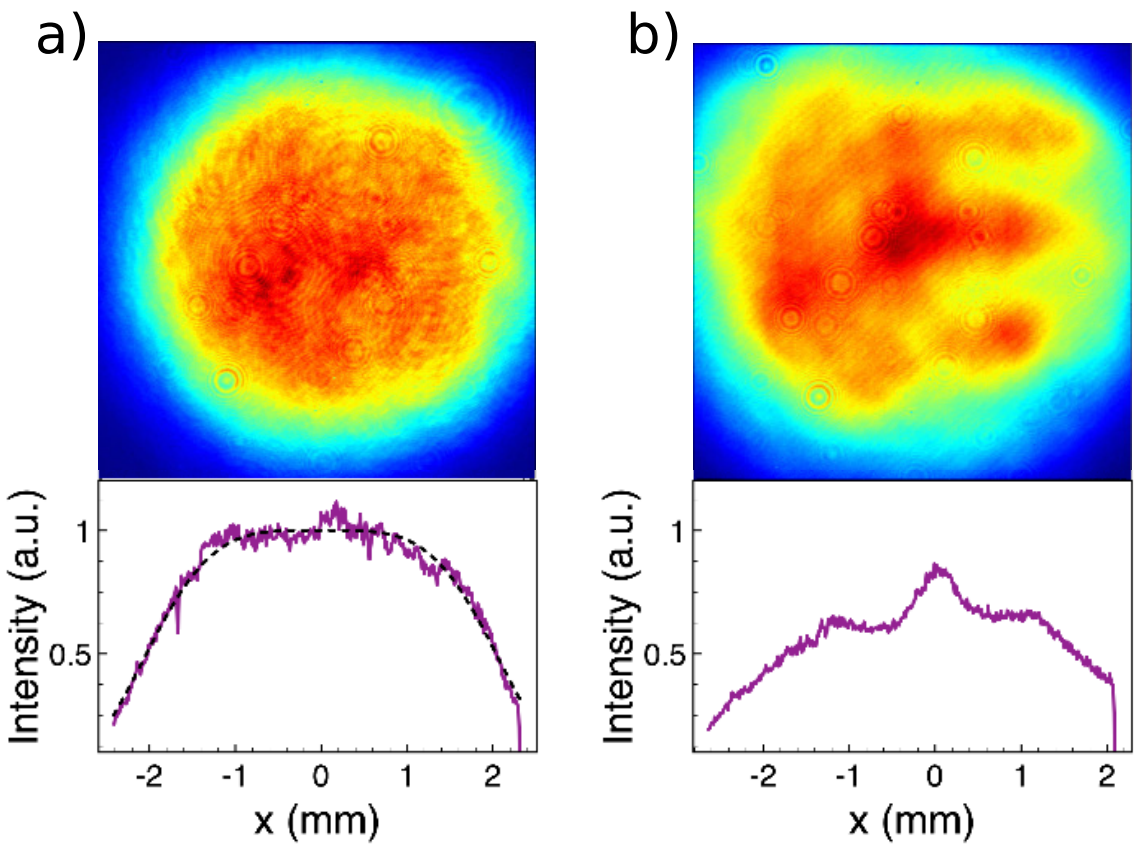

Figure 4.3: Beam profile of the oscillator output, using the GRM on the right of Fig. 4.2. a)10 cm from the output coupler; b) 70 cm from the output coupler

the two GRM shown in Fig. 4.4. A central intensity dip is clearly seen in both cases. We designed a new GRM mirror to improve the output beam profile. The simulated

output profile is shown in Fig. 4.5. It remains to be seen how much improvement the new design brings to the laser system.

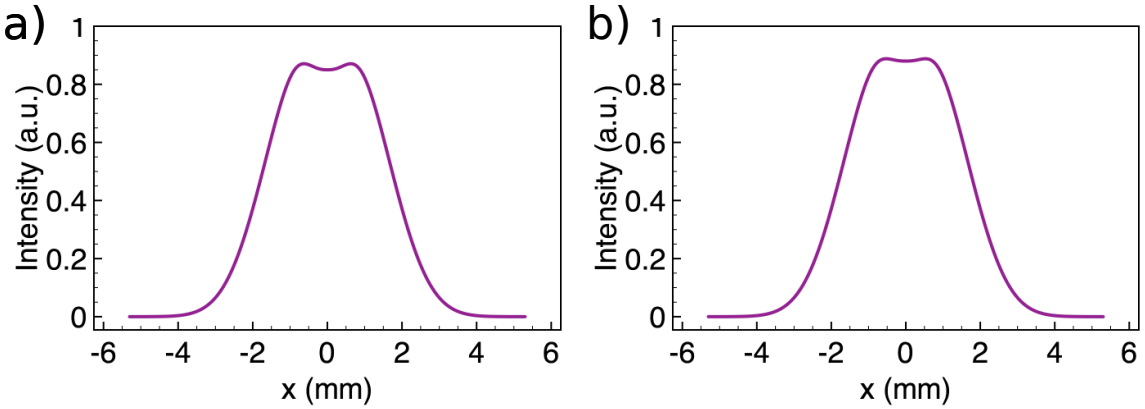

Figure 4.4: a) Simulated output spatial intensity profile with GRM1 b) Simulated output spatial intensity profile with GRM2

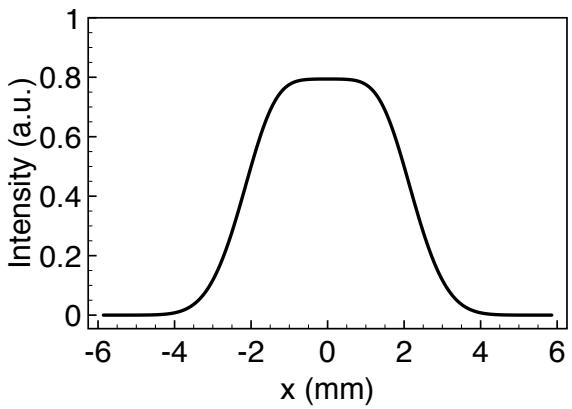

Figure 4.5: Simulated output spatial intensity profile with a new GRM mirror: R_0=20.6%, w_m=1.89, n=2.85

4.2 Beam expander design

Before each amplification stage, a beam expander is used to (slightly) expand the beam for maximum filling of the rod without clipping. The original design of the

beam expander is a three-lens system shown in Fig. 4.6a. Varying the distances between the three lenses allows magnification tuning from 0.5 to 2. Despite of its flexibility to match a rod of arbitrary size, this design suffers from a number of disadvantages. We found that a simple Galilean telescope, shown in Fig. 4.6b is more suitable for our applications. Here we discuss the design considerations and compare the two geometries.

4.2.1 Back-reflection consideration

In a high-power laser system, careful control of the back-reflected beam is critical. If the back reflection focuses on an upstream optics, it causes optical damage. If the back reflection focuses in air, it can create a "plasma bubble" that strongly scatters and distorts the pulse. In our application, for example, even a 0.5% back reflection is powerful enough to induce damage when unintentionally focused. To address this, we used ABCD beam propagation method to back trace the reflection from very surface. This procedure allowed us to identify all possible "ghost spots".

For example, in the telescope shown in Fig. 4.6, there are three back reflection paths that might cause problems: the flat surfaces of L1, L2 and L3. Reflection off L1 focuses at around $f_1/2$ to the left of L1. Reflection off L2 focuses to the left of L1 as well, but at a distance much closer to L1. Where reflection off L3 focuses depends on the alignment: for a well-aligned telescope that produces a collimated output, the back reflection will go through L2 before focusing. In this case, a focused spot is avoided. On the other hand, when the output is slightly converging, the back reflection could focus somewhere in the return path, posing damage threat to upstream optics. In practice, problems from back reflection are mitigated by a) always placing the beam expander at least 15 cm away from the previous YAG rod and b) making sure that output of the telescope is collimated or slightly diverging.

However, satisfying a) increases the distance between amplifiers and worsens the beam profile due to propagation effects of the non-Gaussian beam (Fig. 4.3b.)

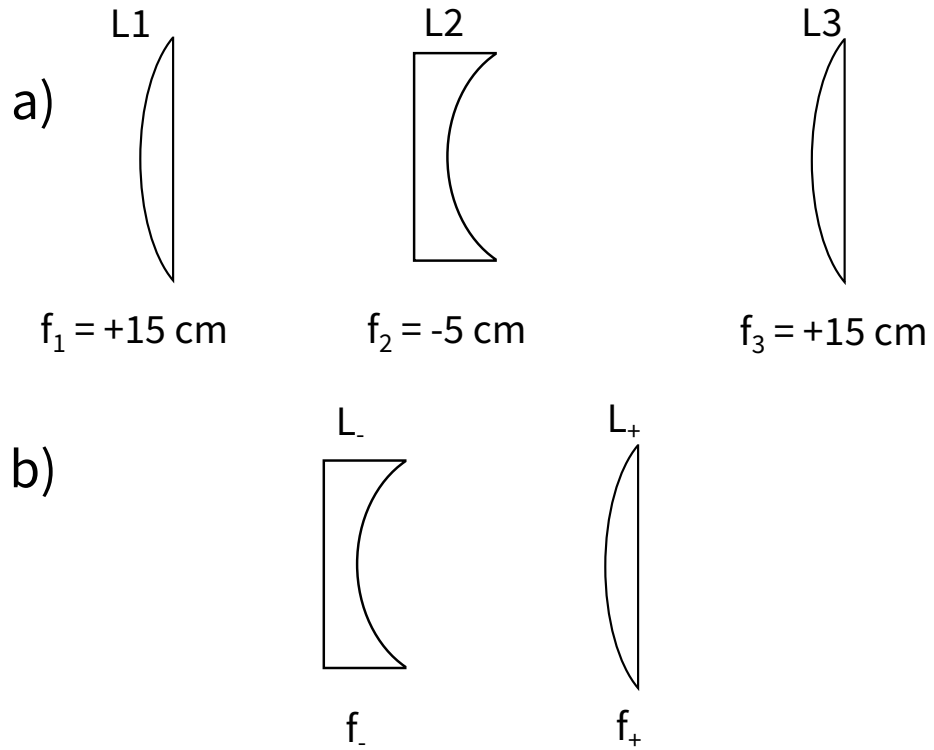

Figure 4.6: Two beam expander designs. a) the three-lens geometry with tunable expansion ratio. b) the single Galilean design, the focal lengths of the two lenses depends on the desired expansion ratio.

In the Galilean telescope geometry (Fig. 4.6), back reflections do not focus and each telescope can be placed as close as physically allowed to the previous rod to limit propagation effects.

4.2.2 Aberration consideration

Spherical aberration prevents the laser beam from achieving diffraction-limited spot size, thus limiting the efficiency of the nonlinear processes (e.g. SBS and SHG). The

three-lens telescope design introduces a lot of spherical aberration to the system, mainly by L2 due to the large curvature of the spherical surface. Previously it was suggested that replacing L3 with a gradient index lens help reduce the spherical aberration [55]. However, we found the effect to be quite minimum.

The Galilean telescope design is intrinsically superior in aberration performance. By design, the spherical aberration coefficients of L_- and L_+ are of opposite sign so the contribution from the two lenses tends to cancel each other [56].

In the end, with the super-Gaussian cavity (Fig. 4.1) and the beam expander design in Fig. 4.6b, we achieved a fill factor of ~64% (i.e. the beam size is about 80% of the size of the rod). A super-Gaussian beam with a higher order may further improve the fill factor, although commercial GRM that satisfies the design is currently unavailable.

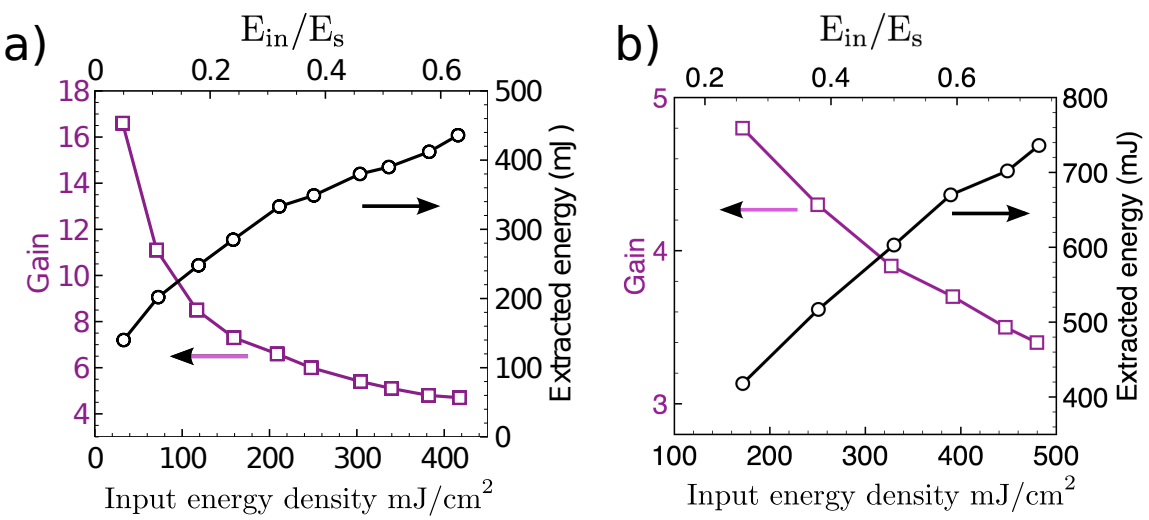

Figure 4.7: Amplification gain (left, magenta axis) and extracted energy (right, black axis) as a function of the energy density of the input, at a constant flash-lamp energy of 75 J. a) First amplifier stage with a 8 mm rod. b) Second amplifier stage with a 12 mm rod.

4.3 Energy extraction measurements of Nd:YAG amplifiers

In this section we show actual measurement result of our amplifier stage. Fig. 4.7 shows the amount of extracted energy (right axis) as a function of input energy density (or equivalently, input energy density normalized to the saturation energy density, which, for Nd: YAG is $E_s = 660$ mJ/cm^2). The corresponding gain, which clearly shows the saturation behavior as E_{in}/E_s approaches 1, is plotted on the left axis. At the first amplifier stage, we achieved an overall extraction efficiency ~50% with our design.

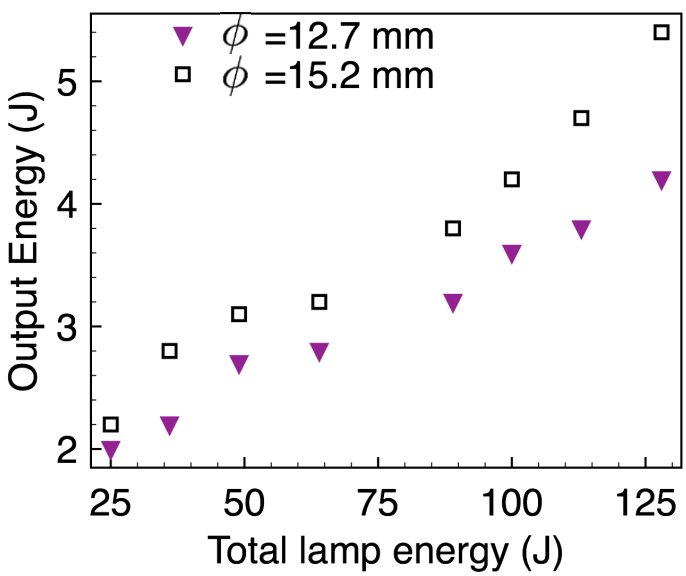

Figure 4.8: Energy input-output relation of the final two amplification stages (combined). Black squares, the case with slight under filling of the laser rod ($\phi = 12.7$ mm, beam diameter). Magenta triangles, the case with optimal filling ratio ($\phi = 12.7$ mm).

To illustrate how beam fill factor influences the energy extraction efficiency, we plot in Fig. 4.8 the output energy as a function of pumping energy for the final two

amplification stages (combined), for two different beam sizes. Here, the rod diameter is about 19 mm and a better filling factor (beam size of 15.3 mm compared to 12.7 mm) led to ∼28% more extracted energy. Since a further increase in beam diameter causes clipping near the edges, we decided $\phi = 15.3$ to be optimal.

4.4 Spatial-temporal coupling of the amplified pulses

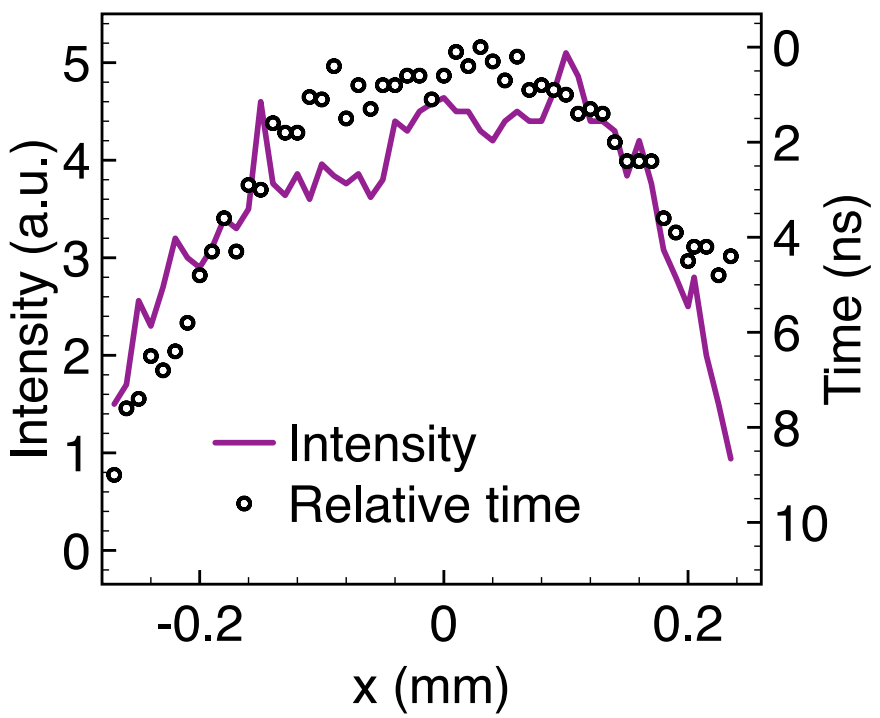

Figure 4.9: Spatial-temporal coupling measurement of the amplified pulse. Magenta: intensity distribution; Black circles: relative arriving time.

One very interesting observation was made regarding the spatial-temporal properties of the output pulse. Here, we scan a pinhole across the beam profile to map out the intensity and arrival time as a function of spatial coordinate. In Fig. 4.9,

the result along one dimension through the beam center is shown. In the intensity channel (magenta, left axis), we observed a super-Gaussian like profile as designed. Intriguingly, the arrival time of the pulse also depends on the spatial coordinate and it has a shape that follows the intensity profile. More specifically, the center of the beam arrives earlier than the edge of the beam, and the time difference is as large as ∼8 ns!

We understand this interesting phenomenon as arising from gain saturation during the amplification process. First, consider the high-intensity portion of the beam, as it propagates through the amplifiers, the gain may saturate at the leading edge of the pulse and later becomes depleted for the falling edge of the pulse. The net effect is the beam gets "pushed forward" and appears to be propagating faster than its phase velocity in the medium. On the other hand, the low-intensity portion of the beam experiences less (or no) saturation effect and propagates close to its nominal phase velocity.

4.5 Two strategies of producing 266 nm pulses

We tried two different strategies of generating 266 nm from the 1064 nm fundamental. In strategy one (see Fig. 4.10 for schematics and Fig. 4.11 for actual lab photos of the modules), light produced by the oscillator (∼ 120 mJ) was first boosted by 4 amplifier stages to ∼ 1 J. Then, the amplified 1064 nm pulse was compressed using SBS in FC-72. The SBS process reduced pulse width from 12 ns to ∼670 ps with ∼73% conversion efficiency. The compressed pulse (1064 nm) was then further amplified by 2 amplification stages. The measured beam profiles before and after the final 2 amplifier stages are shown in Fig. 4.12a and b, respectively. After the last amplifier, the laser beam was frequency doubled into 532 nm with a LBO crystal (see section 4.6) and then further doubled into 266 nm with a KDP crystal (see

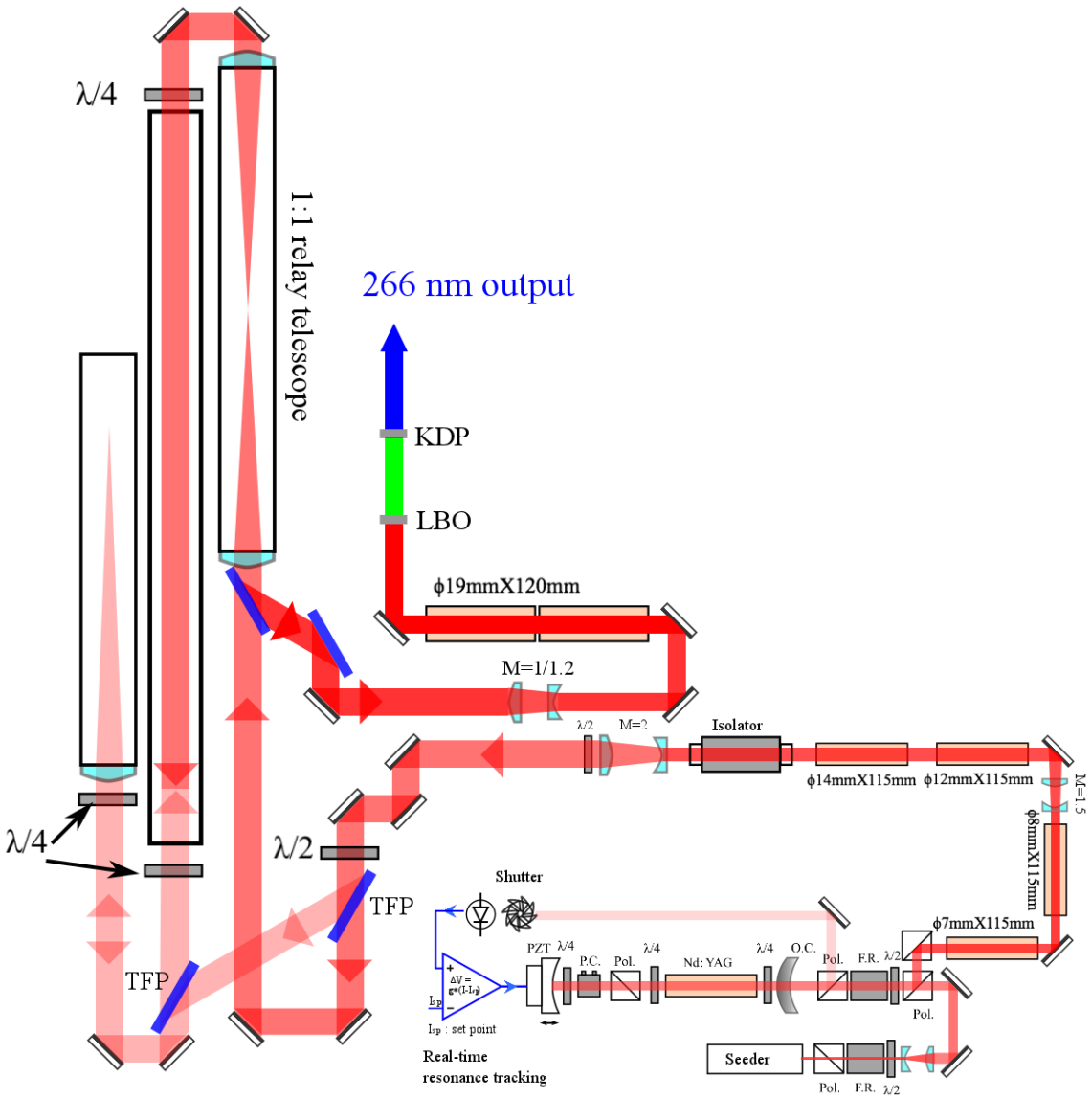

Figure 4.10: Schematic of the laser system in configuration 1, see text for details.

section 4.6).

The second strategy is illustrated in Fig. 4.13 (see Fig. 4.14 for lab photos). Output from the oscillator is first boosted by all 6 amplifiers, resulting in 12 ns pulses with up to 7 J per pulse. The 1064 nm pulse is then frequency doubled

into 532 nm with a LBO crystal (see section 4.6). SBS pulse compression in this configuration is achieved at 532 nm using water as the nonlinear medium. Finally, the compressed 532 nm pulse (∼1.2 J, ∼300 ps) is frequency-doubled into 266 nm with a KDP crystal (see section 4.6).

Both strategies produced 266 nm pulses with similar pulse energy and peak power (Fig. 4.17 right panel and Fig. 4.18 right panel). The main experimental consideration that prompted us to switch from the first configuration to the second is the thermal stability of the SBS compression process. As discussed in Chapter 3, water has a much lower thermo-optic coefficient as compared to FC-72. This makes the spatial profile of the output beam much better in the second configuration, as evidenced by burn paper recording of the output profiles in Fig. 4.16. A slight temperature gradient inside the liquid would cause astigmatism in the output beam and this effect is much more pronounced in the case of FC-72 (Fig. 4.16). However, water has a large absorption cross section at 1064 nm, due to overtones of vibronic transitions. As a result, SBS compression in water was not conducted at 1064nm but at 532 nm. Even though absorption loss in water at 532 nm is still larger compared to FC-72 at 1064 nm, our results showed that the advantages of water outweigh its drawbacks.

4.6 Second harmonic generation

The SHG unit is relatively straightforward. We designed the crystals using the SNLO software (http://www.as-photonics.com/snlo). Fig. 4.17 plots the measurement result of the two SHG stages in configuration 1. In the case of 1064-to-532 conversion, three different crystals were tested and compared. As shown in the conversion efficiency plot in the left panel of Fig. 4.17, for KDP, the efficiency first increases but then decreases as the input pulse energy increases. Similar behavior is observed in 532-to-266 conversion as well. The decrease at high input energies is due to two-

photon absorption at the second harmonic wavelength and is of particular concern in the 532-to-266 conversion. This can be eliminated by using a bigger input beam size and longer SHG crystal. Fig. 4.18 shows the results for configuration 2.

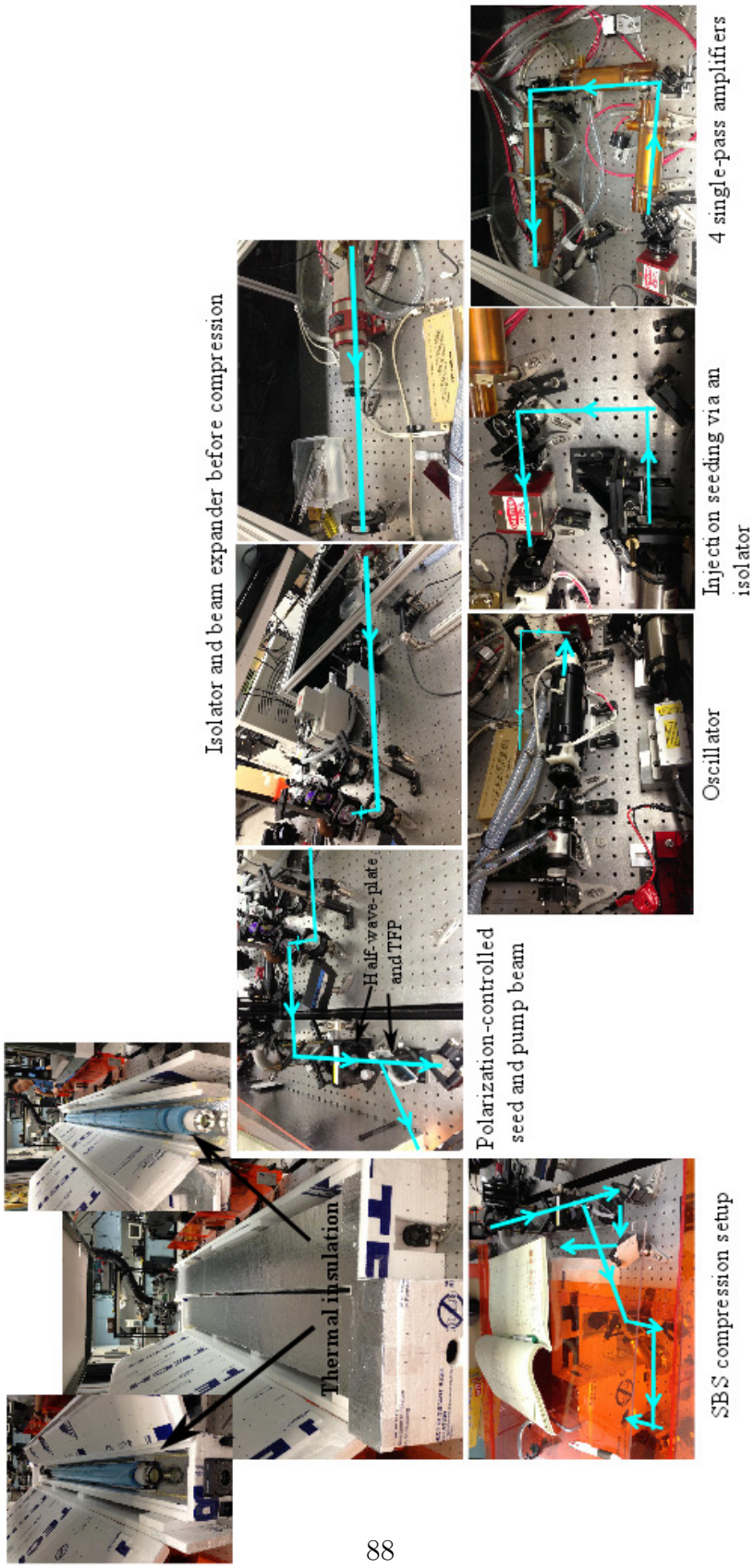
4 single-pass amplifiers
Injection seeding via an isolator
Oscillator
Isolator and beam expander before compression
Half-wave-plate and TFP
Polarization-controlled seed and pump beam
Thermal insulation
SBS compression setup

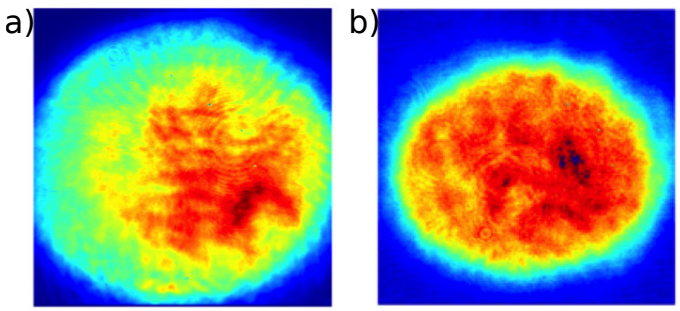

Figure 4.12: Beam profile of configuration 1. a) Beam profile after the compressor. Pulse energy: 730 mJ, pulse width: 670 ps b) Beam profile after two single-pass amplifiers, 3.7 J, 670 ps.

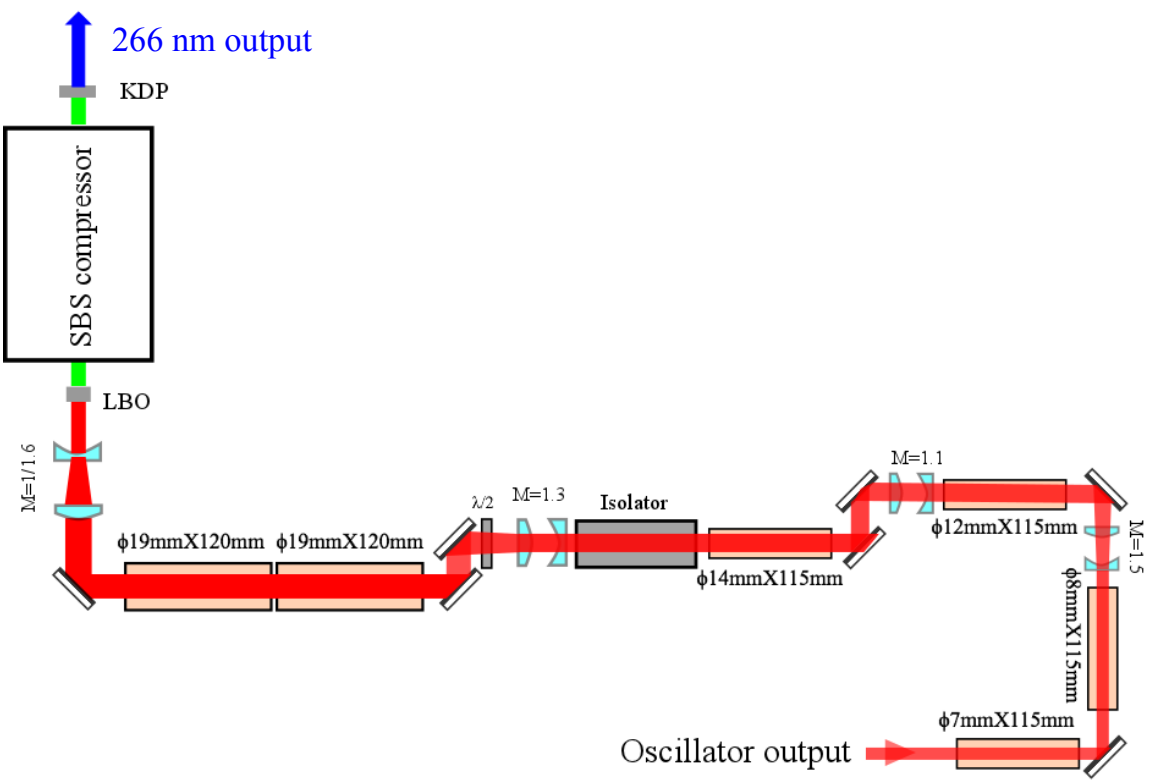

Figure 4.13: Schematic of the laser system in configuration 2

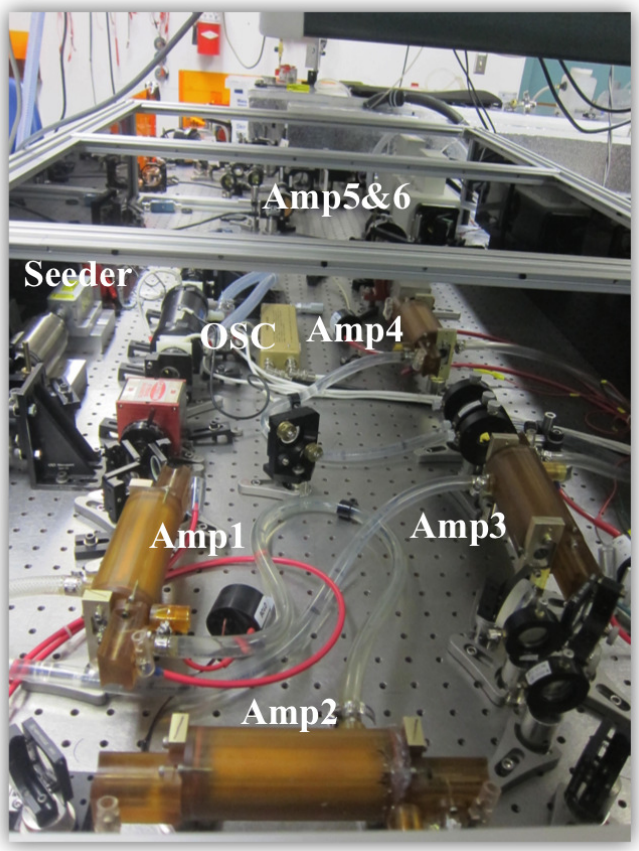

Figure 4.14: Lab pictures of the laser part in configuration 2

Figure 4.15: Laser beam profile from the 6-stage single pass amplifier on a burn paper.

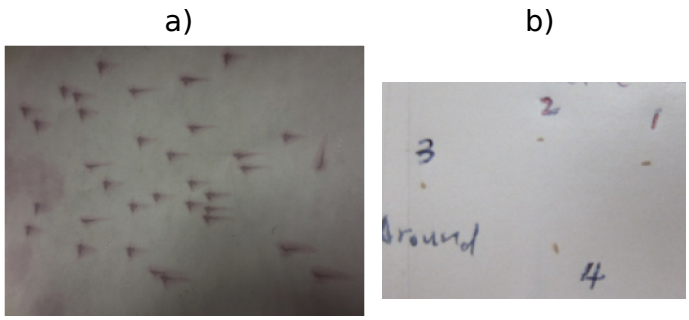

Figure 4.16: Far field patterns of two configurations. a) Configuration 1; b) configuration 2.

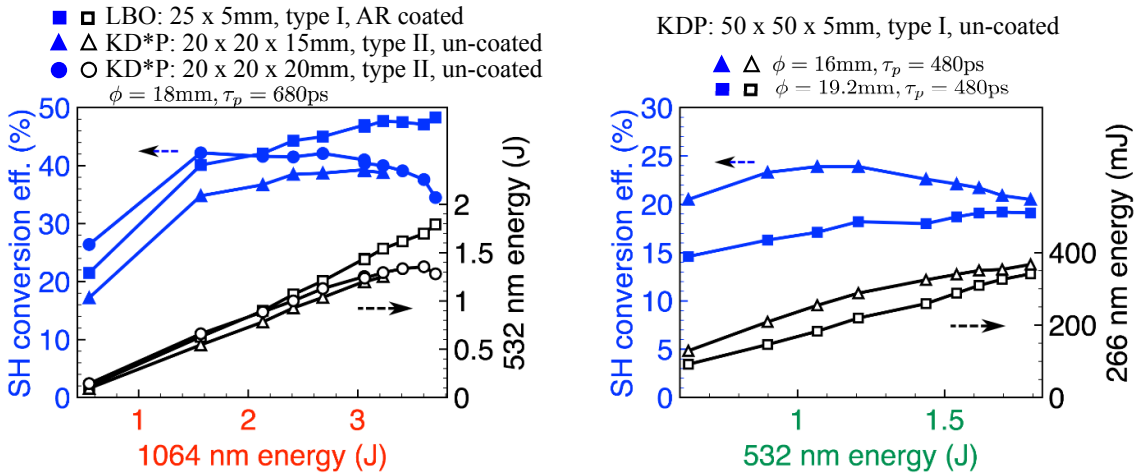

Figure 4.17: SHG performance of configuration 1. Left: 1064-to-532 conversion, ϕ, beam size, τ_p, pulse width. Right: 532-to-266 conversion

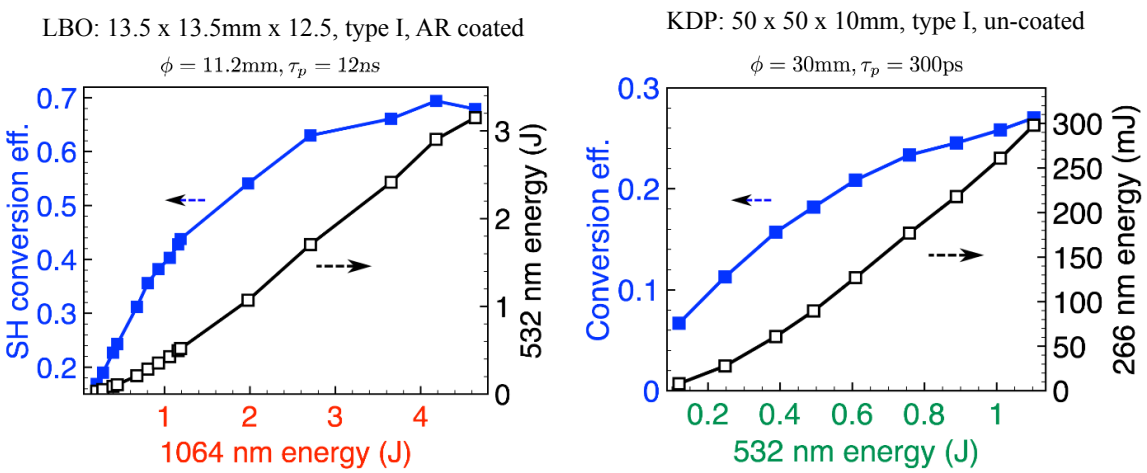

Figure 4.18: SHG performance of configuration 2. Left: 1064-to-532 conversion, ϕ, beam size, τ_p, pulse width. Right: 532-to-266 conversion

Chapter 5

High power UV source: applications and future work

Our GW UV source provides physicists a new tool to explore nonlinear optics in the atmosphere. Application of the source is the focus of current research and includes laser-guided discharge and filament generation in air. Here we summarize some early results and point to possible future work.

5.1 UV pulse guided discharge

5.1.1 Experimental arrangement

To observe high-voltage discharge in air, we used metallic spheres, 16" in diameter, as the terminal electrodes. Positive and negative DC high voltages can be applied on the two spheres independently with tunable electrical potentials. Two small holes ($\sim$5 mm in diameter) were drilled across the center of the spheres to let the laser beam pass through. We manually tune the distance between the two spheres.

5.1.2 Preliminary results

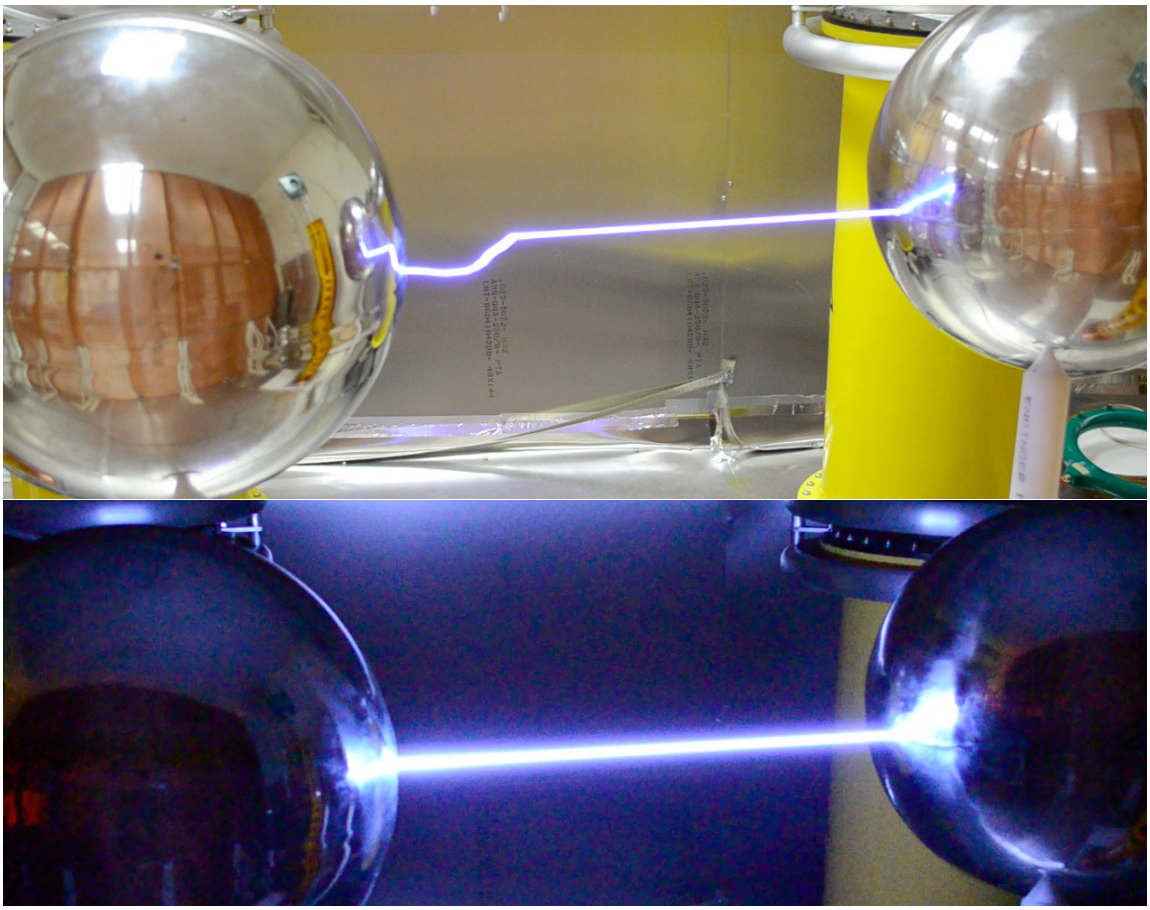

Figure 5.1: UV laser pulse guided discharge between two high DC voltage electrode.

Without the UV laser and at a separation distance of 12 cm, discharge between the two metal spheres happens when the voltage exceeds ∼250 kV. This is reasonable, considering that the self breakdown voltage is about 20 kV/cm in air. When we switched on the UV pulse (here, 12 ns pulses were used), we immediately observed a factor-of-two decrease in the breakdown voltage (the minimum voltage needed to observe discharge). As we dial up the energy from ∼40 mJ to ∼270 mJ (per pulse), the breakdown voltage further decreased and saturated to about 100 kV (Fig. 5.2a). Apparently, the presence of the UV pulse facilitated the onset of discharge.

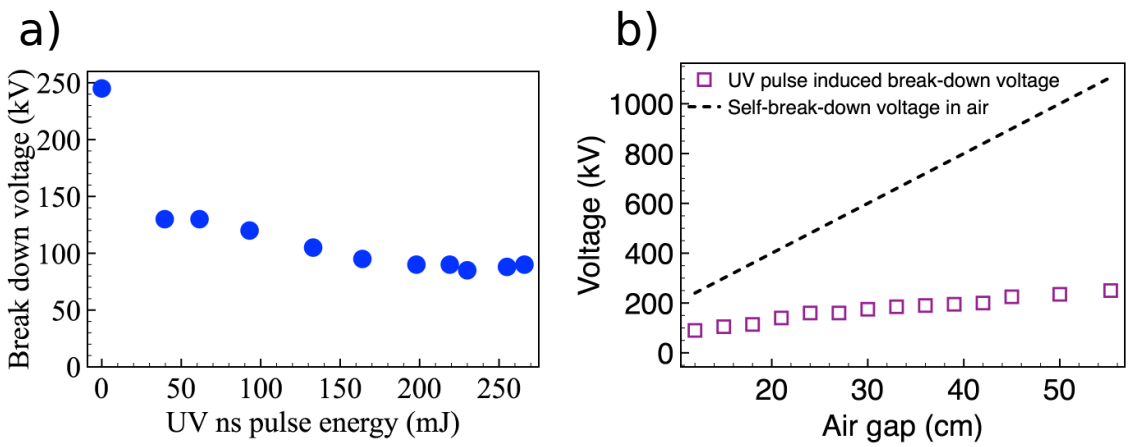

Figure 5.2:

In a separate experiment, we varied the distance between the two metal spheres and recorded the corresponding breakdown voltages (the energy per pulse is fixed at 300 mJ). The result is plotted in Fig. 5.2b. Also plotted is a theoretical model of self breakdown voltage in air (i.e. no UV pulse). With the guiding laser, the breakdown voltage has a much weaker dependence on the air-gap distances.

We also studied the time-domain behavior of the electric discharge. Interestingly, the discharge lags the guiding UV pulse by a few microsecond (Fig. 5.3 inset). Moreover, as the spacing between the two spheres increases, the discharge-to-pulse delay first remains constant, and then starts to increase once the spacing exceeds ~40 cm. This observation raises the possibility that two different mechanisms might be needed to explain the behavior below and above 40 cm.

The exact mechanism of UV laser induced discharge is currently being investigated. Previously, similar experiment has been conducted in near IR and a thermal model was proposed [9]. In this model, the lowering of discharge threshold is caused by heating followed by decreased pressure near the center region of the beam. This model is reasonable in predicting a large delay (μs) between the laser pulse and discharge. On the other hand, our UV pulse is capable of delivering much more

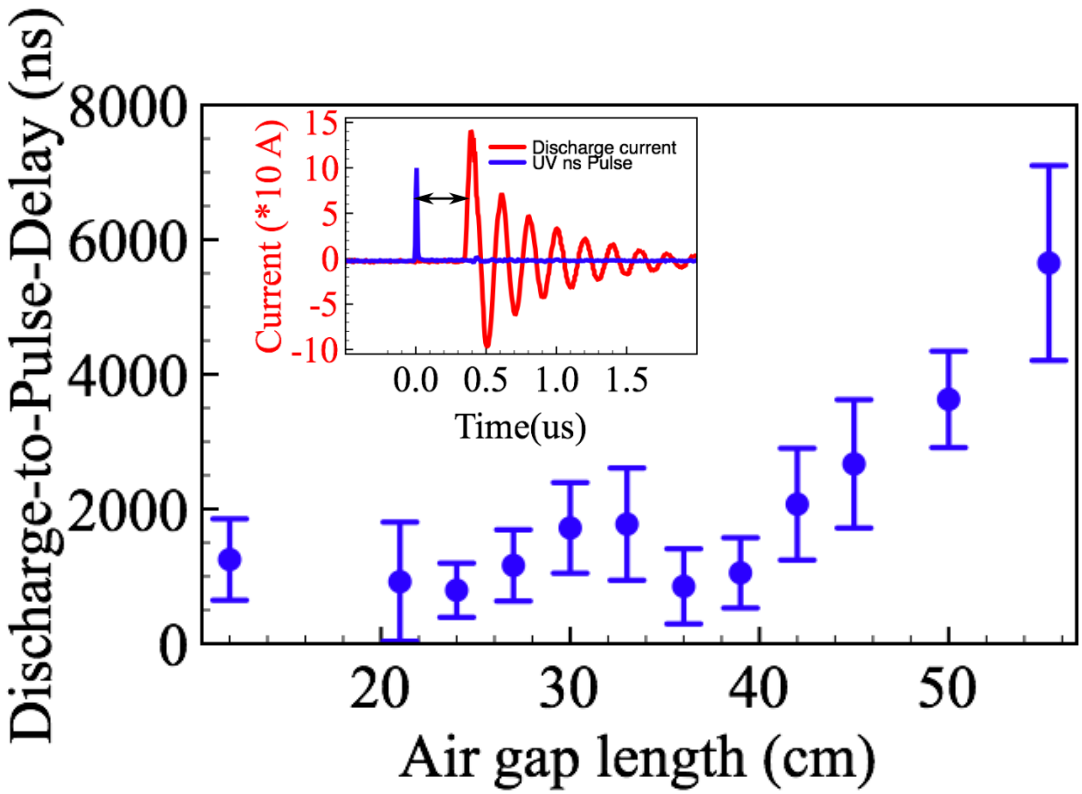

Figure 5.3:

energy compared to the near IR pulse, it would be interesting to conduct a detailed quantitative modeling for our experiment.

5.2 UV filament in air

To generate UV filament in air, the output 266 nm beam of the laser system is first focused in vacuum to avoid premature filament generation. The focused beam then goes through an aerodynamic window, where the filament initializes. The high air flow rate creates a natural gradient from vacuum ($\sim$ 10 Torr) to atmosphere pressure (630 Torr).

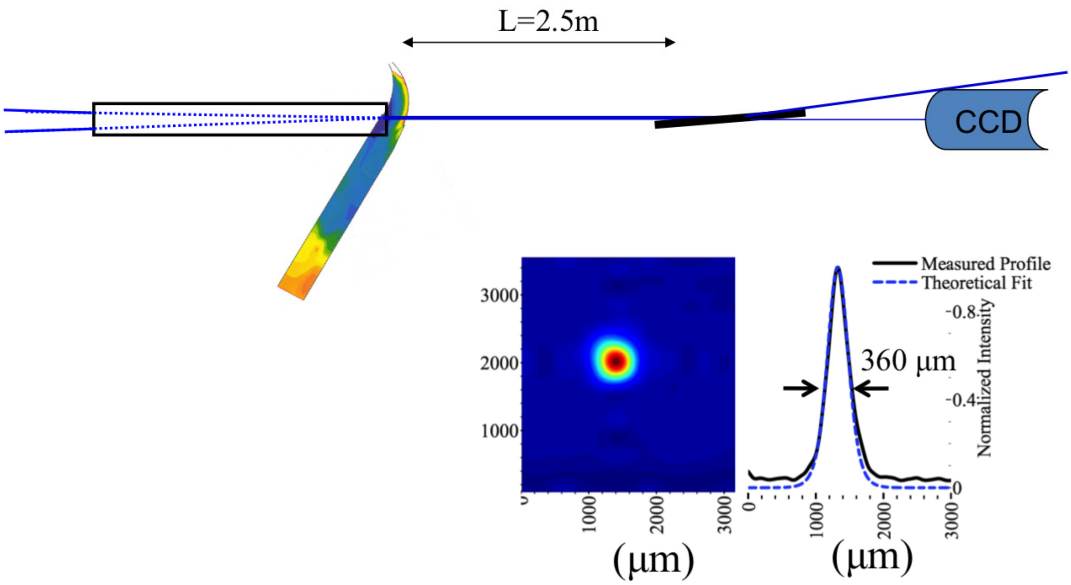

Figure 5.4: Direction imaging of UV filament in air.

Fig. 5.4b shows an image on a CCD camera at 2.5 m from the focus (attenuated by 10^6 using glazing incident on a UV-coated mirror). We observed a highly localized intensity spot with a FWHM of ∼1mm. If the beam propagates by normal diffraction, it would be the same size as the white dashed circle.

5.3 Future work

Our laser system is capable of stable generation of UV filaments in air. This represents an important first step in investigating extreme nonlinear interactions between air molecules and 266 nm photons. A number of exciting future experiments wait ahead.

5.3.1 Filament diagnostics and characterization

The high degree of stability and pulse-to-pulse reproducibility enables detailed statistical characterization of the generated filaments. Below we outline a number of interesting parameters to measure.

Filament width and length

The width of the filament determines the degree of energy concentration during propagation while the length of the filament determines how far the concentrated energy can be delivered. It is of practical importance to measure those two parameters as a function of the following experimental conditions: input pulse energy, air turbulence, temperature gradient and atmospheric humidity.

Temporal filament splitting

Niday *et al* [57] predicted that the temporal evolution of a nanosecond, UV filament might be unstable under reasonable experimental conditions. According to their model, one pulse would split into multiple picosecond sub-pulses. This can be directly measured by our current apparatus.

Time resolved light-plasma interactions

A distinctive feature of our UV filament is its sub-nanosecond duration. This is about four orders of magnitudes longer than conventional femtosecond NIR filaments. The long temporal duration will allow us to study the transient interplay between photons and plasma fields with fine details. A possible experimental approach is time-resolved diffractometry, where a weak probe beam interacts with the formed

filament and its time-dependent spatial profile provides direct information of the time-varying refractive index.

Optical signals generated by filaments: Raman and fluorescence

For potential remote sensing applications, it is important to analyze the optical signal *generated* by the UV filament. Radiation from a UV filament includes (but not limited to) Raman and fluorescence from molecules in air. These experiments can be conducted by collecting signal orthogonal to filament propagation and analyzing the spectral components using a high-resolution grating spectrometer. Time-resolved fluorescence measurement, which probes population evolution of ionized nitrogen [58] in air with sub-nanosecond resolution, might provide additional insight to transient plasma dynamics during filament formation.

5.3.2 Nested IR and UV filament

Due to loss by conical emission, one single IR filament generally can only propagate less than one meter in air. It might be possible to co-propagate a UV filament with an IR filament and use the energy in the UV filament as an energy reservoir that continuously replenish the IR. Energy exchange between the IR and UV might be accomplished by a parametric four-wave mixing process. Recently, a similar idea, which uses a Bessel "dressing" beam to supply energy to the central filament beam has been realized experimentally [59]. The authors successfully extended the longevity of a single IR filament by $\sim$10 fold.

5.3.3 Outdoor experiments

Eventually, outdoor experiments should be possible if long propagation distances can be realized. Remote sensing and analysis of atmosphere contents would be an important application. Previously, LIDAR (LIght Detection And Ranging) experiments have been conducted with IR filmanent produced by the teramobile laser. Recently, it has been shown that UV-based sensing gives much clearer signature when trying to detect explosive materials [60].

Appendices

References

[1] Q. Wang and W. Moerner, "Single-molecule motions enable direct visualization of biomolecular interactions in solution," Nature methods (2014).

[2] J. Cen, P. Yuan, and S. Xue, "Observation of the optical and spectral characteristics of ball lightning," Physical Review Letters **112**, 035001 (2014).

[3] E. P. Krider, "Benjamin franklin and lightning rods," Physics Today **59**, 42–48 (2006).

[4] G. Ostrovskaya *et al.*, "Laser spark in gases," Soviet Physics Uspekhi **16**, 834 (1974).

[5] J. Kasparian, R. Sauerbrey, and S. Chin, "The critical laser intensity of self-guided light filaments in air," Applied Physics B **71**, 877–879 (2000).

[6] L. Bergé, S. Skupin, R. Nuter, J. Kasparian, and J. Wolf, "Ultrashort filaments of light in weakly ionized, optically transparent media," Reports on progress in physics **70**, 1633 (2007).

[7] A. Braun, G. Korn, X. Liu, D. Du, J. Squier, and G. Mourou, "Self-channeling of high-peak-power femtosecond laser pulses in air," Optics letters **20**, 73–75 (1995).

[8] X. M. Zhao, J.-C. Diels, C. Y. Wang, and J. M. Elizondo, "Femtosecond ultraviolet laser pulse induced lightning discharges in gases," Quantum Electronics, IEEE Journal of **31**, 599–612 (1995).

[9] S. Tzortzakis, B. Prade, M. Franco, A. Mysyrowicz, S. Hüller, and P. Mora, "Femtosecond laser-guided electric discharge in air," Physical Review E **64**, 057401 (2001).

[10] H. Wille, M. Rodríguez, J. Kasparian, D. Mondelain, J. Yu, A. Mysyrowicz, R. Sauerbrey, J.-P. Wolf, and L. Woeste, "Teramobile: A mobile femtosecond-terawatt laser and detection system," The European Physical Journal Applied Physics **20**, 183–190 (2002).

[11] J. Kasparian, M. Rodríguez, G. Méjean, J. Yu, E. Salmon, H. Wille, R. Bourayou, S. Frey, Y.-B. André, A. Mysyrowicz *et al.*, "White-light filaments for atmospheric analysis," Science **301**, 61–64 (2003).

[12] P. Rohwetter, J. Kasparian, K. Stelmaszczyk, Z. Hao, S. Henin, N. Lascoux, W. M. Nakaema, Y. Petit, M. Queißer, R. Salamé *et al.*, "Laser-induced water condensation in air," Nature Photonics **4**, 451–456 (2010).

[13] J. Kasparian, R. Ackermann, Y.-B. André, G. Méchain, G. Méjean, B. Prade, P. Rohwetter, E. Salmon, K. Stelmaszczyk, J. Yu *et al.*, "Electric events synchronized with laser filaments in thunderclouds," Optics express **16**, 5757–5763 (2008).

[14] P. Rambo, J. Schwarz, and J.-C. Diels, "High-voltage electrical discharges induced by an ultrashort-pulse uv laser system," Journal of Optics A: Pure and Applied Optics **3**, 146 (2001).

[15] J. Schwarz and J.-C. Diels, "Analytical solution for uv filaments," Physical Review A **65**, 13806 (2002).

[16] O. Chalus, A. Sukhinin, A. Aceves, and J.-C. Diels, "Propagation of non-diffracting intense ultraviolet beams," Optics Communications **281**, 3356–3360 (2008).

[17] O. Chalus and J.-C. Diels, "Lifetime of fluorocarbon for high-energy stimulated Brillouin scattering," J. Opt. Soc. Am. B **24**, 606–608 (2007).

[18] T. R. Barends, L. Foucar, S. Botha, R. B. Doak, R. L. Shoeman, K. Nass, J. E. Koglin, G. J. Williams, S. Boutet, M. Messerschmidt *et al.*, "De novo protein crystal structure determination from x-ray free-electron laser data," Nature **505**, 244–247 (2014).

[19] D. C. Hanna, B. Luther-Davies, and R. C. Smith, "Single longitudinal mode selection of high power actively Q-switched lasers," Opto-electronics **4**, 249–256 (1972).

[20] Y. K. Park and R. Byer, "Electronic linewidth narrowing method for single axial mode operation of Q-switched Nd: YAG lasers," Optics Communications **37**, 411 – 416 (1981).

[21] D. J. Kuizenga, "Short-pulse oscillator development for the Nd:glass laser-fusion systems," Quantum Electronics, IEEE Journal of **17**, 1694–1708 (1981).

[22] J.-L. Lachambre, P. Lavigne, G. Otis, and M. Noel, "Injection locking and mode selection in TEA-CO2 laser oscillators," Quantum Electronics, IEEE Journal of **12**, 756 – 764 (1976).

[23] Y. K. Park, G. Giuliani, and R. L. Byer, "Stable single-axial-mode operation of an unstable-resonator Nd:YAG oscillator by injection locking," Opt. Lett. **5**, 96–98 (1980).

[24] L. A. Rahn, "Feedback stabilization of an injection-seeded Nd:YAG laser," Appl. Opt. **24**, 940–942 (1985).

[25] S. W. Henderson, E. H. Yuen, and E. S. Fry, "Fast resonance-detection technique for single-frequency operation of injection-seeded Nd:YAG lasers," Opt. Lett. **11**, 715–717 (1986).

[26] P. Esherick and A. Owyoung, "Polarization feedback stabilization of an injection-seeded Nd:YAG laser for spectroscopic applications," J. Opt. Soc. Am. B **4**, 41–47 (1987).

[27] A. Sträßer, T. Waltinger, and M. Ostermeyer, "Injection seeded frequency stabilized Nd:YAG ring oscillator following a pound-drever-hall scheme," Appl. Opt. **46**, 8358–8363 (2007).

[28] C. Marengoni, F. Canova, D. Batani, R. Benocci, M. Librizzi, V. Narayanan, M. Gomareschi, G. Lucchini, A. Kilpio, E. Shashkov, I. Stuchebrukhov, V. Vovchenko, V. Chernomyrdin, I. Krasuyk, T. Hall, and S. Bittanti, "Mode-locking optimization with a real-time feedback system in a nd:yttrium lithium fluoride laser cavity," Review of Scientific Instruments **78**, 013105 (2007).

[29] R. L. Schmitt and L. A. Rahn, "Diode-laser-pumped Nd:YAG laser injection seeding system," Appl. Opt. **25**, 629–633 (1986).

[30] S. DeSilvestri, P. Laporta, V. Magni, and O. Svelto, "Solid-state laser unstable resonators with tapered reflectivity mirrors: the super-Gaussian approach," IEEE J. Quantum Electron. **QE-24**, 1172–1177 (1988).

[31] V. Evtuhov and A. E. Siegman, "A "twisted-mode" technique for obtaining axially uniform energy density in a laser cavity," Appl. Opt. **4**, 142–143 (1965).

[32] Y. K. Park, G. Giuliani, and R. Byer, "Single axial mode operation of a Q-switched Nd:YAG oscillator by injection seeding," Quantum Electronics, IEEE Journal of **20**, 117 – 125 (1984).

[33] A. E. Siegman, *Lasers* (Univerisy Science Books, 1986), chap. 29.5, pp. 1154–1162.

[34] D. T. Hon, "Pulse compression by stimulated Brillouin scattering," Opt. Lett. **5**, 516–518 (1980).

[35] V. Kmetik, H. Fiedorowicz, A. A. Andreev, K. J. Witte, H. Daido, H. Fujita, M. Nakatsuka, and T. Yamanaka, "Reliable stimulated Brillouin scattering compression of Nd:YAG laser pulses with liquid fluorocarbon for long-time operation at 10 Hz," Appl. Opt. **37**, 7085–7090 (1998).

[36] H. Yoshida, V. Kmetik, H. Fujita, M. Nakatsuka, T. Yamanaka, and K. Yoshida, "Heavy fluorocarbon liquids for a phase-conjugated stimulated Brillouin scattering mirror," Appl. Opt. **36**, 3739–3744 (1997).

[37] H. Yoshida, H. Fujita, M. Nakatsuka, T. Ueda, and A. Fujinoki, "Temporal compression by stimulated Brillouin scattering of Q-switched pulse with fused-quartz and fused-silica glass from 1064 nm to 266 nm wavelength," Laser and Particle Beams **25**, 481–488 (2007).

[38] H. Yoshida, T. Hatae, H. Fujita, M. Nakatsuka, and S. Kitamura, "A high-energy 160-ps pulse generation by stimulated Brillouin scattering from heavy fluorocarbon liquid at 1064 nm wavelength," Opt. Express **17**, 13654–13662 (2009).

[39] W. Hasi, Z. Zhong, Z. Qiao, X. Guo, X. Li, D. Lin, W. He, R. Fan, and Z. L, "The effects of medium phonon lifetime on pulse compression ratio in the process of stimulated Brillouin scattering," Optics Communications **285**, 3541 – 3544 (2012). Special Issue: Sub-wavelength Light Localization and Focusing.

[40] S. Schiemann, W. Ubachs, and W. Hogervorst, "Efficient temporal compression of coherent nanosecond pulses in a compact SBS generator-amplifier setup," Quantum Electronics, IEEE Journal of **33**, 358 –366 (1997).

[41] D. Neshev, I. Velchev, W. Majewski, W. Hogervorst, and W. Ubachs, "SBS pulse compression to 200ps in a compact single-cell setup," Applied Physics B **68**, 671–675 (1999).

[42] S. Schiemann, W. Hogervorst, and W. Ubachs, "Fourier-transform-limited laser pulses tunable in wavelength and in duration (400-2000 ps)," Quantum Electronics, IEEE Journal of **34**, 407–412 (1998).

[43] I. Velchev, D. Neshev, W. Hogervorst, and W. Ubachs, "Pulse compression to the subphonon lifetime region by half-cycle gain in transient stimulated Brillouin scattering," Quantum Electronics, IEEE Journal of **35**, 1812–1816 (1999).

[44] C. Dane, W. Neuman, and L. Hackel, "High-energy SBS pulse compression," Quantum Electronics, IEEE Journal of **30**, 1907 –1915 (1994).

[45] M. J. Damzen and M. H. R. Hutchinson, "High-efficiency laser-pulse compression by stimulated Brillouin scattering," Opt. Lett. **8**, 313–315 (1983).

[46] M. Damzen and H. Hutchinson, "Laser pulse compression by stimulated Brillouin scattering in tapered waveguides," Quantum Electronics, IEEE Journal of **19**, 7–14 (1983).

[47] R. R. Buzyalis, A. S. Dementjev, and E. K. Kosenko, "Formation of subnanosecond pulses by stimulated Brillouin scattering of radiation from a pulse-periodic Nd:YAG laser," Soviet Journal of Quantum Electronics **15**, 1335 (1985).

[48] I. T. Veltchev, "Stimulated Brillouin scattering pulse compression and harmonic generation: applications to precision XUV laser spectroscopy," Ph.D. thesis, Laser Centre of the Vrije Universiteit Amsterdam (2001).

[49] R. W. Boyd, *Nonlinear optics*, T (Academic Press, 2003), 2nd ed.

[50] W. Kaiser and M. Maier, "Stimulated Rayleigh, Brillouin, and Raman spectroscopy," in "Laser Handbook," , vol. 2, F. T. Arecchi and E. O. Schulz-Dubois, eds. (North Holland, 1972), pp. 1077–1150.

[51] X. Xu and J.-C. Diels, "Stable single axial mode operation of injection-seeded Q-switched Nd:YAG laser by real-time resonance tracking method," Applied Physics B **114**, 579–584 (2014).

[52] J. Alda and G. D. Boreman, "On-axis and off-axis propagation of Gaussian beams in gradient index media," Appl. Opt. **29**, 2944–2950 (1990).

[53] G. Abbate, U. Bernini, E. Ragozzino, and F. Somma, "The temperature dependence of the refractive index of water," Journal of Physics D: Applied Physics **11**, 1167 (1978).

[54] S. De Silvestri, P. Laporta, V. Magni, and O. Svelto, "Solid-state laser unstable resonators with tapered reflectivity mirrors: the super-gaussian approach," Quantum Electronics, IEEE Journal of **24**, 1172–1177 (1988).

[55] O. J. Chalus, "Study of nonlinear effects of intense uv beams in the atmosphere," Ph.D. thesis, 'a l? Ecole Nationale Sup?erieure de Physique de Strasbourg (2007).

[56] M. Klein and T. Furtak, *Optics* (Wiley, New York, 1986), 2nd ed.

[57] T. A. Niday, E. M. Wright, M. Kolesik, and J. V. Moloney, "Stability and transient effects in nanosecond ultraviolet light filaments in air," Physical Review E **72**, 016618 (2005).

[58] F. Arqueros, F. Blanco, and J. Rosado, "Analysis of the fluorescence emission from atmospheric nitrogen by electron excitation, and its application to fluorescence telescopes," New Journal of Physics **11**, 065011 (2009).

[59] M. Scheller, M. S. Mills, M.-A. Miri, W. Cheng, J. V. Moloney, M. Kolesik, P. Polynkin, and D. N. Christodoulides, "Externally refuelled optical filaments," Nature Photonics **8**, 297–301 (2014).

[60] D. Mirell, O. Chalus, K. Peterson, and J.-C. Diels, "Remote sensing of explosives using infrared and ultraviolet filaments," JOSA B **25**, B108–B111 (2008).